

Dynamic Light Scattering Studies of Phase Transitions in Polymers and Gels


by
Michal J. P. Orkisz

B.S., Computer Science, Massachusetts Institute of Technology (1988)
B.S., Physics, Massachusetts Institute of Technology (1988)


Submitted to the Department of Physics
in partial fulfillment of the requirements for the degree of
Doctor of Philosophy
at the
MASSACHUSETTS INSTITUTE OF TECHNOLOGY
MAY 1994

© 1994 Massachusetts Institute of Technology

All rights reserved


Signature of Author _____
Department of Physics
May, 1994


Certified By _____ 4/28/94
Toyoichi Tanaka
Thesis Supervisor


Accepted By _____
George F. Koster
Chairman, Departmental Committee

MASSACHUSETTS INSTITUTE
OF TECHNOLOGY

MAY 25 1994

PHYSICS
Department of
Science

DYNAMIC LIGHT SCATTERING STUDIES OF PHASE TRANSITIONS IN POLYMERS AND GELS

by

Michal J. P. Orkisz

Submitted to the Department of Physics on Apr. 29, 1994

in partial fulfillment of the requirements for the degree of

Doctor of Philosophy in Physics

ABSTRACT

Implementation of a complete system for automated light scattering studies of gels is described and applied to several gel systems: a neutral homopolymer gel, a polyelectrolyte, and a polyampholyte exhibiting multiple phase behavior. A logarithmic software correlator capable of measuring delays from $0.8\mu\text{s}$ to several hours simultaneously was designed and used as the core for this system. A method for estimating correct ensemble averages from time average data collected at different locations was compiled. A gel description based on collective diffusion and non-ergodic theories provides basis for interpreting scattering data in terms of dynamic and static components. The origin of structural inhomogeneities was investigated and found to be dependent on the pre-gel solution state within the phase diagram at the onset of gelation. A NIPA (N-isopropylacrylamide) monomer phase diagram was determined to elucidate the last notion, and found to exhibit a lower critical solution temperature. The critical point was found to be well below that of a gel. Measurement temperature dependence of light scattering in a NIPA gel was probed through a discontinuous volume phase transition. Near-critical fluctuations in both dynamic and static intensities were found close to the spinodal line. Correlation function shapes confirmed the collective diffusion origin of dynamic intensity fluctuations. The friction coefficient obtained by light scattering was found not to vanish near the critical point, contrary to macroscopic liquid flow measurements. A weakly charged NIPA gel was examined and the light scattering results were in agreement with existing SANS data for this gel, confirming the notion of a microphase separation. A novel dynamic behavior is reported – power law shape of the correlation function, with a temperature dependent exponent. A multiple phase polyampholyte gel (acrylic acid + MAPTAC) was also studied. The pre-gel solution pH was shown to affect gel scattering behavior. The static intensity was found to have two different concentration dependencies for different pH regions. This demonstrated the existence of another gel order parameter. Qualitative explanation, based on light scattering results, was given for some aspects of this gel's complex phase behavior.

Thesis Supervisor: Dr. Toyochi Tanaka

Title: Professor of Physics

"AD MAIOREM DEI GLORIAM"
I WOULD ALSO LIKE TO DEDICATE THIS THESIS
TO MY PARENTS:
JANUSZ AND MARIA ORKISZ
AND TO MY "ADOPTED MOTHER"
ANA LYDIA SAWAYA

ACKNOWLEDGMENTS

First I would like to thank my supervisor, Dr. Tanaka. There are many reasons for my gratitude: his supervision, his encouragement, his patience, and last, but not least, his faith in me that in many cases exceeded my faith in myself.

I am grateful to my many colleagues and co-workers I encountered in Prof. Tanaka's group during my several years' sojourn here. I list them in an alphabetical order: Dr. Masahiko Annaka, Anthony English, Dr. Sid Gorti, Prof. Alexander Grosberg, Dr. Terrance Hwa, Dr. Frank Ilmain, Prof. Etsuo Kokofuta, Dr. Yong Li, Dr. Toyoaki Matsuura, Vijay Pande, Bill Robertson, Prof. Mitsuhiro Shibayama, Prof. Ron Siegel, Dr. Masayuki Tokita, Kevin Wasserman, Prof. Shigeo Yoshino, Dr. Xiaohong Yu, and Dr. Yong-Quing Zhang.

I want to thank my parents and the rest of my family. They know best what I need to be grateful for, and anyone else can use his or her imagination.

Last but not least, I want to extend my thanks to all of my C&L friends at MIT, in Boston, in the USA, and all over the world. Foremost among them to my "adopted mother", Dr. Ana Lydia Sawaya, without whose encouragement to take my life seriously I would probably have not finished this thesis.

TABLE OF CONTENTS

INTRODUCTION	15
0.1 Gels	15
0.2 Gel Phase Transitions.....	16
0.2.1 Fundamental Forces	18
0.2.1.1 van der Waals Interaction	18
0.2.1.2 Hydrophobic Interaction	18
0.2.1.3 Hydrogen Bonding.....	18
0.2.1.4 Electrostatic Interactions.....	19
0.2.2 Flory-Huggins Theory of Gel Phase Transitions	19
0.3 Light Scattering.....	21
0.3.1 Overview	21
0.3.2 Scattering Geometry	21
0.3.3 The Correlation Function	22
0.4 The Apparatus	23
0.4.1 Overview	23
0.4.2 Sample Holders	25
0.4.3 Sample Translation	26
0.5 About this Thesis	27
0.5.1 Motivation	27
0.5.2 Organization	28
0.5.3 Specific Contributions.....	29
References	31
1. DESIGN AND IMPLEMENTATION OF A SOFTWARE CORRELATOR	33
1.1 Introduction	33
1.2 Correlation Function	34

1.2.1	Definition	34
1.2.2	Discrete Approximation	35
1.2.3	Graphical Representation	37
1.2.4	Sources of Errors	37
1.2.4.1	Decimation	38
1.2.4.2	Discretization	39
1.2.4.3	Finite Collection Time	41
1.3	Software design	41
1.3.1	Why Logarithmic?	41
1.3.2	Principle of Operation	42
1.3.3	Main Loop	44
1.3.4	Initialization	45
1.4	Data compression	46
1.5	Hardware design	46
1.5.2	BI-2030AT as a Front End	48
1.6	Analysis Software	49
1.6.1	Ensemble Averaging	49
1.6.2	Curve Plotting and Fitting	50
	Summary	51
	References	51
2.	LIGHT SCATTERING FROM NON-ERGODIC SYSTEMS	53
2.1	Overview of (Non)ergodicity	53
2.1.1	Ensemble vs. Time Average	54
2.1.2	Ergodic vs. Nonergodic Systems	56
2.1.3	Light Scattering	56
2.2	Determining the Ensemble Average	58

2.2.1	Different Approaches	59
2.2.2	Correcting the Effects of Finite Averaging	60
2.2.2.1	Underlying Assumptions.....	61
2.2.2.2	Estimating the Deviation.....	62
2.2.2.3	Correcting the Deviation	63
2.3	Theory of Light Scattering in Gels	67
2.3.1	Origin of the Static Component	67
2.3.2	Collective Diffusion and the Origin of the Dynamic Component	69
2.3.3	Summary	71
2.4	Some Experimental Results	71
2.4.1	Correlation Function Statistics	71
2.4.2	Speckle Pattern.....	73
2.4.3	Reproducibility.....	74
2.4.4	Randomness	75
2.4.5	Intensity Histogram.....	76
2.4.6	Local Oscillator Effects (Heterodyning).....	77
2.4.7	Extracting Decay Time from Ensemble Average	78
	Conclusion	80
	References	81

3. FROZEN GEL INHOMOGENEITIES – TEMPERATURE OF GELATION

	DEPENDENCE	83
3.1	Introduction	84
3.2	Experiments	85
3.2.1	Sample Preparation	85
3.2.2	Light Scattering.....	86

3.3	Results	86
3.3.1	General Observations	86
3.3.2	Dependence on Gelation Temperature	89
3.3.3	Dependence on Measurement Temperature	89
3.4	Discussion	94
	Conclusions	97
	Further Research	98
	References	99
4.	PHASE DIAGRAM OF NIPA MONOMER	101
4.1	Introduction	101
4.2	Experiments	102
4.2.1	Liquid-Liquid Phase Boundary	104
4.2.2	Solid-Liquid Phase Boundary	104
4.3	Results	104
4.4	Discussion	106
	Conclusion	110
	Further Research	110
	References	111
5.	LIGHT SCATTERING FROM A NIPA GEL NEAR A TEMPERATURE INDUCED PHASE TRANSITION.....	113
5.1	Introduction	113
5.2	Experiments	115
5.2.1	Sample Preparation	115
5.2.2	Temperature	115
5.2.3	Approach to the Transition	115
5.2.4	Light Scattering	116

5.3	Results	117
5.3.1	The Transition	117
5.3.2	Correlation Functions	118
5.3.3	Light Scattering Results	120
5.4	Discussion	120
5.4.1	Shape of the Correlation Function	120
5.4.2	Near-Critical Behavior	124
5.4.3	Network-Solvent Friction	128
	Conclusions	131
	Further Research	131
	References	132
6.	LIGHT SCATTERING FROM A POLYELECTROLYTE GEL.....	133
6.1	Introduction	133
6.2	Experiments	137
6.2.1	Sample Preparation	137
6.2.2	Temperature	137
6.2.3	Light Scattering	137
6.3	Results	139
6.3.1	Scattering Parameters.....	139
6.3.2	Intensities	142
6.4	Discussion	142
	Conclusion	146
	Further Research	147
	References	148
7.	ANALYSIS OF A MULTIPLE-PHASE POLYAMPHOLYTE GEL.....	149
7.1	Introduction	149

7.1.1	Organization of this Chapter	152
7.1.2	Sample Preparation	152
7.1.3	Temperature	154
7.1.4	Light Scattering.....	154
7.2	"Unwashed" gels – Dependence on Preparation Conditions and Composition	155
7.2.1	Experiments	155
7.2.2	Results	155
7.2.3	Discussion	158
7.3	"Constrained" gels - Diameter Dependence.....	159
7.3.1	Experiments	159
7.3.2	Results	160
7.3.3	Discussion	163
7.4	Comparison of Unwashed, Constrained, and Free gels	165
7.4.1	Experiments	165
7.4.2	Results	167
7.4.3	Discussion	168
7.5	"Free" Gels – pH Dependence	169
7.5.1	Experiments	169
7.5.2	Results	169
7.5.3	Discussion	171
	Conclusions	178
	Further Research	179
	References	181
	FURTHER RESEARCH	183
	CONCLUSION.....	187

INTRODUCTION

This thesis deals with light scattering studies of phase transitions in polymer gels. I shall start by briefly describing these terms in reverse order: first gels, then gel phase transitions, then the light scattering technique. Subsequently, the apparatus used in most of the experiments reported here will be described. Finally, some information about the organization, and an evaluation of this thesis will be given.

0.1 GELS

A polymer gel is a three-dimensional polymer network in contact with a solvent. The polymers can be of any nature: biopolymers such as proteins or DNA or synthetic polymers. The gels investigated in this thesis are exclusively synthetic. Component chains can be linked by physical means (such as entanglements, hydrogen bonding), or covalent crosslinks (i.e., chemical bonds). This thesis deals only with chemically crosslinked gels. An interesting aspect of such gels is that the whole gel is a single molecule of macroscopic size. They are an ideal medium for studying molecular interactions, as the effects of microscopic inter-polymer forces manifest themselves on a macroscopic level.

Gels are abundant in nature. Many of the living tissues, such as the cornea, vitreous humor, the connective tissues, basement membranes, liners of stomach and lung surfaces, etc., exist in a gel form. Gels are widely used in scientific, industrial, and everyday life contexts. Their applications range from a medium for macromolecule separation by electrophoresis or liquid chromatography in biology, "breathable" materials

for soft contact lenses, super absorbent fillers of disposable diapers, slow release carriers of drugs in medicine, and many others. New research in "intelligent gels" promises future applications in molecular recognition (artificial enzymes), mechanical actuators (artificial muscles), controlled drug release (drug release in response to chemical changes in the organism), information storage (holographic memories), etc.

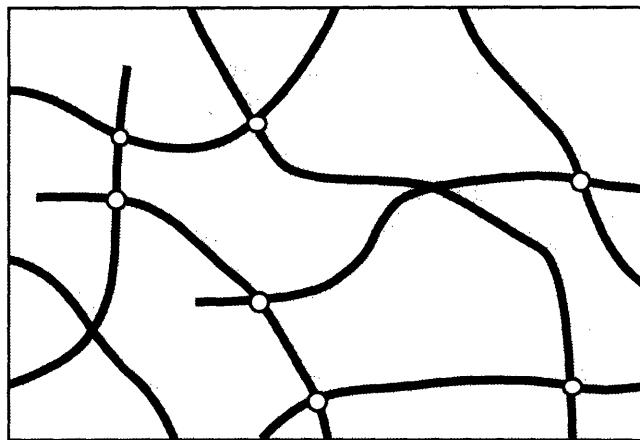


Fig. 1 Schematic drawing of a gel. Black lines represent the polymer chains, white circles the crosslinks, and gray background the solvent.

To realize these potential applications and other future developments it is important to understand the microscopic structure of gels. One of the goals of this thesis is to make a contribution towards this understanding.

0.2 GEL PHASE TRANSITIONS

The phase transitions discussed in this thesis are volume phase transitions. Figure 2 illustrates such a transition. The topology of the network remains the same (the number and the placement of crosslinks does not change), but the conformation and density of the chains changes. Solvent is expelled from the network in the process. This is a phase transition in the usual sense of the word (see, e.g., (1)). An infinitesimal change in

external conditions can trigger a macroscopic change in the gel. Volume changes of up to 1000 times have been observed. The change is fully reversible, i.e., when the initial conditions are restored the gel returns to its former state.

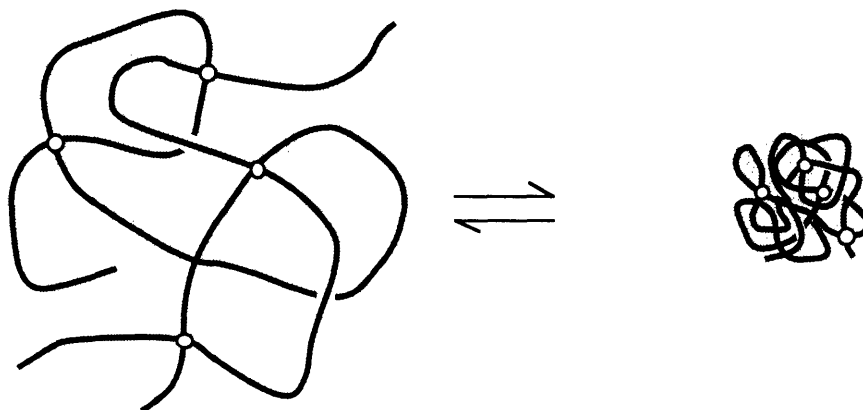


Fig. 2 Volume phase transition of a gel. The network collapses – the chains become more densely packed, and the solvent is expelled.

Volume phase transitions can be contrasted with another class of transitions closely related to the gel state: sol-gel transitions. In the latter case, a solution (of finite viscosity) becomes, through the process of crosslinking, a gel (of infinite viscosity). These transitions, although interesting in their own right, are not dealt with in this thesis.

The possibility of a gel volume phase transition was first predicted theoretically by Dusek and Patterson in 1968 (2). A physical manifestation of such a transition was not observed till almost 10 years later. In 1977 Tanaka for the first time observed a volume transition of a slightly ionized acrylamide gel in an acetone-water mixture (3). Since then many factors that induce phase transitions have been discovered: temperature (4), solvent composition (5,6), solvent pH (7), electric field (8), external pressure (9), ultraviolet (10) and visible light (11), and specific molecules (12).

The interested reader is referred to (13-14) and references therein for a much more exhaustive discussion of polymer gels and gel phase transitions.

0.2.1 Fundamental Forces

Gel phase transitions result from a competition between attractive and repulsive forces attempting to collapse and swell the gel. Listed below are the four fundamental forces responsible for molecular interactions (N.B. all are a manifestation of the electromagnetic force), which in gels compete with entropic forces manifested in gel-solvent mixing entropy and rubber elasticity.

0.2.1.1 van der Waals Interaction

The van der Waals interaction is present in every system. It is a multipole – induced multipole attraction (accompanied by short range excluded volume repulsion). Therefore its strength in water is usually much smaller than other interactions, and it can be ignored. However, a change in solvent composition can make it more pronounced. The first volume transition ever observed (3) was in fact induced by van der Waals attraction.

0.2.1.2 Hydrophobic Interaction

Hydrophobic interaction between polymer chains and water is an entropic force. Water molecules in the vicinity of a hydrocarbon group become more ordered (ice structure) than in pure water. Thus the entropy is lowered. In order to maximize the entropy the chains are forced to aggregate. The lowered chain entropy is compensated by the gain of entropy by water. This effect is stronger at higher temperatures, so hydrophobic gels tend to collapse when heated. The transition described in (4) is driven by a hydrophobic interaction.

0.2.1.3 Hydrogen Bonding

Hydrogen bonding is an attractive interaction due to formation of hydrogen bonds between polymer chains. The energy of a hydrogen bond is significantly smaller than that of a covalent bond, so the bonds can form and break as the temperature is decreased and increased. Reference (16) reports a phase transition driven by hydrogen bonding.

0.2.1.4 Electrostatic Interactions

Several effects are due to electrostatic forces between charged polymer chains themselves and between the chains and mobile counterions in the solution. If the network carries a net charge the osmotic pressure of counterions attempts to swell the gel. The is Coulomb repulsion between like network charges is usually screened by water. In the case of a polyampholyte gel, where both positive and negative charges are attached to the network, long range attractive forces are present (see Reference (17) for a more extensive treatment).

0.2.2 Flory-Huggins Theory of Gel Phase Transitions

The classical theory of gel phase transitions is based on the Flory-Huggins form of free energy (2). In this summary it is assumed that the swelling force is due to the counterion pressure (13). The free energy can be decomposed into three parts:

$$F = F_{\text{mixing}} + F_{\text{rubber elasticity}} + F_{\text{counterion}}$$

These terms can be expressed explicitly as:

$$\frac{F}{\nu kT} = N \frac{1-\phi}{\phi} [\ln(1-\phi) + \chi\phi] + \frac{1}{2} \left[3 \left(\frac{\phi_0}{\phi} \right)^{2/3} + \ln \phi \right] + f \ln \phi$$

(each term corresponding to the one above) where N is the total number of persistent units, ν the total number of chains (bounded by crosslinks), χ is the reduced chain-solvent interaction energy (Flory parameter), ϕ is the network volume fraction (ϕ_0 – the reference state – is the volume fraction when the chains are Gaussian – usually the concentration at which the gel was polymerized), and f is the charge per chain. When a gel is freely swollen, its osmotic pressure π is zero. Thus the swelling behavior can be analyzed by considering the isobars: $\pi = \phi^2 (\partial F / \partial \phi) = 0$.

Performing the calculations and expanding the logarithms to order ϕ^3 , the following simplified equation is obtained:

$$t = S \cdot (\rho^{-5/3} - \rho^{-1} / 2) - \rho / 3$$

with the reduced parameters defined as

$$t \equiv \frac{(1-2\chi) \cdot (2f+1)^{3/2}}{2\phi_0}$$

$$\rho \equiv \left(\frac{\phi}{\phi_0} \right) \cdot (2f+1)^{3/2}$$

$$S \equiv \left(\frac{v\nu}{N\phi_0^3} \right) \cdot (2f+1)^4$$

Analyzing this equation we observe that for S larger than $S_c=234.1$ the isobar has a Maxwell loop, and the transition becomes discontinuous. Figure 3 (reprinted from (13)) shows the swelling curves (parametrized by f) obtained from this equation.

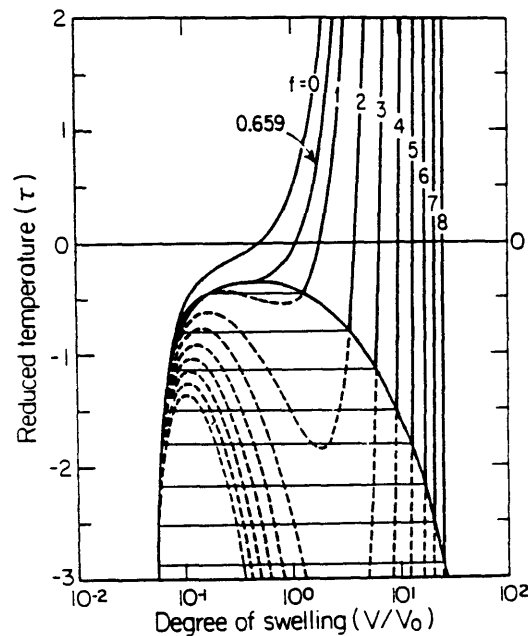


Fig. 3 Theoretical swelling curves for various degrees of ionization f (number of ions per chain), based on the Flory-Huggins formula. (Reprinted from (13)).

This model does not give correct quantitative results, but at least it can qualitatively predict existence of discontinuous volume phase transitions. The reader is referred to (13-15) for more details.

0.3 LIGHT SCATTERING

0.3.1 Overview

Many books have been devoted to the theory and practice of laser light scattering (see, e.g., (18-20)), so I will confine myself to essentials.

Light passing through a medium is scattered by density fluctuations (or, more precisely, by refractive index fluctuations). Scattered light is then detected and analyzed. This follows the general scheme of most techniques available to physicists today – be it condensed matter, atomic, or high energy. The sample is hit or probed with something and the response is observed. In our case the sample is a gel, and the probe is light. Here the incident light does not perturb the sample – it only probes the ever-present thermal fluctuations of the system.

It is interesting to note an exact analogy between a light scattering experiment and the principle of FM radio. The carrier wave of the radio corresponds to the monochromatic incident laser light. This carrier is frequency modulated by another process of much lower frequency – either by an audio signal, or by the thermal fluctuations inside a sample. The modulated wave is transmitted through space to a detector – ideally a so-called perfect square-law detector. This is implemented in a radio receiver using an antenna and electronics. In the case of light scattering this role is played by the surface of the photomultiplier tube (PMT), which is sensitive to intensity of the incident light – exactly the square of the incident electric field. The signal is then demodulated. In a radio receiver the voice or music is recovered, while in the case of light scattering it is the fluctuating signal of the sample. Actually, we are not interested in the signal itself, but rather in its signature obtained with the aid of an autocorrelator.

0.3.2 Scattering Geometry

Figure 4 illustrates the scattering geometry. Laser light passing through the sample is scattered (in all directions). Light scattered at an angle Θ with respect to the beam direction is picked up by the detector.

Incident laser light of wavelength λ (in vacuum) is described by wave vector \mathbf{k}_i , where $|\mathbf{k}| = 2\pi n/\lambda$, where n is the refractive index of the medium. The scattered light's wave vector has the same magnitude $|\mathbf{k}|$, but different direction \mathbf{k}_f . Their difference gives the scattering vector $\mathbf{q} = \mathbf{k}_f - \mathbf{k}_i$, whose magnitude is, from the law of cosines,

$$q = \frac{4\pi n}{\lambda} \sin \frac{\Theta}{2}$$

Throughout this thesis we use a fixed 90° angle and a He-Ne laser, with a vacuum wavelength $\lambda=633\text{nm}$. The resulting scattering vector magnitude is $q\approx 70 \text{ nm}^{-1}$.

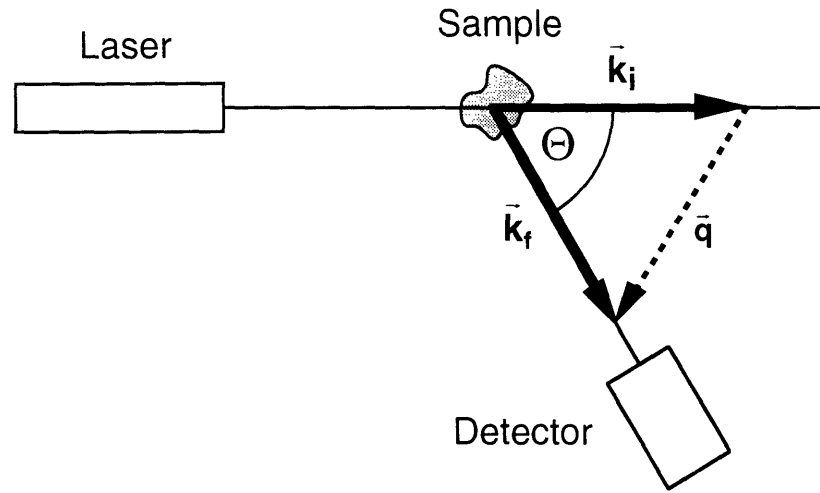


Fig. 4 Scattering geometry. Incident laser light is scattered by the sample and detected at an angle Θ . The construction of the scattering vector \vec{q} is also shown.

0.3.3 The Correlation Function

The way of extracting information from the scattered light is by measuring the autocorrelation function of the scattered light intensity. The time-averaged normalized intensity autocorrelation function $C(t)$ is defined as:

$$C(t) = \frac{\langle I(t') I(t'+t) \rangle}{\langle I(t') \rangle^2}$$

where $I(t)$ is the instantaneous intensity measured at time t . If $I(t)$ and $I(t+\Delta t)$ can be considered independent for $\Delta t \neq 0$, as in the case of Poisson statistics (normal light source), or for Δt much greater than the internal relaxation time (for any fluctuating system), then the average of the product $I(t) \cdot I(t+\Delta t)$ equals the product of the averages, so $C(t)=1$. Thus one would expect the limit of $C(t)$ for large t to be 1. On the other hand, at $t=0$ we have

$C(0)=\langle I^2 \rangle / \langle I \rangle^2$, so $C(0)$ is related to the second moment of intensity distribution. For an electric field with Gaussian distribution (as one would normally expect), we have $C(0)=2$. The information conveyed by the correlation function is the same as in the power spectrum of the signal. In fact they are related to each other by a Fourier transform.

0.4 THE APPARATUS

This section describes the light scattering setup used for all of the light scattering experiments presented in this thesis. An overview is given first, and specific details are given later. In particular, the sample holders, the temperature control, and the sample translation are discussed. The core of the setup – the software correlator – is not described here since Chapter 1 is devoted to it.

0.4.1 Overview

The setup used throughout this thesis differs from a conventional light scattering apparatus (in design, not in principle). It is a Microscopic Laser Light Scattering (MLLS) setup (see Figure 5) where a microscope is used to observe the sample and to detect the scattered light. This particular setup was originally devised for performing light scattering experiments in microscopic biological samples. This setup was modified and adapted for scattering from gels since it offered several advantages over a conventional (optical table size) setup. First, it allows for precision measurements to be performed on small size samples. This is very important since the speed of a gel transition decreases quadratically with increasing size. Thus the speed gain from using samples of order 0.5mm (MLLS) as opposed to 5mm (conventional setup) is 100-fold. This translates to minutes versus days. The apparatus was also particularly amenable to installing a stepping motor for moving the sample under observation. This is important in gel light scattering measurements since gels are non-ergodic and one cannot equate the ensemble average with a time average of a measured signal. The ensemble average can be obtained by collecting data at different points.

There are two main disadvantages of our MLLS setup. The scattering angle is fixed. (A 90° angle was used since it was the most natural choice given the sample geometry – see Figure 6.) This precluded the possibility of running angular dependence

experiments, which could have shed more light on the structure of the systems under investigation. The other deficiency is that ideally the detector should be point-size. In practice, however, the finite size of the aperture of the objective lens extended the effective detector size, so that the scattering parameter β (more about its meaning in chapter 2) was 0.8 as opposed to the ideal value of 1.0 (actually, our conventional setup had an even lower value of β).

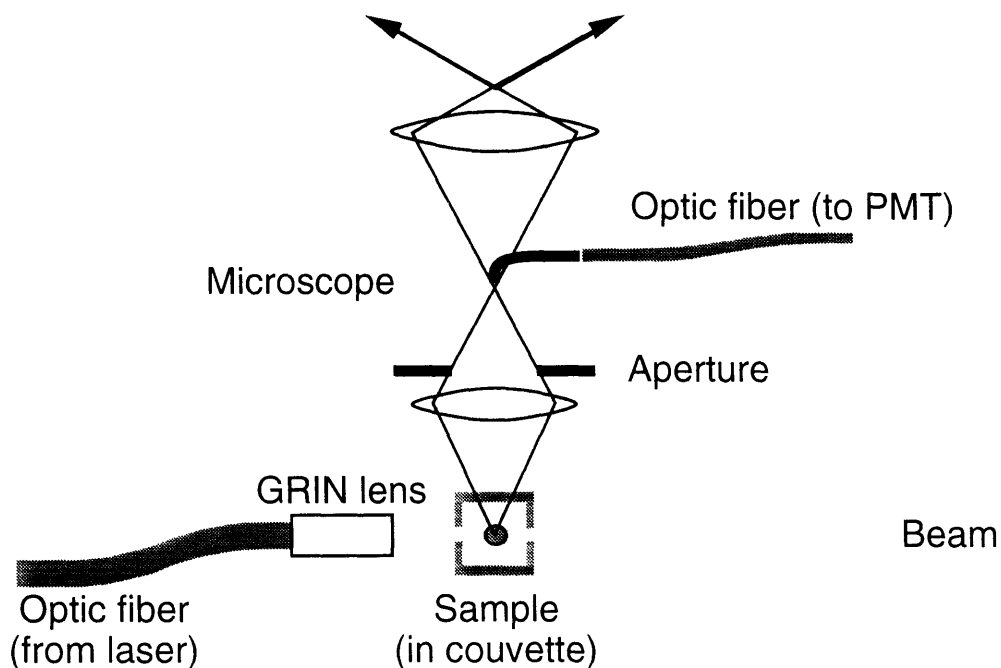


Fig. 5 Schematic diagram of the Microscopic Laser Light Scattering (MLLS) setup. The light from a laser is brought through a single mode optic fiber and focused with a GRIN lens. The scattered light is collected through microscope's optics and transmitted, through another optic fiber into the detector (a PMT)

Figure 5 illustrates the light scattering setup. The source of light was a Spectra Physics He-Ne laser (model 127) with an output power of $\sim 50\text{mW}$. The optics for delivering laser light to the sample were custom made by OZ Optics Ltd. The light was fed into a single-mode fiber using an OZ Optics coupler, and on exit focused by a GRIN (Graded Refraction INdex) lens 4mm away from the lens surface. This in practice gave a

focused waist of under $10\mu\text{m}$ in diameter. Some light was lost during the transmission, so the output power from the GRIN lens was reduced to about 20mW.

Figure 6 shows the scattering geometry. Scattered light (going up in the figure) is picked up through a Nikon OPTIPHOT microscope. It was equipped with a Leitz L32 long working distance objective lens (with adjustable aperture) and Gamma Scientific 10x eyepieces with built-in optical fiber in the focal plane (model 700-10-36A with $50\mu\text{m}$ fiber and 700-10-37A with $150\mu\text{m}$ fiber). The larger fiber was normally used. If the scattering intensity was too high, the $50\mu\text{m}$ fiber was employed. The light from the eyepieces traveled through a shielded fiber bundle to a photomultiplier tube operated in a photon counting mode. The pulses from the PMT were converted to TTL levels and fed into a correlator, which is described in detail in Chapter 1.

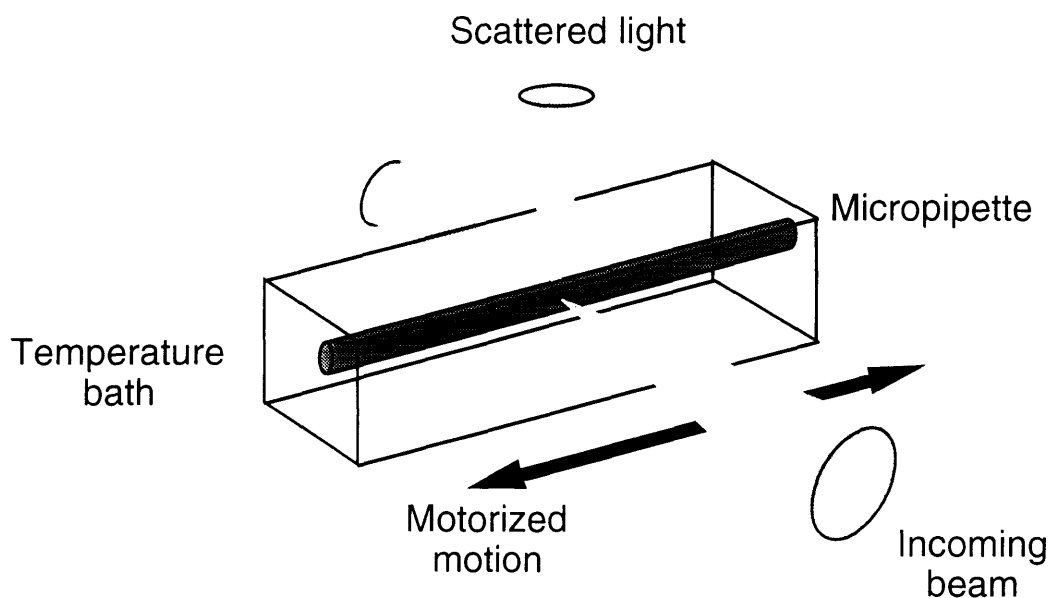


Fig. 6 Actual scattering and sample geometry

0.4.2 Sample Holders

Several sample holders were used depending on the conditions of the experiment. The simplest measurements were performed at room temperature measurements with no change in the gel environment. In this case the gel was kept in a round micropipette inserted into a square cuvette (10mm x 10mm) of optical quality glass (available from many glass manufacturers, e.g., Helma). The micropipette was held in place by rubber

spacers. The cuvette was filled with water to minimize the lens effect of the micropipette and plugged with a square rubber stopper. This arrangement is represented in Figure 6.

In some cases the environment in which the gel was placed had to be changed during the experiment. In a series of measurements, for example, the solution pH was monitored and varied. In this case the gels were allowed to swell freely as the solution flowed around them. They were held in place at one end by the micropipette in which they were made. Full description is provided in Chapter 7 where this holder is used.

Finally in some experiments the temperature had to be changed. The simplest solution would be to run water from a heat/refrigeration bath (such as Neslab or Lauda) through a cuvette holding the micropipette, as described above. However, the flow from the heat bath introduces vibrations that were picked up through light scattering and affect the correlation function. Therefore this solution is impractical. So a metal (copper in one version, aluminum in another) sample holder with glass windows was constructed, inside which the micropipette was immersed in water, as before. The holder sits on top of two thermoelectric devices connected to one of the temperature control units available in the lab (and constructed by a previous generation of graduate students). The controller uses a thermistor in a Wheatstone bridge configuration. The imbalance between the two branches of the bridge is presented to the input of an integrator (with adjustable gain and time constant), whose output, after amplification, drives the thermoelectric devices. This configuration was altered in such a way that the reference part of the bridge was replaced with the output of a DAC (Digital to Analog Converter) from Keithley System 570 controlled by the computer. Another thermistor was read by Keithley's ADC, so the temperature could be both controlled and monitored by the computer.

0.4.3 Sample Translation

All sample holders are mounted on an X-Y translation stage. The micrometric screw controlling the X stage was attached to a stepping motor which moves the stage back and forth. Stepping motors rotate their shafts in exact increments when the voltage applied to their coils is cycled through 4 phases. The particular motor used had 200 steps per revolution, which, combined with 0.5mm per revolution pitch of the micrometer screw, provides a resolution of 2.5 μ m per step. A stepping motor controller was constructed. It translates the signals from a parallel port of an IBM PC compatible computer into 4 phases. They are amplified through power transistors to drive two independent stepper motors. (The other motor was sometimes used to re-center the beam

during long measurements.) Thus the position could be controlled from the same computer that collected the correlation function and controlled the temperature.

The only other complication was that each motor step would jerk the stage, and shake the sample. Since the sample had to be perfectly still for light scattering measurements, this had to be avoided (especially in cases when the sample was floating almost freely). The solution adopted was to oscillate the motor rapidly ($\sim 7\text{kHz}$) between two consecutive steps, and to vary smoothly the oscillation duty cycle. As the oscillations are much faster than motor's response time, this results in a smooth transition between the two positions.

0.5 ABOUT THIS THESIS

The following three sections describe this thesis. First the motivation behind this research is stated, then the conceptual organization is described. Finally a critical look is taken where author's contributions are stated and the relevance of the findings discussed.

0.5.1 Motivation

A property of gels which sets them apart from most other substances is that they combine both liquid and solid nature. A liquid, even as complex as a polymer solution, does not exhibit any permanent structure. The solvent particles are free to move around, even if it happens very slowly. A solid, on the other hand, can have a permanent structure. Positions of individual particles are fixed in space and time except for the thermal oscillations about the equilibrium positions. A gel, on the other hand, consists of polymer chains that are mostly free to move around (as in a liquid), but there are some limitations because the chain ends are linked to other chains. Beyond the conformational motion of the chain whose end points are fixed, the movement involves a collective displacement of the whole network. A network can have many imperfections – dangling ends, loops, regions of higher crosslinking density, etc., – all of which influence the structure of a gel. These are structural inhomogeneities. In addition, other inhomogeneities can be formed dynamically by the monomer interactions.

These inhomogeneities play an important role in the optical, mechanical, rheological, etc., properties of gels. They also influence the gel phase behavior. What is even more important, the inhomogeneities are related to the memory of structure.

Random polymers are free to change their conformation and relative positions. They do not exhibit any memory. Certain biopolymers, especially the proteins that play a crucial role in life processes, can "remember" their structure. They exist in one, or at most a few conformations. When pushed out of this state, they can find it again (thermodynamic renaturation). The structure of some proteins, such as enzymes and antibodies, enables them to lock onto specific targets (molecular recognition). Frozen inhomogeneities provide gels with at least a trivial form of shape memory – densely crosslinked regions remain dense, while dilute regions stay dilute. Can this memory be more specific? Can a gel, or at least its portion, find a particular "frozen" state? Would this state be unique? Can it be reached again after the gel was swollen? Would it be possible to design such a state? Can it be made to recognize specific targets? Such structure, if existent, would also be a form of a structural inhomogeneity.

To answer these questions it is important to understand the physical principles of their formation and to characterize the inhomogeneities. This thesis attempts to do this. It investigates a mechanism by which thermal fluctuations become frozen as inhomogeneities. It traces the divergence of these inhomogeneities at the spinodal line. Finally, it investigates the dynamic and static nature of inhomogeneities caused by interactions among monomers.

0.5.2 Organization

The thesis begins by describing the logarithmic correlator, used extensively in the experiments reported here, as a part of the light scattering setup described in this introduction. The second chapter presents the theory and practice of analyzing light scattering data. The following chapters describe the actual experiments. The progression is from relatively simple systems (neutral gels), through a more complicated polyelectrolyte gel (network charged with ions of one polarity), to a polyampholyte (network with both anionic and cationic components). More precisely, the third chapter deals with the formation of inhomogeneities during the gelation process (probed by light scattering) of an N-isopropylacrylamide (NIPA) gel. The fourth chapter determines the phase diagram of NIPA monomer, which is necessary to elucidate the results of the third chapter. The fifth chapter examines light scattering from a NIPA gel near a discontinuous phase transition. The sixth chapter examines the behavior of NIPA with ionizable units of acrylic acid added to make it a weak polyelectrolyte. Finally, the seventh chapter reports various aspects of scattering from a polyampholyte gel – copolymer of acrylic acid and MAPTAC.

0.5.3 Specific Contributions

All the experiments presented in this thesis were performed by the author (with the exception of several figures reprinted from elsewhere and marked as such). The core of the microscopic light scattering apparatus was neither designed nor built by the author. However, significant modifications and additions were done by the author to convert it from a system prepared to measure biological samples to one suitable for the study of gels. In particular, the optics were redesigned, the sample holders, temperature controllers and the motorized stage designed, constructed, and tested. This setup offers unique advantages in studying microscopic size gels.

The logarithmic software correlator described in Chapter 1 is the fruit of several hardware designs conceived by the author (but never implemented) in an attempt to create a simple and inexpensive correlator suitable for use in clinical eye testing equipment. The idea of a logarithmic correlator implemented partially in software is not new. In fact there exist some commercial designs. However this correlator was designed and implemented entirely by the author. Its main advantages are very low cost of necessary hardware, and its integration into a larger system for collecting and analyzing gel light scattering data (also designed and implemented entirely by the author).

The theoretical considerations presented in Chapter 2 are neither new, nor due to the author. However, the resulting procedures for extracting information from the scattering data and correcting for errors due to averaging over a finite set of data are derived by the author. So is the attempt to combine the collective diffusion with the non-ergodic approaches, which is later successfully (at least for simple systems) applied to the actual data.

The main ideas in Chapter 3 (about the origin of gel inhomogeneities) are not due to the author. All the experimental results are his, though. Among them of greatest value are the precise temperature of gelation measurements and their decomposition into static and dynamic components.

All of Chapter 4 is the author's work, including the data, its analysis, and the simple model explaining the results. This work furnishes important evidence supporting the ideas presented in Chapter 3.

Some of the light scattering experiments presented in Chapter 5 were performed in the past by other researchers. Therefore part of the experimental data repeats previous results. However, author's results are more precise and a more thorough analysis of the data (using the methods devised in Chapter 2) reveals some interesting new aspects. In

addition the author was able to perform light scattering from a collapsed NIPA gel, which is a new result. This, combined with the data from swollen gel, gives a clearer look at the discontinuous transition.

The experiments described in Chapter 6 originated in conjunction with Small Angle Neutron Scattering experiments performed by Dr. M. Shibayama on the same gel. The light scattering study was performed entirely by the author. The observations presented in that chapter are new. Especially interesting is the power law shape of the correlation function and its temperature dependence at higher temperatures. The observation of power law behavior in this context is new. Unfortunately, the author failed to find any quantitative arguments that would model this behavior, so only an attempt is made to explain it qualitatively.

The experiments described in Chapter 7 originated in collaboration with Dr. M. Annaka in the process of his study of the multiple-phase gels. However, the results in Chapter 7 do not deal explicitly with the multiple-phase behavior (because of the difficulty of performing light scattering at the low concentrations of the multiple phases). Instead they reveal some interesting aspects of dependence on preparation conditions and explicitly demonstrate the existence of another order parameter (besides density) in a charged gel, which is an important finding. (N.B. the experiments presented in this chapter, more than any other ones, testify to the usefulness of the microscopic light scattering setup in studying gels, since they would be practically impossible to obtain with macroscopic gels.)

REFERENCES

- [1] Huang, K.: *Statistical Mechanics*, Wiley & Sons, New York, p 34ff (1963).
- [2] Dusek, K. and Patterson, D.: *J. Polym. Sci. Part A-2*, **6**, 1209 (1968).
- [3] Tanaka, T.: *Phys. Rev. Lett.*, **40**, 820 (1978).
- [4] Hirokawa, Y. and Tanaka, T.: *J. Chem. Phys.*, **81**, 6379 (1984).
- [5] Tanaka, T., Fillmore, D., Sun, S.-T., Nishio, I., Swislow, G. and Shah, A.: *Phys. Rev. Lett.*, **45**, 1636 (1980).
- [6] Ilavsky, M.: *Macromolecules*, **15**, 782 (1982).
- [7] Tanaka, T.: *Sci. Am.*, **244**, 124 (1981).
- [8] Tanaka, T., Nishio, I., Sun, S.-T. and Ueno-Nishio, S.: *Science*, **218**, 467 (1982).
- [9] Suzuki, A.: *4th Gel Symp.*, Tokyo (1990).
- [10] Mamada, A., Tanaka, T., Kungwachakun, D. and Irie, M.: *Macromolecules*, **23**, 1517 (1990).
- [11] Suzuki, A. and Tanaka, T.: *Nature*, **346**, 345 (1990).
- [12] Kokofuta, E., Zhang, Y.-Q. and Tanaka, T.: *Nature*, **351**, 302 (1991).
- [13] Li, Y. and Tanaka, T.: *Annu. Rev. Mater. Sci.*, **22**, 243-277 (1992).
- [14] Tanaka, T., Annaka, M., Ilmain, F., Ishii, K., Kokofuta, E., Suzuki, A. and Tokita, M.: *NATO ASI Series, Vol. H64*, pp. 683-703 (1992).
- [15] Shibayama, M. and Tanaka, T.: *Adv. in Polymer Sci.*, **109**, 1-62 (1992).
- [16] Ilmain, F., Tanaka, T. and Kokofuta, E.: *Nature*, **349**, 400 (1991).
- [17] Yu, X.H., Ph.D. Thesis, M.I.T (1993)
- [18] Chu, B.: *Laser Light Scattering*, Academic Press, London (1991).
- [19] Berne, B.J. and Pecora, R.: *Dynamic Light Scattering*, Wiley & Sons, New York, (1976).
- [20] Tanaka, T., "Light Scattering from Polymer Gels" in *Dynamic Light Scattering*, ed. R. Pecora, Plenum Publishing Co., New York (1985)

CHAPTER 1

DESIGN AND IMPLEMENTATION OF A SOFTWARE CORRELATOR

This chapter provides details of design and implementation of a logarithmic correlator and its supporting software and hardware. This instrument was used throughout the rest of this thesis for collecting light scattering data.

1.1 INTRODUCTION

The dynamic light scattering technique is a powerful method of examining the structure of solutions and gels. It can provide information about phenomena taking place at very different time scales. For example, a typical gel might exhibit a decay time of 10-100 μ s. On the other hand, the speckle pattern in such a gel is much more permanent, in some cases not changing on the time scale of days and larger. Several observed phenomena exhibited a correlation function displaying a power-law decay, which does not have a characteristic time scale at all. The need to examine such a wide range of time scales at the same time dictated the necessity to go beyond the equally spaced 136 channels of a typical linear correlator. It is true that the Brookhaven Instruments' BI-2030AT available to me has a so-called multiple-tau option in which four banks of 32 channels can be set to separate widths, but that is achieved through a decimation of the number of arriving photons. This introduces an accuracy loss that has to be compensated

by very long acquisition times. Another recurring problem due to the decimation is that often there is a discontinuous jump in the correlation function between two data banks.

It turns out that a 50MHz i486 Intel microprocessor is fast enough to process 16 channels of the real-time data with the channel width of about 10 μ s and with 32 bits of accuracy (which provide for practically NO data loss due to decimation). This fact was used to construct a purely software logarithmic correlator according to the scheme described below.

1.2 CORRELATION FUNCTION

Correlation function condenses the information about the temporal evolution of a system. Its information content is equivalent to that of the signal's power spectrum. Therefore measuring the correlation function gives one access to the dynamics of the system on various time scales. The reader is referred to References (1,2), and to Chapter 2 of this thesis for a more thorough treatment of the subject.

1.2.1 Definition

The intensity-intensity autocorrelation function (an approximation to which is measured in a light scattering experiment) is defined as follows:

$$C(t) = \lim_{T \rightarrow \infty} \frac{1}{T} \cdot \int_0^T I(t') \cdot I(t'+t) dt'$$

where $I(t)$ is the intensity at time t . Thus its value at delay t indicates how the intensities measured t units apart relate to each other. It reveals a "memory effect" inherent in the intensity signal. N.B. if the light intensity has a Poisson distribution, i.e., no "memory", the correlation function for $t > 0$ is simply a constant. The correlation function is usually normalized such that this constant becomes unity:

$$G(t) = \lim_{T \rightarrow \infty} \frac{\frac{1}{T} \cdot \int_0^T I(t') \cdot I(t'+t) dt'}{\left(\frac{1}{T} \cdot \int_0^T I(t') dt' \right) \left(\frac{1}{T} \cdot \int_0^T I(t'+t) dt' \right)} \quad (1)$$

It can be easily verified that if $I(t')$ and $I(t'+t)$ are independent, the average of their product equals the product of their averages (which are equal), so the numerator equals the denominator, and $G(t>0) = 1$ as promised.

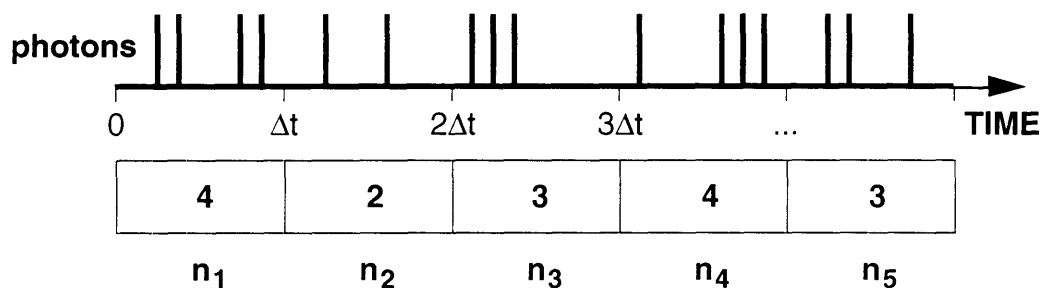


Fig. 1 A discrete time series constructed from photon pulse train. The number of pulses counted in i^{th} interval of width Δt becomes the i^{th} number in the series (n_i).

1.2.2 Discrete Approximation

A digital autocorrelator computes a discrete approximation to the continuous correlation function defined above. The first step is to digitize $I(t)$. This is easy, because most often the input to the correlator is a train of pulses corresponding to photons arriving at the detector. Thus, as an approximation to $I(t)$, a time series n_i is formed (see Figure 1) where $n_i = [\text{number of pulses detected between } t=(i-1)\Delta t \text{ and } t=i\Delta t]$. One then computes the raw correlation function (this is the job of the autocorrelator):

$$C_k = \sum_{i=1}^M n_i \cdot n_{i+k} \quad (2)$$

It can be normalized analogously to $G(t)$ above:

$$G_k = \lim_{M \rightarrow \infty} \frac{M \cdot \sum_{i=1}^M n_i \cdot n_{i+k}}{\left(\sum_{i=1}^M n_i \right) \cdot \left(\sum_{i=1}^M n_{i+k} \right)} = \lim_{M \rightarrow \infty} \frac{M \cdot C_k}{S_0 \cdot S_k} \quad (3)$$

where C_k is defined above and S_0, S_k are defined by

$$S_k = \sum_{i=1}^M n_{i+k} \quad (4)$$

Note that we distinguish between S_0 and S_k . Ideally (i.e., for infinite M) they are equal, but the difference becomes important when M is finite (as in any real-life implementation). This will be further discussed below. (N.B. at $M=1$ we have $C_k=S_0 \cdot S_k$.)

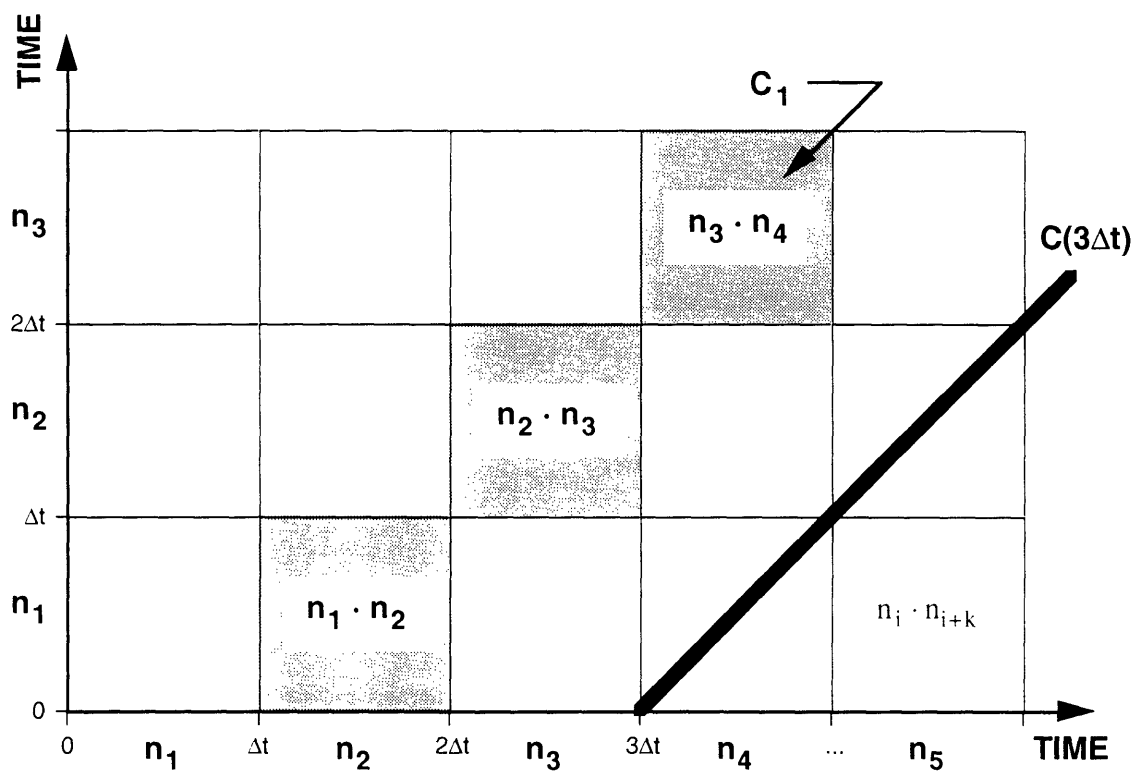


Fig. 2 Graphical representation of the correlation function $C(t)$ and its approximation C_k . Each square's side represents the photon count in a corresponding interval. Thus the square itself represents the product of the sides' counts. The discrete approximation C_k is formed by the sum along a diagonal. The continuous correlation function $C(t)$ can be represented by a line.

1.2.3 Graphical Representation

Figure 2 shows a graphical representation of the construction of the correlation function and its approximation. The horizontal and the vertical axes represent increasing time. Each segment $(t, t+\Delta t]$ on either axis "holds" the photons collected during that interval, i.e., it represents

$$\int_t^{t+\Delta t} I(t) dt$$

The area of each square in the plane represents the product of intensities "held" by its sides. The squares of side Δt along each 45° line displaced k units from the origin correspond then to the products $n_i \cdot n_{i+k}$, thus their combined area represents the raw correlation function C_k . Clearly, as $\Delta t \rightarrow 0$, this approximates the continuous correlation function $C(t)$, so the continuous function corresponds simply to the 45° line displaced by a delay t from the origin.

The normalization of G_k becomes intuitively obvious in this scheme (see Figure 3). We have M squares distributed along a diagonal (dark gray) of a big square (lightly shaded). The sums in the denominator of Equation 3 correspond to the sides of this square (since each side "holds" all the photons in the interval of M units, thus corresponds to one of the sums). The diagonal has only M unit squares, while the shaded square has M^2 of them. Thus for proper normalization we need to multiply the numerator by M .

1.2.4 Sources of Errors

The discrete correlation function is only an approximation. Let us consider the errors that can enter into this process. Even before the correlation function is computed, errors are introduced during the process of photodetection. The detector has only a finite efficiency and not every photon produces a pulse. Furthermore, each detection is followed by a dead time. Dead time means that if two photons arrive too close to each other, the second one will not be detected. This introduces a negative correlation at short delay times. Finally, there is a probability of an afterpulse – one photon can trigger several pulses. This enhances the correlation at short delay times. The errors of interest here are due to the discretization process itself. They are discussed below.

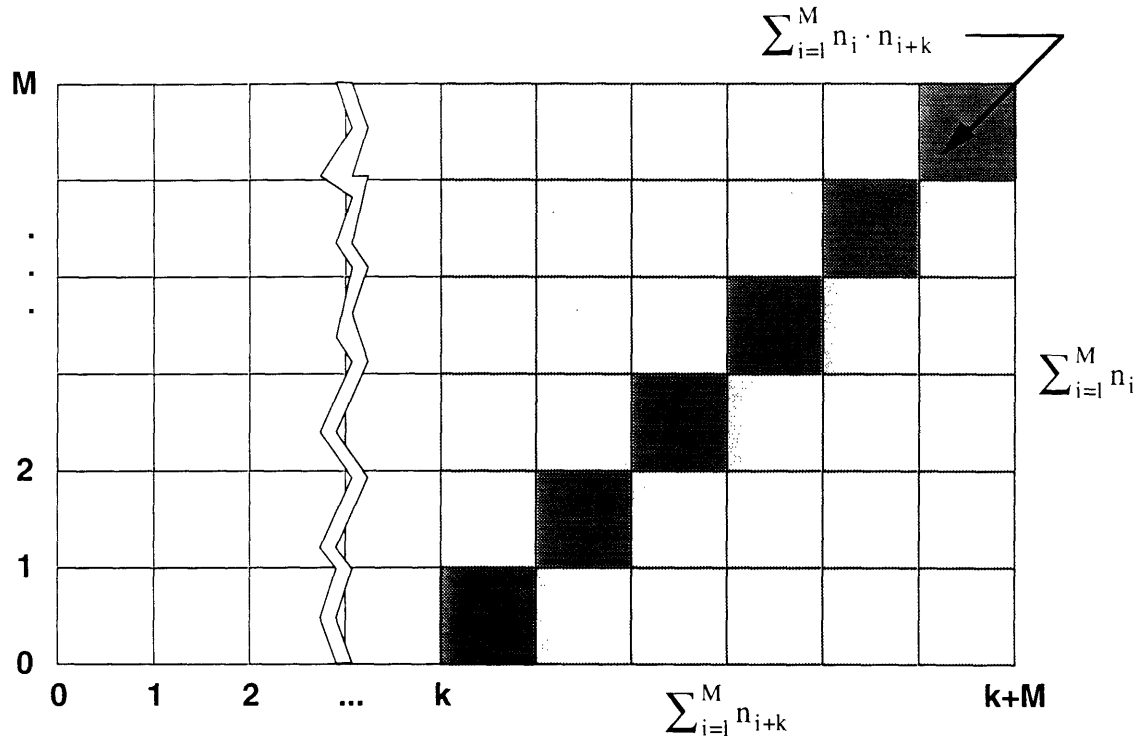


Fig. 3 Graphical illustration of the correlation function's normalization. The dark squares represent the raw correlation C_k . The sides of the lightly shaded square represent the intensity sums S_0 and S_k . This square is then their product. Its area is M times bigger than the diagonal's. As the normalized correlation function has to be dimensionless, it is formed as $G_k = M \cdot C_k / S_0 \cdot S_k$.

1.2.4.1 Decimation

Standard implementation of a correlator uses registers to hold the delayed values of n_j . The registers have a limited size, usually 4 (or 8) bits. Thus if the count rate exceeds 16 (or 256) counts per channel width the data has to be decimated (for example by throwing away every second pulse), which decreases the accuracy. In this scheme the multiplication is replaced by repeated addition each time a new photon arrives, thus there is no further error introduced from that direction. Hence these correlators are called $4 \cdot N$ or $8 \cdot N$. In the correlator described here each n_j is stored in a 32 bit buffer, so one would need to register more than $4 \cdot 10^9$ counts per channel width to experience an overflow. Thus the discrete correlation can be computed losslessly.

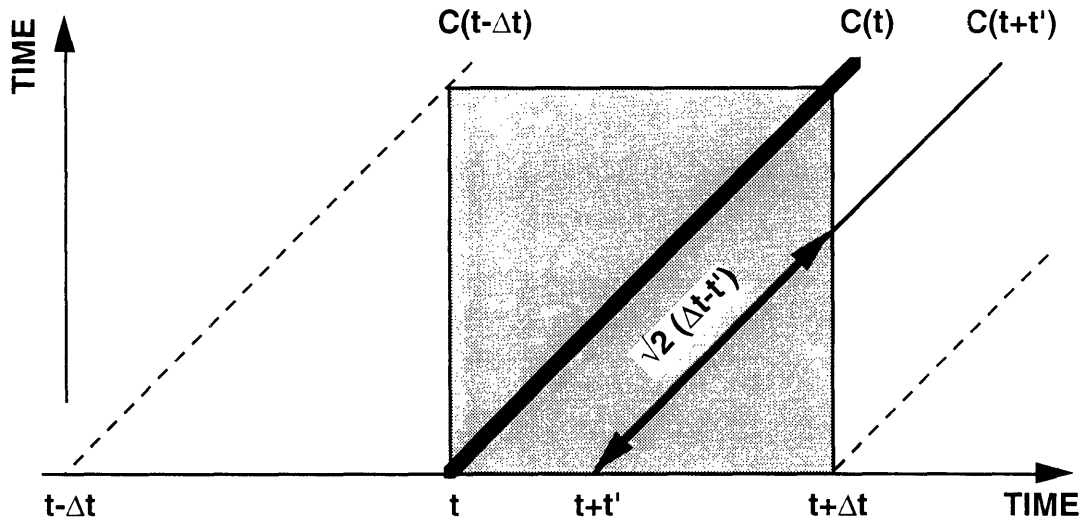


Fig. 4 Construction for estimating the difference between the continuous correlation function $C(t)$ and the discrete approximation $C_{t/\Delta t}$. The discrete approximation (the square) can be evaluated by integrating the diagonals ($C(t+\tau)$) weighted by the length of their intersection with the square (the arrows). The times between $t-\Delta t$ and $t+\Delta t$ have to be considered (dashed lines).

1.2.4.2 Discretization

Let's examine the error introduced by the discrete approximation. As explained above, in our graphical representation discrete correlation is represented by the sum of all tiles on one diagonal. Figure 4 shows the construction for evaluating the approximate (discrete) correlation function from continuous ones (given some simplifying assumptions, e.g., that the correlation function does not change in time). As before, the 45° diagonals represent the true (continuous) correlation function values at times corresponding to their intersection with the lower edge, whereas the square represents the approximate (discrete) value $\tilde{C}(t) \equiv C_{k=t/\Delta t}$ and is the average of different $C(t)$'s intersecting it. We compute it by summing the upper and the lower triangles:

$$\tilde{C}(t) = \frac{1}{\Delta t^2} \left(\int_0^{\Delta t} C(t-t') \cdot \sqrt{2} (\Delta t - t') \cdot \frac{dt'}{\sqrt{2}} + \int_0^{\Delta t} C(t+t') \cdot \sqrt{2} (\Delta t - t') \cdot \frac{dt'}{\sqrt{2}} \right)$$

$$= \frac{1}{\Delta t^2} \int_0^{\Delta t} (C(t-t') + C(t+t')) \cdot (\Delta t - t') \cdot dt'$$

We can get some idea about the magnitude of the difference $\tilde{C}(t) - C(t)$ by expanding $C(t)$ in a Taylor series:

$$C(t + \delta t) = C(t) + C'(t) \cdot \delta t + \frac{1}{2} C''(t) \cdot \delta t^2 + \dots$$

Plugging this in we obtain

$$\begin{aligned} \tilde{C}(t) &= \frac{1}{\Delta t^2} \int_0^{\Delta t} (2 C(t) + C''(t) \cdot t'^2) \cdot (\Delta t - t') \cdot dt' \\ &= C(t) + C''(t) \cdot \Delta t^2 / 12 \end{aligned}$$

Thus the difference is directly related to the curvature. If the function does not bend too much within the period Δt , the accuracy should be good. A more illustrative example is to look at a typical homodyne correlation function of the form $C(t) = e^{-2t/\tau}$. Plugging it in we obtain

$$\begin{aligned} &= \frac{1}{\Delta t^2} \int_0^{\Delta t} (C(t-t') + C(t+t')) \cdot (\Delta t - t') \cdot dt' \\ \tilde{C}(t) &= \frac{1}{\Delta t^2} \int_0^{\Delta t} [e^{-2(t-t')/\tau} + e^{-2(t+t')/\tau}] \cdot (\Delta t - t') \cdot dt' \\ &= e^{-2t/\tau} \cdot \frac{1}{\Delta t^2} \int_0^{\Delta t} 2 \cosh(2t'/\tau) \cdot (\Delta t - t') \cdot dt' \\ &= C(t) \cdot \frac{\tau^2}{\Delta t^2} \cdot \sinh^2\left(\frac{\Delta t}{\tau}\right) \end{aligned}$$

So the ratio $\tilde{C}(t) / C(t)$ depends only on the quantity $r = \Delta t / \tau$ and equals

$$\tilde{C}(t) / C(t) = \left(\frac{\sinh r}{r} \right)^2$$

which for small r is very close to 1. In fact, the expansion about 0 gives

$$\tilde{C}(t)/C(t) = 1 + \frac{r^2}{3} + \frac{2r^4}{45} + \dots$$

so even for $r=0.1$ the deviation is only 0.3%. Thus it is important to keep the channel width Δt small compared to time scales involved in the problem.

1.2.4.3 Finite Collection Time

Another source of errors arises from the finite collection time. This is especially true for the large width channels. For example, a channel of 10s width is updated only once every 10s. Thus for a one minute run it will be updated at most 6 times (less in reality, since there is also a delay time before the channel is first accessed). The errors introduced by finite collection time are reduced by using symmetric normalization introduced by Schätzel et al. (3). This is nothing else than normalization with $S_0 \cdot S_k$ rather than with $(S_0)^2$, which would be easier from the technical point of view (because less information needs to be kept track of). Reader is referred to (3) for a thorough analysis of finite collection time errors with and without symmetric normalization.

1.3 SOFTWARE DESIGN

The correlator described here is implemented mostly in software (except for the hardware that counts the incoming pulses and transfers them to computer's memory).

1.3.1 Why Logarithmic?

Computational power necessary to calculate the correlation function is related to the number of squares (see Figure 1) composing the correlation function. Each square represents one multiplication and one addition. Thus the required number of operations per unit time is directly proportional to the number of channels (as each channel must be computed separately), but inversely proportional to the square side (Δt). Doubling the channel width Δt halves the number of squares per unit time hence halving the number of operations required to compute that channel. This fact, along with a property of the sum of a geometric series of the powers of 2, allows for a construction of a correlator in which

the channel width is doubled every several channels. The design described here uses blocks of 8 channels. So if the width of channels 1 to 8 is $10\mu\text{s}$, channels 9 to 16 have a width of $20\mu\text{s}$, channels 17 to 24 – $40\mu\text{s}$, 25 to 32 – $80\mu\text{s}$, etc. Thus if n instructions per second are needed for the channels of the first block, $n/2$ are needed for the second, $n/4$ for the third, $n/8$ for the fourth, etc. The sum of such a geometric series converges:

$$n + \frac{n}{2} + \frac{n}{4} + \frac{n}{8} + \dots = 2n$$

Thus the total required computing power, even for an infinite number of channels, is equal to that needed for two linear blocks.

1.3.2 Principle of Operation

For the sake of simplicity in the following discussion it will be assumed that each of the blocks has only four (rather than 8) channels. The graphical representation of the logarithmic correlation process is presented in Figure 5.

The data structures needed to hold all the necessary information for computing the correlation function are described below. To better reflect this computation, the indices in the Equation 2 can be rewritten as:

$$C_k = \sum_{i=k+1}^{M+k} n_i \cdot n_{i-k} \quad (5)$$

This demonstrates that to calculate C_k in real time we need to keep track of k past values of n_i . This is implemented using a shift register – an entity where during each cycle the new data comes in on one side and the old data is pushed out on the other. There is one cell (from now on referred to as n_k) for each channel of the block. The last two values pushed out are added together in a "limbo" and subsequently fed into the shift register of the next block, reflecting the fact that the next block doubles the channel width. Of course shifting of this higher block will be only half as frequent as that of the lower one (that is why we need the "limbo" to hold the intermediate value). N.B. the presence of the "limbo" corresponds to the white squares in Figure 5 where no correlation is collected between the blocks.

Another structure is needed to hold the currently arriving data. Again, the problem is complicated by the fact that each block doubles the channel width, so we need a separate n_0 register (as it will be subsequently referred to) for each block. Analogously

to the n_k case, two consecutive values from one block's n_0 register are added together and placed into next block's n_0 register reflecting the fact that the next block's channels are two times wider.

Next we need a way of keeping track of the sums S_0 and S_k (defined in Equation 4) which occur in the denominator of Equation 3. In this implementation each channel starts collecting data at a different time, so each of the sums for each of the channels runs over a different set of numbers. This forces us to keep two sets of registers for each channel (that's why the symmetric normalization is more difficult to implement). In practice, only one register per block is being updated for each sum (as opposed to one per channel). The correction for each channel is pre-computed and stored separately.

Finally we need to keep track of the number of cycles (M) for each channel (different for each one of them). This can be deduced from the total number of steps taken and thus only one number needs to be kept.

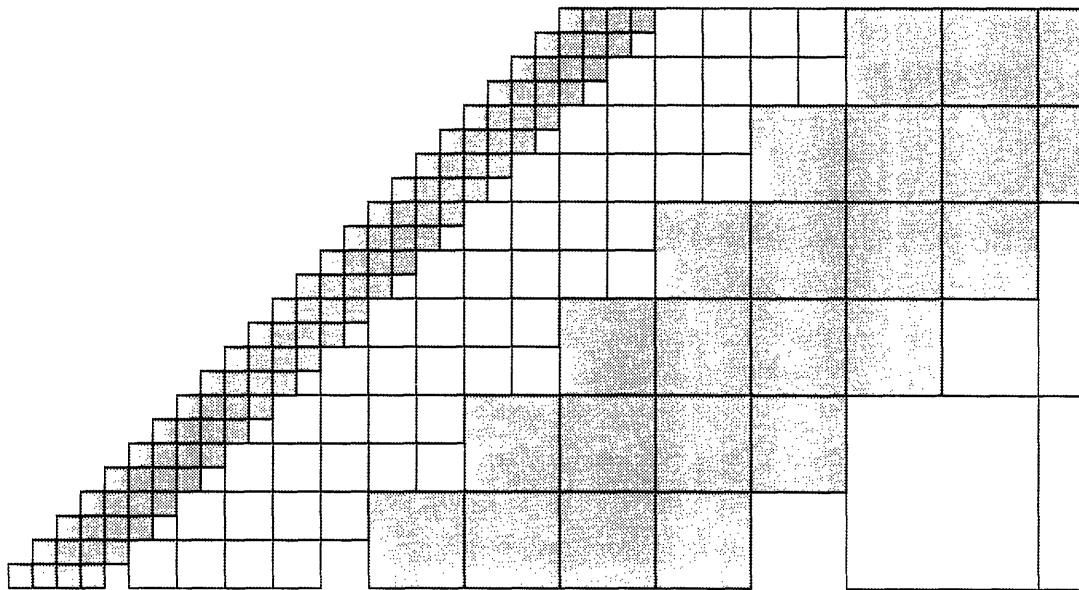


Fig. 5 Schematic representation of the logarithmic correlation. Course graining is introduced here by doubling the channel width every four channels (marked by different shades of gray). The number of computations per unit time (each square represents one computation) is halved by this operation. Since the sum of powers of $1/2$ is twice the first term, the total computing power required is just twice that needed for the first four channels.

1.3.3 Main Loop

The heart of the correlator consists of a loop which between two incoming data values has to do the following:

- Read new data from the hardware (waiting for its arrival, if necessary)
- Process the eight channels of the first block
- Decide which block to process next
- Process that block's eight channels
- If necessary, update the screen display

Let's look at this process in some more detail. The hardware writes data into a circular buffer in the main memory using a DMA (Direct Memory Access) channel. This buffer is large enough to store the incoming data for a while when the processor is busy doing other tasks, such as updating the screen.

Several tasks of the main loop are repetitive in nature (e.g., processing each of the 8 channels), but to conserve time they are coded explicitly (rather than being put in a loop). For each block the task is as follows:

- Get the "current" value – n_0
- Multiply it by each of the 8 n_k 's, accumulating the result in channel C_k and shift the n_k 's by 1 (reflecting the time flow). A value from this block's "limbo" is shifted in, and the "limbo" is cleared. The n_k shifted out is added to next block's "limbo".
- Add this n_0 to next block's n_0 , and clear this block's n_0
- Update this block's S_0 .

The order of updating different blocks (illustrated in Figure 6) is designed in a form of a binary tree. In this scheme each block is accessed exactly half as often as the block below it. Moreover, it is accessed in a moment when all the other blocks need to be idle.

One point on the screen is updated every 64 loop repetitions. A normalized correlation function is calculated and plotted by writing directly to the video memory. The incoming data is buffered so it can be absorbed while the screen is updated (which is a relatively slow operation).

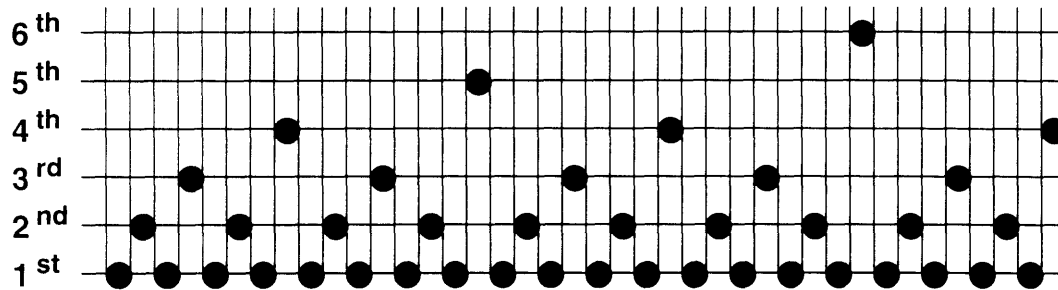


Fig. 6 The order of operations. The vertical axis has the block numbers (for each block of 8 channels). The horizontal line represents the processing sequence (time). This binary tree ordering ensures that each level is processed half as often as the previous level, while not disrupting the operation of any of the levels below.

1.3.4 Initialization

Besides a trivial initialization – clearing all the storage areas – there are several more subtle points that need to be addressed. They are caused by the fact that not all the channels are started at the same time. This is a "feature" rather than a "bug", since if all the channels were to start at once, we would have to wait for a time equal the longest delay (up to several hours), before obtaining any results. Therefore it is better to start each channel as soon as its delay is reached. This means that the sums S_0 and S_k are different for each channel. As explained before, to conserve time they are not updated for every channel, but once per block. That means that the correction for each channel must be computed during initialization. To this purpose a variable is kept which marks the block being initialized. Blocks below this level are processed as explained before, blocks above this level are ignored (their delay has not been reached yet), and blocks at this level are initialized one channel at a time. This introduces another subtle point. The sequence of processing the blocks (the binary tree in Figure 6) must be started at such a point that after the last channel of the first block was initialized, the next channel accessed is from the second block. The same should hold true for the second, third, etc., blocks. Interestingly, there is one unique starting point that guarantees this.

Another aspect of the initialization is reading the entire program and its data areas into microprocessor's on-board cache, so it can execute without external (slow) memory references. This provides a significant speed gain.

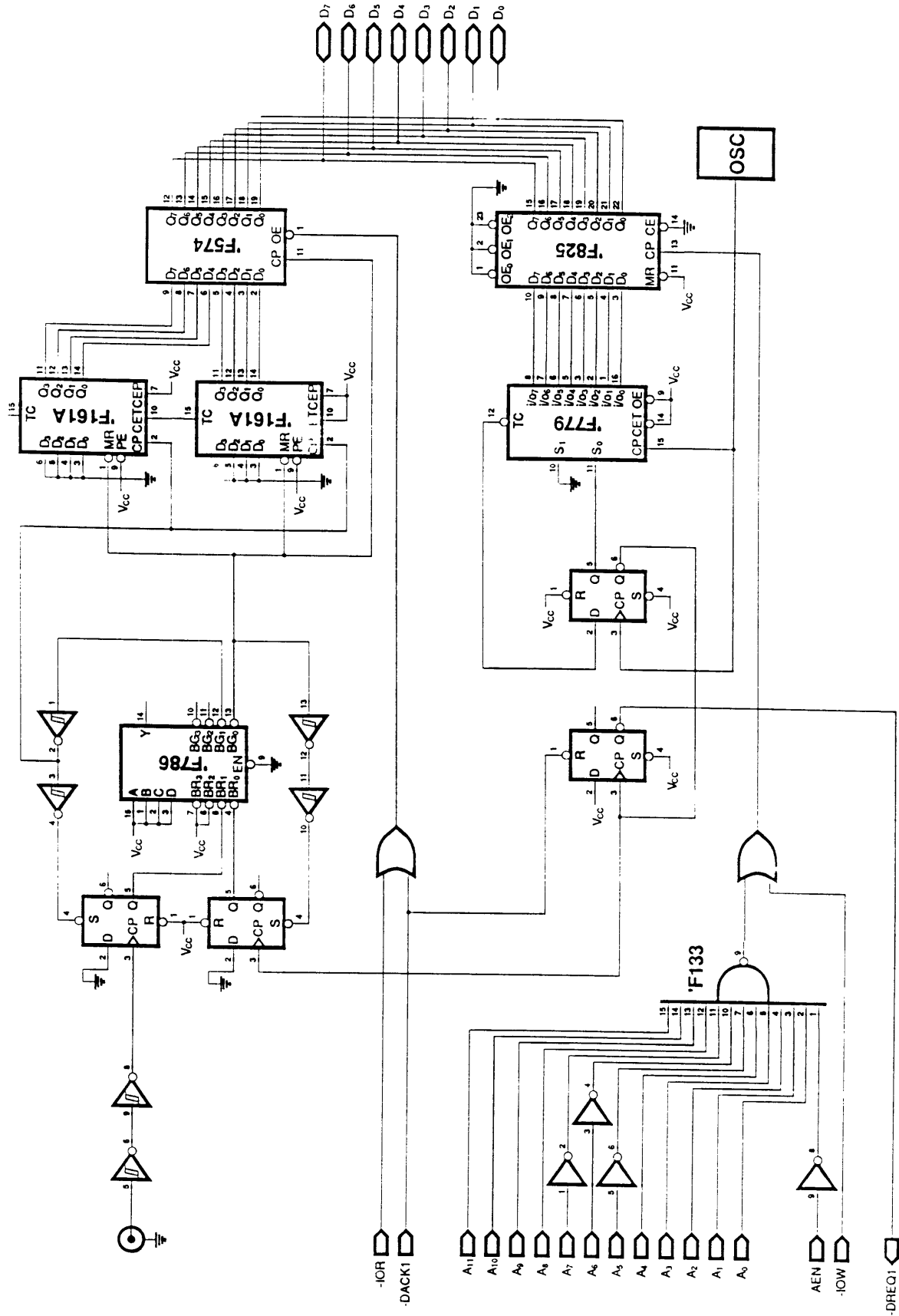
1.4 DATA COMPRESSION

Once the correlation function has been collected, it needs to be stored for future analysis. However, the full description of the correlation function involves a significant amount of data. At each channel we have four numbers to keep track of (C_k , S_0 , S_k and M). In addition the channel's delay is essential, and the width is also useful. For a 200 channel correlation function this information would take up 4 kilobytes. If this is multiplied by 150 different positions needed to compute an ensemble average at given conditions (600kB), and by the number of different conditions, the storage requirement is large. A solution is to compress the data. The algorithm used performs a lossy compression – some of the accuracy is lost, but it is much smaller than the inherent statistical error in data. The delay, the width, and the count M can be derived for each channel from a few parameters. Thus it is only necessary to store these parameters, rather than entire arrays of numbers. The other three items (C_k , S_0 , S_k) are normalized into smooth variables G_k , I_0 , I_k , where G_k was defined before (Equation 2) and I_0 , I_k are intensities (in counts/ms) derived from S_0 , S_k . All three are compressed into 32 bits per channel – 12 bits for G_k , and 10 each for I_0 , I_k . The intensities are stored as a difference from the first channel (which is stored explicitly), while G_k is stored as a second derivative – deviation of each point from the line extrapolated from previous two points. It is further weighted by $M^{-1/2}$, reflecting the Central Limit Theorem statistics governing channel counts. In this way the storage requirement is reduced almost fivefold.

1.5 HARDWARE DESIGN

As the core of the correlator is implemented in the software, the hardware is reduced to a minimum. Nevertheless, the external signals need to be somehow presented to the software, so some form of external interface is needed. The following section describes first the exact task of the interface, and then its design and implementation.

Fig. 7 (Opposite page) Schematic diagram of the hardware interface.



1.5.1 Task of the Interface

The input to the correlator is a series of TTL pulses corresponding to photon detection events. These pulses are by nature asynchronous, so they need to be synchronized with the on-board clock. The software expects to receive, during each consecutive delay time, the total number of pulses arriving during that delay time. Thus each delay period the pulses need to be counted, and then made available to the host computer. After that, the pulse counter has to be cleared, and another delay period started.

The transfer to the computer's memory is implemented through a DMA (direct memory access) channel (see Reference (4) for details about DMA transfers). Each time the hardware card is ready to transmit data (once every $12.8\mu\text{s}$), it issues a DMA request. It is given high priority because the data will be overridden with the next ones if not read on time. The DMA controller reads the count from the hardware card, acknowledges the DMA transfer, and places the data in a ring buffer where the correlator program can fetch it. This allows the processor to receive the data with only two accesses to external (slow) memory (the second access is to mark the buffer location empty).

The only other part of the hardware is the programmable timer, which determines the basic channel width. It is programmed by writing the delay (in multiples of $0.2\mu\text{s}$) to I/O port number $1F1_{16}$.

For the interested reader, Figure 7 shows the actual hardware schematic diagram.

1.5.2 BI-2030AT as a Front End

A serious problem of this correlator design is that the shortest achievable channel width is about $12\mu\text{s}$. This is enough in some cases, but usually one wants to know the correlation function at even shorter times. A solution would be to build a dedicated hardware that performs operations analogous to the software correlator, but for channel widths less than $12\mu\text{s}$. It wouldn't need to be very sophisticated, since it wouldn't require more than 4 bit resolution (the count rate that would cause an overflow at these delay times would first saturate the photomultiplier), and it could relay on the software part to do most of the work.

An even easier solution was found by using an existing Brookhaven Instruments BI-2030AT linear correlator as the front end. It is operated with a channel width of $0.8\mu\text{s}$. The values of first 16 channels are left unchanged, while higher channels are grouped by 2's, 4's, 8's, etc., to reflect the mode of operation of the software correlator.

Altogether the 136 linear channels of BI-2030AT yield 40 logarithmically spaced channels. Further channels are implemented in the software correlator (they are delayed to reflect the proper position of the 41st channel). Pulses arriving into the hardware card are routed through BI-2030AT to make sure that both correlators count exactly the same pulses (otherwise there would be a discontinuity between 40th and 41st channels). Thus the combination of BI-2030AT and the software correlator is capable of collecting simultaneously channel widths from 0.8 μ s to ~10,000s (with 256 channels).

1.6 ANALYSIS SOFTWARE

As a part of complete system for performing light scattering from gels, programs were developed to calculate the ensemble average of the data, and to analyze the results. Both parts are briefly described here.

1.6.1 Ensemble Averaging

As it will be explained in Chapter 2, an important part of performing light scattering experiments with gels consists in estimating the ensemble average of the correlation function. One way of doing this (adopted in this thesis) is to measure the correlation function at various points, and then to average the result. A program is provided which does this task automatically, given a file with raw data from a set of different positions. It also provides a way of eliminating faulty points (e.g., dust in the sample). Ensemble averaging of raw data from M different points p is carried out by first forming a sum:

$$C_k^N = \sum_{p=1}^N C_k^{(p)}$$

where C_k^N is the average of N points, and $C_k^{(p)}$ is the raw data collected at point p. S_0^N , S_k^N , and M^N are defined analogously. Then, in an exact analogy to Equation 2, we compute

$$G_k^N = \frac{M^N \cdot C_k^N}{S_0^N \cdot S_k^N}$$

which is a finite N approximation to the normalized ensemble averaged correlation function. This correlation function is then saved again in the same compressed format as described above. Correlation functions obtained at different conditions can be combined in a single file, and later analyzed together.

1.6.2 Curve Plotting and Fitting

Another program is provided to plot and analyze the correlation functions. Nonlinear multiple parameter fitting routines (Levenberg-Marquardt method) were adopted from Reference (5) to fit the correlation functions with one of several models. Some of the models available are

$$f_{\text{sng}}(t) = A \cdot e^{-2t/\tau} + B$$

for a homodyne fit to intensity-intensity correlation function;

$$f_{\text{dbl}}(t) = A \cdot \left(\frac{e^{-t/\tau_1} + R \cdot e^{-t/\tau_2}}{1 + R} \right)^2 + B$$

for a double exponential fit (homodyne spectrum assumed) – useful to model systems with two inherent time scales;

$$f_{\text{mx2}}(t) = A \cdot \left(\frac{e^{-t/\tau_1} + R \cdot e^{-t/\tau_2}}{1 + R} \right) + B$$

a mixture of two exponentials – useful in estimating the effect of homodyne and heterodyne mixing (one decay time should be twice the other); and

$$f_{\text{spw}}(t) = A \cdot e^{-t/\tau} + C \cdot (t^2 + t_0^2)^{-d/2} + B$$

which is a single exponential plus a power law (corrected not to diverge at $t=0$).

The analysis software is designed to perform automatic curve fitting to a number of correlation functions residing in a single file, and produce a table of fit parameters for all correlation functions. This data can be later analyzed for dependence on conditions under which the scattering was performed.

SUMMARY

This chapter presented a design of an instrument capable of obtaining correlation functions with logarithmically spaced delays ranging from $0.8\mu\text{s}$ to several hours, simultaneously. The core of the correlator is implemented in software executing entirely inside the on-chip cache of an Intel 486DX50 microprocessor. The hardware interface card is implemented for counting the incoming photon pulses and transferring them into the computer's memory in regular intervals. A commercial linear correlator is used as a front end to obtain low delay times. This simplifies the hardware design, which would otherwise need to compute short delay time correlations (inaccessible to the software correlator). Correlated data is displayed in real time on screen, and written to disk in a compressed format to conserve space. Data from a number of different locations can be combined to form an approximation to the ensemble average. Averaged data for different gel conditions can be combined and analyzed together.

REFERENCES

- [1] Chu, B.: *Laser Light Scattering*, Academic Press, London (1991).
- [2] Berne, B.J. and Pecora, R.: *Dynamic Light Scattering*, Wiley & Sons, New York, (1976).
- [3] Schätzel, K., Drewel, M., Stimac, S.: *J. Mod. Opt.*, **35**, 711 (1988).
- [4] Sargent, M. and Shoemaker, R.L.: *The IBM Personal Computer From the Inside Out*, Addison-Wesley, Reading, MA, (1986).
- [5] Press, W.H., Flannery, B.P., Teukolsky, S.A. and Vetterling, W.,T.: *Numerical Recipes*, Cambridge University Press, Cambridge, (1986).

CHAPTER 2

LIGHT SCATTERING FROM NON-ERGODIC SYSTEMS

The goal of this chapter is to introduce a theoretical and practical basis for analyzing dynamic light scattering from non-ergodic media. It establishes procedures that will be used extensively throughout the rest of this thesis to analyze the raw light scattering data and for interpreting the results. This chapter consists of four parts. The first section gives an overview of ergodicity and nonergodicity. Several key concepts, such as ensemble and time averages are reviewed. The first section also discusses light scattering from ergodic and nonergodic media, reviewing the basic concepts and comparing time and ensemble averaged intensity correlation functions for various classes of systems. The second section deals in more detail with ways of extracting an ensemble averaged correlation function from a set of time averaged correlation functions (the measured data). It derives the procedures to be used in further chapters for analyzing the data. The third section presents a model for light scattering from gels, which combines theories of Pusey and van Megen (1) and Tanaka, Hocker and Benedek (2). It provides basis for interpreting the light scattering results. Finally the fourth section presents some simple experimental results that illustrate the points made in the previous sections.

2.1 OVERVIEW OF (NON)ERGODICITY

A system is said to be ergodic if time and ensemble averages of physical quantities associated with that system are identical (see, e.g., (3)). Before exploring this definition it is important to understand the distinction between the two averages.

2.1.1 Ensemble vs. Time Average

Figure 1 (after (3)) schematically represents the meaning of time and ensemble averages of some quantity $F(t)$. We divide the system into subensembles (labeled by index p) much larger than molecular length scales (so the statistical treatment applies to each subensemble), but also much smaller than the macroscopic size of the system (so that the collection of all subensembles can in turn be treated statistically). We then consider the time evolution of F for each subensemble p : $F_p(t)$. The time average can be expressed as

$$\langle F_p(t) \rangle_T = \lim_{T \rightarrow \infty} \frac{1}{2T} \int_{-T}^T F_p(t) dt$$

while the ensemble average is

$$\langle F_p(t) \rangle_E = \lim_{N \rightarrow \infty} \frac{1}{N} \int_0^N F_p(t) dt$$

N.B. these two averages commute, so

$$\langle \langle F_p(t) \rangle_E \rangle_T = \langle \langle F_p(t) \rangle_T \rangle_E$$

However, if the system is stationary, i.e., it does not depend on the choice of the origin of time (which would be true for any statistical system in equilibrium), the ensemble average will be time-independent, so its time average would equal that value. Under these conditions the equation above can be rewritten as

$$\langle F_p(t) \rangle_E = \langle \langle F_p(t) \rangle_T \rangle_E$$

This equality will be assumed throughout this chapter, and the notation $\langle \dots \rangle_E$ will denote an ensemble average of the time average. In addition, the notation $\langle \dots \rangle_N$ will be used to denote this an average taken over a finite set of subensembles.

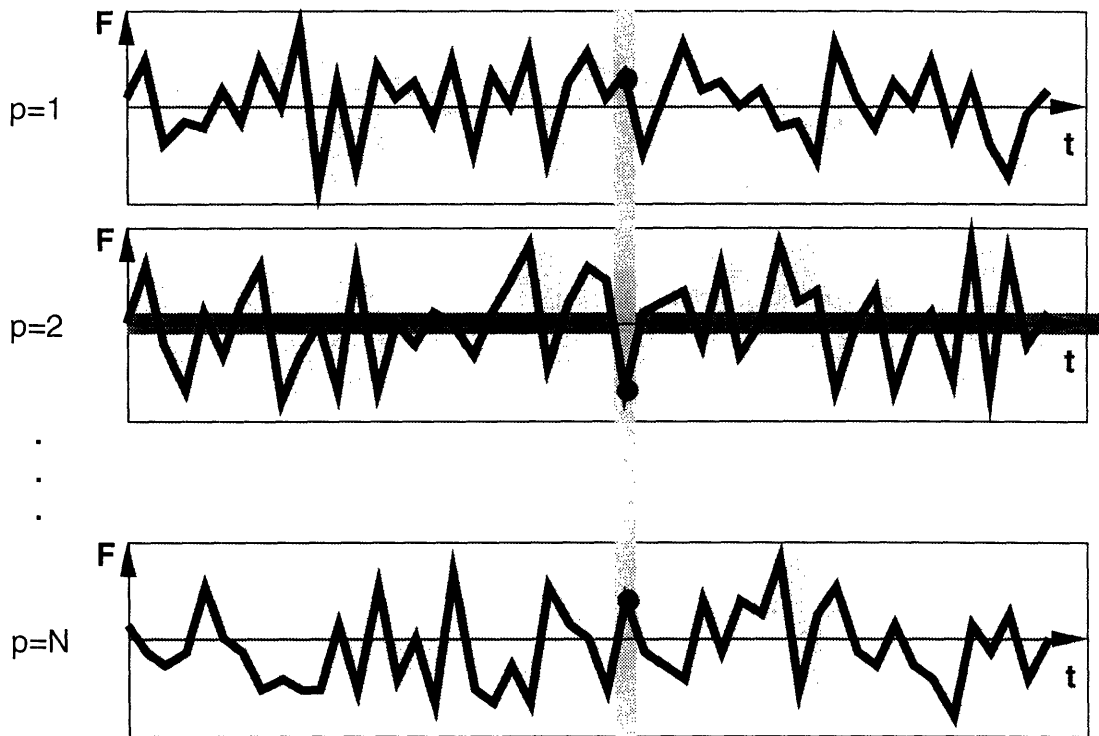


Fig. 1 Illustration of the definition of time and ensemble averages of some quantity F . Different p 's represent different subensembles within of the system. For each p the time average of the quantity F can be computed in an obvious way. The thick horizontal line represents the domain of time averaging for subensemble $p=2$. The ensemble averaging is represented here by the thick vertical line. The value of F at a time t is averaged over all subensembles of the system. The system is said to be ergodic if the time and ensemble averages of F (denoted as $\langle F \rangle_T$ and $\langle F \rangle_E$) are equal. This also implies that the time averages would be equal for all subensembles. This would hold if all the values of F for each subensemble were reachable during the time of measurement. However, this might not be true. For example, due to a difference in the local structure the scattering intensity may be different at each location. Then the time averages of different subensembles would not equal. Note however, that if the system is in equilibrium (i.e., the time origin is not important) the ensemble average $\langle F(t) \rangle_E$ is time-independent, thus equal to $\langle \langle F \rangle_T \rangle_E$.

2.1.2 Ergodic vs. Nonergodic Systems

As mentioned before, a system is called ergodic if its time and ensemble averages are equal, i.e., if

$$\langle F_p(t) \rangle_T = \langle F_p(t) \rangle_E$$

for physical quantities associated with the system. It further implies that the time average is independent of the particular subensemble chosen. This would be the case if within each subensemble F was able to attain all the possible values (or at least a representative set of values) available to it in the whole ensemble.

Some systems fail to be ergodic in the sense described above. They are called nonergodic. If, in each subensemble, F is restricted to a small subset of available values, the time average for that ensemble will be different from the time averages for other ensembles, and the system will be nonergodic. For example, in a gel scattered light intensity can vary from location to location due to some differences in local structure. So for some subensembles (scattering volumes) the average intensity will be high, for others low, and the ensemble average will not, in general, equal any of these time averages.

2.1.3 Light Scattering

As mentioned above, light scattering from a system is affected by the system's ergodicity (or lack thereof). Figure 2 (reproduced from (1)) illustrates the general distinction. The left column shows the normalized time average correlation function of subensemble p , defined as:

$$g_{T,p}^{(2)}(\tau) = \frac{\langle I_p(t) \cdot I_p(t + \tau) \rangle_T}{\langle I_p(t) \rangle_T^2} \quad (1)$$

where $I_p(t)$ is the instantaneous light intensity detected far away from the sample and originating from the scattering volume (subensemble) p . The right column has the normalized ensemble averaged correlation function defined analogously:

$$g_E^{(2)}(\tau) = \frac{\langle I_p(t) \cdot I_p(t + \tau) \rangle_E}{\langle I_p(t) \rangle_E^2} \quad (2)$$

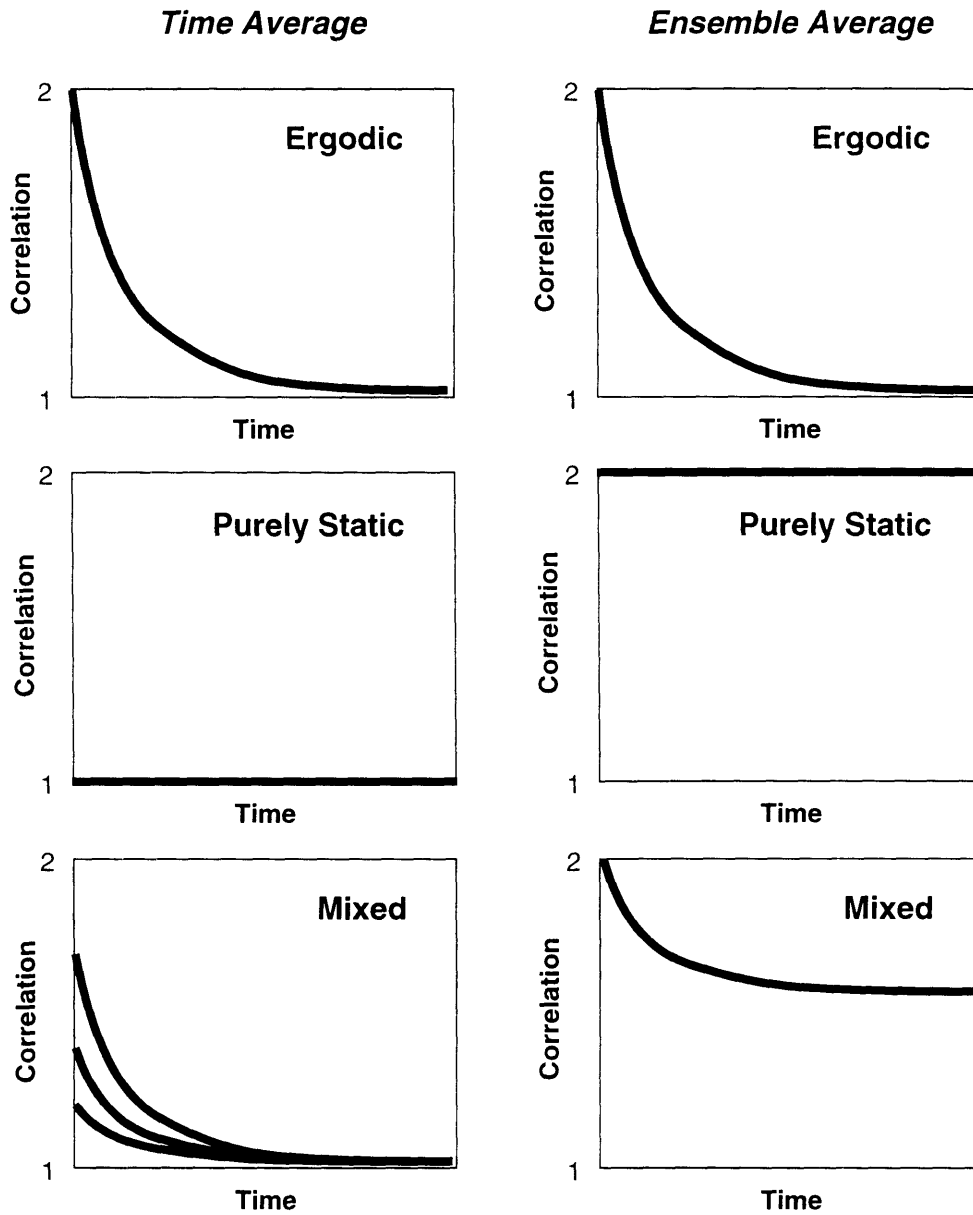


Fig. 2 Comparison of time- and ensemble-averaged intensity correlation functions for various media. The top row shows a fully ergodic medium (e.g., a liquid). In this case both averages are the same. The middle row represents a sample with purely static (i.e., time independent) scattering (e.g., ground glass). Nevertheless, the spatial distribution is Gaussian, which makes the ensemble average equal 2. The bottom row shows a medium with both solid and liquid-like characteristics. The multiple traces of the time average represent correlation at different points in space.

where, as mentioned before, the ensemble average is taken over time averages from the subensembles.

The top row of Figure 2 shows results for an ergodic system. Typical example of such system is liquid solution. Due to the thermal motions of the scatterers, the intensity fluctuates. The intensity values are correlated on a time scale of diffusive motion of the particles within the scattering volume – reflected by a high value of the correlation function at $\tau=0$. It decays quickly as the scatterer motion is uncorrelated at longer times. Clearly for a liquid the scattering should not depend on the particular scattering volume chosen – statistically the scatterers behave identically in any subensemble. Therefore the system is ergodic, as manifested by the identity of time and ensemble averages (left and right panels). For this reason the ergodic behavior will sometimes be referred to as liquid-like.

The middle row shows the other extreme case (see, e.g., (4)). There is no time dependence in this system. It can be modeled, for example, by ground glass. At each position (subensemble) the time averaged correlation function is 1 (no correlation). The intensity varies from position to position, so the ensemble average is not 1. It can be argued (and will be – later in this chapter) that in the case of a zero mean Gaussian distribution of the electric field (which can be expected from this system) the ensemble averaged correlation function is 2. This extreme nonergodic behavior will sometimes be referred to as solid-like.

Finally, the bottom row demonstrates what happens if both effects are mixed (as can be expected in a gel). The left panel shows several time-averaged correlation functions obtained for different subensembles. We note that at $\tau=0$ they never reach the value of 2, as it happened with the liquid. The ensemble average (right panel) has a value of 2 at $\tau=0$, but does not decay to 1 at large times.

It is evident from these considerations that gel manifests some liquid-like and some solid-like behavior. It will be explored further below.

2.2 DETERMINING THE ENSEMBLE AVERAGE

The ensemble average is of interest to a researcher, but an experiment measures the time average. A way to convert from the latter to the former has to be devised. In the context of light scattering we are talking about going from time-averaged to ensemble-averaged correlation functions. This section starts with a discussion of the possible approaches, and then proceeds to explain the details of the approach used in this thesis.

2.2.1 Different Approaches

Much recent literature has dealt with the light scattering from gels as non-ergodic systems (1, 5-8). Aside from neglecting the nonergodicity altogether (justifiable if the nonergodic effects are weak), two methods are generally used to determine the ensemble average. The first, "brute force" method approximates the true ensemble average by summing raw correlation data obtained at a number of separate points within the gel. For an increasing number of samples this result approaches the true ensemble average. The main drawback is the time that is required to collect data at each point. For this reason many authors (1,5-7) prefer a more recent approach, following the theoretical work of Pusey and van Megen (1). The main idea here is to try to extract all the relevant information from the time average correlation function collected at a single point, correcting it with the ensemble average of scattered intensity (which is much easier to obtain than the correlation function). The details of this procedure can be found in (1). The ensemble average obtained in this way closely (but not exactly) matches the correlation function computed by averaging over different positions.

This thesis follows the first of the two methods – the "brute force" approach. It was chosen for several reasons. First, having at my disposal a system equipped with a stepper motor to move the sample made it easy to collect data at different locations. Second, averaging over many correlation functions is "safer" than relying on a single one. If something goes wrong, the faulty point can be excluded. For example, I often observed that the speckle pattern (and thus the correlation function) would drift slightly on the time scale of minutes, so prolonged measurements would be inaccurate. However, to obtain good statistics the correlation data had to be collected over a long time (N.B. this was precisely the argument against the "brute force" method, though in a different context). A possible solution would be to break the measurement into a series of shorter ones. In such case why not move the sample in the process?

Finally, the following consideration shows how the total time in the "brute force" method needs not be much different from the single point approach. Let's first examine the time necessary to obtain good statistics. Let $C[i]$ be a random variable corresponding to i^{th} channel's raw correlation data. In general, the law of large numbers provides that

$$\text{Var}(C[i]) \cong \bar{C}[i]$$

where $\bar{C}[i]$ is the average value, which is proportional to the collection time. From this the relative deviation is

$$\frac{\sigma(C[i])}{\bar{C}[i]} \cong \frac{1}{\sqrt{\bar{C}[i]}}$$

(a fact that is experimentally demonstrated in Figure 3). Thus to get a good statistics one has to wait until $C[i]$ is high. Now consider the sum

$$C_N[i] = \sum_{p=1}^N C_p[i]$$

where p denotes different positions (different scattering volumes). Of course each $\bar{C}_p[i]$ is different, but the Central Limit Theorem tells us that the average is

$$\bar{C}_N[i] = \sum_{p=1}^N \bar{C}_p[i]$$

and the variance again equals the average:

$$\text{Var}(C_N[i]) = \sum_{p=1}^N \text{Var}(C_p[i]) \cong \bar{C}_N[i]$$

Thus by splitting the measurement time into N intervals of length T (each of them too short to give good statistics by itself) taken at different positions we get a distribution that is equivalent to the single measurement of length $N \cdot T$, and in addition we approximate the ensemble average.

2.2.2 Correcting the Effects of Finite Averaging

There is bound to be some discrepancy between the true ensemble average and its approximation obtained by averaging over a finite number of positions. The following discussion focused on two issues: estimating the magnitude of this discrepancy and finding a way to correct it, at least partially. These considerations are based on the theory presented by Pusey and van Megen (1). The first result is that if certain assumptions are satisfied (9), the scattered electric field detected at a far distance from the sample can be decomposed into a dynamic zero-mean Gaussian component (henceforth called the dynamic part) and a constant static component (henceforth called the static part)

2.2.2.1 Underlying Assumptions

Certain conditions must be fulfilled by the system (the sample and the scattering apparatus) so that the decomposition mentioned above be valid (see (1, 9)). These assumptions will be examined here and shown to be compatible with the system in question. In the following let L be the size of the scattering volume, i.e., the part of the sample illuminated by laser and projected onto the detector ($L \approx 5 \mu\text{m}$ in our case). The conditions are as follows:

1. The number of scatterers per scattering volume should be large. In a gel this is not difficult to achieve, since the concentrations we are dealing with are quite high. For example, given a 700mM gel with 1.2% monomers being crosslinkers, our scattering volume would contain about 10^9 chains.
2. L should be much greater than the length scale associated with the scattering vector. This is also easily achieved since for a He-Ne laser and 90° scattering q^{-1} is about 70nm (while $L \approx 5 \mu\text{m}$).
3. The correlation length should be much less than L . In general this should be true, though the assumption may break down at a critical point.
4. The sample should be amorphous on the length scale of L . This should again be true away from the critical point since the gel is transparent, thus amorphous even on the scale of the wavelength of light.

Since these conditions are satisfied, one can argue (1) that the electric field $E_p(t)$ originating from the scattering volume p can be decomposed into a dynamic zero-mean Gaussian component $E_{D,p}(t)$ and a constant static component $E_{S,p}$:

$$E_p(t) = E_{D,p}(t) + E_{S,p} \quad (3)$$

This in turn implies a similar decomposition of the time averaged intensity:

$$\begin{aligned} \langle I_p(t) \rangle_T &= \langle (E_{D,p}(t) + E_{S,p}) \cdot (E_{D,p}^*(t) + E_{S,p}^*) \rangle_T \\ &= \langle E_{D,p}(t) \cdot E_{D,p}^*(t) \rangle_T + 2 \text{Re}[\langle E_{D,p}(t) \rangle_T \cdot \langle E_{S,p}^* \rangle_T] + \langle E_{S,p} \cdot E_{S,p}^* \rangle_T \end{aligned}$$

$$= \langle I_{D,p}(t) \rangle_T + I_{S,p} \quad (4)$$

since $\langle E_{D,p}(t) \rangle_T = 0$. The assumptions made above furthermore imply that the dynamic portion does not depend on the choice of the scattering volume p . Thus from here on the p dependence will be omitted from the dynamic variables (E_D , I_D , etc.). Now E_p is a zero-mean Gaussian variable when taken over the whole ensemble, and so is E_D , thus E_S must also be one.

2.2.2.2 Estimating the Deviation

Armed with this knowledge we can now examine the statistics of the electric field and the corresponding intensity. Since E_D does not depend on p , and its average is 0, we can ignore it when considering the statistics of $E_{S,p}$, so for now we drop both subscripts and remember that the distribution is over different subensembles (p 's). A zero-mean Gaussian probability distribution for the complex electric field amplitude E :

$$P(E) \cdot dE = \frac{1}{\pi \langle |E|^2 \rangle} e^{-E \cdot E^* / \langle |E|^2 \rangle} dE$$

gives the magnitude distribution

$$P(|E|) \cdot d|E| = \frac{1}{\langle |E|^2 \rangle} e^{-|E|^2 / \langle |E|^2 \rangle} 2 |E| d|E|$$

which in turn yields an exponentially decaying intensity distribution ($I = \langle |E|^2 \rangle$)

$$P(I) \cdot dI = \frac{1}{\langle I \rangle} e^{-I / \langle I \rangle} dI \quad (5)$$

This distribution has the following properties: the average is $\langle I \rangle$, while $\langle I^2 \rangle = 2 \langle I \rangle^2$, so the variance becomes $\text{Var}(I) = \langle I^2 \rangle - \langle I \rangle^2 = \langle I \rangle^2$. Now take an average I_N of N such variables I_p at different scattering volumes $p=1, \dots, N$. By the Central Limit Theorem we then obtain

$$\langle I_N \rangle = \langle I \rangle$$

and

$$\text{Var}(I_N) = \text{Var}(I) / N = \langle I \rangle^2 / N$$

so the relative deviation is

$$\delta_N = \sigma(I_N)/\langle I_N \rangle = 1/\sqrt{N}$$

For the values of N used here (N=50 and N=150) we get, respectively, $\delta_{50}=14.1\%$ and $\delta_{150}=8.2\%$.

2.2.2.3 Correcting the Deviation

The next question is how will this incomplete ensemble averaging affect the correlation function and whether we can reliably separate it into static and dynamic contributions.

Let us recall that the ensemble averaged intensity correlation function is

$$g_E^{(2)}(\tau) = \frac{\langle I_p(t) \cdot I_p(t + \tau) \rangle_E}{\langle I_p(t) \rangle_E^2} \quad (2)$$

where $\langle \dots \rangle_E$ denotes an ensemble average and the subscript p indicates different scattering volumes. Since the electric field taken over the whole ensemble is a zero-mean Gaussian variable, we can write, using the Siegert relationship (9):

$$g_E^{(2)}(\tau) - 1 = \beta |g^{(1)}(\tau)|^2 \quad (6)$$

Here $g^{(1)}(\tau) = \langle E_p(t) \cdot E_p^*(t + \tau) \rangle_E / \bar{I}$ is the normalized ensemble averaged electric field correlation function, while β is an instrumental parameter due to spatial integration of the speckle pattern over a finite detector area. It can be determined experimentally by repeating the scattering experiment with the same geometry but using an ergodic medium. Then $\beta = g^{(2)}(0) - 1 = \langle I^2 \rangle / \langle I \rangle^2 - 1$. For optimal results β should be as close to 1 as possible.

The quantity that is actually measured is slightly different:

$$g_N^{(2)}(\tau) = \frac{\langle I_p(t) \cdot I_p(t + \tau) \rangle_{T,N}}{\langle I_p(t) \rangle_{T,N}^2} \quad (7)$$

Here the subscripts T and N explicitly denote that the average is taken first over time T and then over N positions p. We assume that the time T is long enough to be considered infinite, so the only difference from the actual ensemble average comes from the finiteness of N. So

$$\lim_{N \rightarrow \infty} g_N^{(2)}(\tau) = g_E^{(2)}(\tau)$$

Let's expand $E_p(t)$ into dynamic and static parts:

$$g_N^{(2)}(\tau) = \frac{\langle (E_D(t) + E_{S,p})(E_D^*(t) + E_{S,p}^*)(E_D(t+\tau) + E_{S,p})(E_D^*(t+\tau) + E_{S,p}^*) \rangle_{T,N}}{\langle (E_D(t) + E_{S,p})(E_D^*(t) + E_{S,p}^*) \rangle_{T,N}^2} \quad (8)$$

The numerator yields 16 terms. Eight of them (with odd number of E_D 's) average out to 0; three others are constant and give $2\bar{I}_D \langle I_S \rangle_N + \langle I_S^2 \rangle_N$, where

$$\bar{I}_D \equiv \langle I_D(t) \rangle_{T,N} = \langle I_D(t) \rangle_T$$

$$\langle I_S \rangle_N \equiv \langle I_{S,p} \rangle_{T,N} = \langle I_{S,p} \rangle_N$$

$$\langle I_S^2 \rangle_N \equiv \langle I_{S,p}^2 \rangle_{T,N} = \langle I_{S,p}^2 \rangle_N$$

One term represents self-beating (homodyning) of the dynamic part:

$$\langle I_D(t) \cdot I_D(t+\tau) \rangle_{T,N} = \bar{I}_D^2 (1 + \beta |g_D^{(1)}(\tau)|^2)$$

where

$$g_D^{(1)}(\tau) = \langle E_D(t) \cdot E_D^*(t+\tau) \rangle_T / \bar{I}_D \quad (9)$$

is the normalized electric field correlation function of the dynamic part. Finally four terms combine to give the heterodyning of the dynamic part with the local oscillator due to the static part, expressed as:

$$\langle \text{heterodyne terms} \rangle_{T,N} = \langle 2 I_{S,p} \cdot \bar{I}_D \cdot \alpha_p |g_D^{(1)}(\tau)| \rangle_N \equiv 2 \langle I_S \rangle_N \bar{I}_D \beta |g_D^{(1)}(\tau)|$$

Here α_p is the instrumental parameter for the heterodyne term, which in general depends on the particular configuration of scatterers at p. It is assumed here that its ensemble

average yields a value equal to β (the instrumental parameter for the homodyne term). Since the values are close to 1 anyway, the difference between the ensemble average and the average over N points should be negligible.

The average in the denominator of Equation (8) can be written as

$$\langle I_p(t) \rangle_{T,N} = \langle \langle I_{D,p}(t) \rangle_T + I_{S,p} \rangle_N = \bar{I}_D + \langle I_S \rangle_N \equiv \langle I \rangle_N$$

Thus

$$\begin{aligned} g_N^{(2)}(t) &= \frac{\beta \bar{I}_D^2 |g_D^{(1)}(t)|^2 + 2\beta \bar{I}_D \langle I_S \rangle_N |g_D^{(1)}(t)| + \bar{I}_D^2 + 2\bar{I}_D \langle I_S \rangle_N + \langle I_S^2 \rangle_N}{(\bar{I}_D + \langle I_S \rangle_N)^2} \\ &= \frac{\beta (\bar{I}_D |g_D^{(1)}(t)| + \langle I_S \rangle_N)^2 + (\bar{I}_D + \langle I_S \rangle_N)^2 + \langle I_S^2 \rangle_N - (1+\beta) \langle I_S \rangle_N^2}{(\bar{I}_D + \langle I_S \rangle_N)^2} \end{aligned}$$

Introducing $R_N \equiv \bar{I}_D / \langle I \rangle_N$ (and $1 - R_N \equiv \langle I_S \rangle_N / \langle I \rangle_N$) we can transform this into

$$g_N^{(2)}(t) = 1 + \beta \left[R_N |g_D^{(1)}(t)| + (1 - R_N) \right]^2 + \{ \langle I_S^2 \rangle_N - (1+\beta) \langle I_S \rangle_N^2 \} / \langle I \rangle_N^2 \quad (10)$$

This looks a lot like the Siegert relation (Equation (6)), except for the extra term at the end. We would be tempted to identify the first term with $\beta |g^{(1)}(\tau)|^2$. We can understand the last term as a deviation from the perfect exponential statistics for which $\bar{I}_S^2 = (1+\beta) \bar{I}_S^2$. Thus as $N \rightarrow \infty$ it drops out, while $R_N \rightarrow R \equiv \bar{I}_D / \bar{I}$. Therefore we can safely identify

$$|g^{(1)}(t)| = R |g_D^{(1)}(t)| + (1 - R) \quad (11)$$

We further notice that the correction term is independent of t. To eliminate it let us define the following quantity:

$$[f(t)]^2 \equiv 1 - \{g_N^{(2)}(0) - g_N^{(2)}(t)\} / \beta \quad (12)$$

Substituting Equation (10) we obtain

$$[f(t)]^2 = 1 - \left[R_N |g_D^{(1)}(0)| + (1 - R_N) \right]^2 + \left[R_N |g_D^{(1)}(t)| + (1 - R_N) \right]^2$$

but $|g_D^{(1)}(0)| = 1$, so it follows that

$$f(t) = R_N |g_D^{(1)}(t)| + (1 - R_N) \quad (13)$$

which is an improved estimate of the normalized electric field correlation function $|g^{(1)}(\tau)|$. This method is used throughout the rest of the thesis to obtain the shape of the correlation function. One can also form another function

$$F(t) = \langle I \rangle_N f(t) \quad (14)$$

which has a very nice form

$$F(t) = \bar{I}_D |g_D^{(1)}(t)| + \langle I_S \rangle_N \quad (15)$$

so the dynamic and static intensities can be read off directly. Alternately, if one is not interested in the shape of the correlation function, but only in the intensities, one can form

$$f_\infty^2 \equiv 1 - \{g_N^{(2)}(0) - g_N^{(2)}(\infty)\} / \beta = (1 - R_N)^2 \quad (16)$$

(since $|g_D^{(1)}(\infty)| = 0$). From this follows that

$$\begin{aligned} \langle I_S \rangle_N &= \langle I \rangle_N f_\infty \\ \bar{I}_D &= \langle I \rangle_N (1 - f_\infty) \end{aligned} \quad (17)$$

This is also used frequently throughout the rest of the thesis.

The important conclusion is that, within the validity of our assumptions, we recover \bar{I}_D exactly, while $\langle I_S \rangle_N$ is subject to the $N^{-1/2}$ statistics discussed above (but no worse). In fact, we could measure $\langle I \rangle_{N'}$ independently for larger number of points N' and thus reduce the deviation. Note, however, that in such case \bar{I}_D still has to be obtained from $\langle I \rangle_N$ and not from $\langle I \rangle_{N'}$. The static part can be obtained from $\langle I \rangle_{N'} - \bar{I}_D$.

2.3 THEORY OF LIGHT SCATTERING IN GELS

The previous section has focused on the general phenomenon of light scattering from non-ergodic media. Now we shall discuss the mechanism that gives rise to dynamic and static components of light scattered intensity from gels. First the origin of the static component is explained using the theory of Pusey and van Megen (1). The second part presents the collective diffusion model of Tanaka, Hocker and Benedek (2), which has been successfully applied to explain light scattering from gels, but without taking the nonergodicity into account. The objective of this section is to combine these two approaches and derive a simple model of the dynamic structure factor $|g^{(1)}(\tau)|$.

2.3.1 Origin of the Static Component

For the purpose of this section consider gel to be a collection of discrete particles labeled by j , whose positions in space at time t are $\mathbf{r}_j(t)$. A laser beam is scattered within the scattering volume p , with a scattering vector \mathbf{q} , and is incident upon a point detector at a large distance (large with respect to the scattering volume size, the wavelength of light, etc.). The electric field at the detector can be described by

$$E_p(\mathbf{q}, t) = \sum_{j=1}^N b_j \exp[i\mathbf{q} \cdot \mathbf{r}_j(t)]$$

where the time independent field amplitudes b_j are in general \mathbf{q} dependent, and the sum is taken over all the particles within the scattering volume p . Consider the motion of j^{th} scatterer. It can be expressed as a motion relative to its average position

$$\mathbf{r}_j(t) = \mathbf{R}_j + \mathbf{u}_j(t)$$

where

$$\mathbf{R}_j \equiv \langle \mathbf{r}_j(t) \rangle_T$$

$$\langle \mathbf{u}_j(t) \rangle_T = 0$$

Now introduce an auxiliary variable

$$w_j \equiv \langle \exp[i\mathbf{q} \cdot \mathbf{u}_j(t)] \rangle_T$$

We can proceed to divide the electric field into two parts:

$$E_p(\mathbf{q}, t) = E_{D,p}(\mathbf{q}, t) + E_{S,p}(\mathbf{q})$$

where the dynamic part is written as:

$$E_{D,p}(\mathbf{q}, t) = \sum_{j=1}^N b_j \exp[i\mathbf{q} \cdot \mathbf{R}_j] \{ \exp[i\mathbf{q} \cdot \mathbf{u}_j(t)] - w_j \} \quad (18)$$

and the static part is:

$$E_{S,p}(\mathbf{q}) = \sum_{j=1}^N b_j w_j \exp[i\mathbf{q} \cdot \mathbf{R}_j] \quad (19)$$

Given that the assumptions stated in Section 2.2.1.1 (regarding the scattering conditions) are satisfied, we can go on to make some statements about $E_{D,p}(\mathbf{q}, t)$. By construction the factor $\{ \exp[i\mathbf{q} \cdot \mathbf{u}_j(t)] - w_j \}$ is a zero-mean complex variable. Provided that the medium is amorphous (as already assumed), $E_{D,p}(\mathbf{q}, t)$ is a sum of many random phase fields and fluctuating amplitudes (but the fluctuations can be small). Particle motions are not correlated on the scale of the scattering volume size (again, by assumption), therefore the summation in Equation (18) contains many independent terms fluctuating about zero means. Hence, by the Central Limit Theorem, the sum, i.e., $E_{D,p}(\mathbf{q}, t)$ is a zero-mean complex Gaussian variable.

The nature of the fluctuations should not change from place to place, so the behavior of $E_{D,p}(\mathbf{q}, t)$ will not depend on the choice of scattering volume p (the instantaneous value will be different from place to place, but we are not interested in this distinction, as we cannot measure the electric field from more than one scattering volume at one time). Therefore we can drop the p dependence and call it $E_D(\mathbf{q}, t)$. Its particular form will depend on the process governing the motion of the scatterers.

Now let's consider the static part, $E_{S,p}(\mathbf{q})$. It is time independent, by construction. Its value depends on the particular configuration of the scatterers. The phases of the factors $\exp[i\mathbf{q} \cdot \mathbf{R}_j]$ can be large compared to 2π (since the scattering volume is, by assumption, much larger than $2\pi/|q|$), so they can be viewed as random variables with zero mean. Their sum is thus a zero-mean complex Gaussian variable, when considered over the whole ensemble (it has a well-defined value for each scattering volume p). Thus

the statistics of $E_{S,p}(\mathbf{q})$ is the same as in Section 2.2.2.2. From the physical point of view the static field arises from the localization of the scatterers. In the case of a gel, this is due to the presence of the crosslinks, which restrict the spatial conformations of the polymer chains. Notice that the pre-factors in the summation in Equation (19) depend on w_j 's. If the motion of j^{th} scatterer about the average position is large (little restriction) then the fluctuation of $\mathbf{q} \cdot \mathbf{u}_j$ can be on the order of 2π , in which case w_j becomes 0. Therefore the static part disappears when the scatterers are free to move.

2.3.2 Collective Diffusion and the Origin of the Dynamic Component

In the above consideration no further insight about the form of $E_D(\mathbf{q}, t)$ could be gained. We need a description of the motion of the scatterers about their average positions. A simple theory that nevertheless describes quite well the light scattering from gels was developed by Tanaka et al (2). It is very accessibly summarized in (10), from which the following discussion was taken. The basic simplifying assumption of this theory is that from the point of view of light scattering the gel can be approximated by a continuous medium. The rationale for that simplification is that the characteristic dimensions associated with the gel (e.g., the average distance between crosslinks) are much smaller than the wavelength of light. In this approximation the light is scattered from the thermal fluctuations of this continuous medium which are overdamped phonons.

The dynamics of a continuous medium can be described using a displacement vector $\mathbf{u}(\mathbf{r}, t)$ which represents the displacement of the volume element at point \mathbf{r} at time t from its equilibrium position. The Newton's second law for this system can be written:

$$\rho(\partial^2 \mathbf{u} / \partial t^2) = \nabla \cdot \tilde{\sigma} - f(\partial \mathbf{u} / \partial t)$$

where ρ is the density, f the friction constant (between the network and the liquid) and $\tilde{\sigma}$ the stress tensor. The right hand side represents the forces acting on our volume element: the restoring force of the internal stress and the friction force due to relative displacement of the network with respect to the liquid (which is proportional to the velocity). The left hand side represents the inertia (mass times acceleration). It generally is much smaller than the other terms, so it will be dropped from here on. To proceed further we express the stress tensor explicitly:

$$\sigma_{ik} = K \nabla \cdot \mathbf{u} \delta_{ik} + 2\mu(u_{ik} - \frac{1}{3} \nabla \cdot \mathbf{u} \delta_{ik})$$

with

$$u_{ik} \equiv \frac{1}{2}[\partial u_k / \partial x_i + \partial u_i / \partial x_k]$$

where K and μ are the bulk and shear moduli of the gel network. Dropping the inertia term and computing the divergence of the stress tensor we obtain the equation

$$f \frac{\partial \mathbf{u}}{\partial t} = \left(K + \frac{\mu}{3} \right) \nabla(\nabla \cdot \mathbf{u}) + \mu \nabla^2 \mathbf{u}$$

which can be decomposed into three diffusion equations – one longitudinal and two transverse:

$$\frac{\partial u_l}{\partial t} = \frac{K + \frac{4}{3}\mu}{f} \frac{\partial^2 u_l}{\partial t^2} \quad (\text{longitudinal})$$

$$\frac{\partial u_t}{\partial t} = \frac{\mu}{f} \frac{\partial^2 u_t}{\partial t^2} \quad (\text{two transverse})$$

The solutions are three diffusive modes (overdamped phonons) with diffusion constants

$$D = \begin{cases} \left(K + \frac{4}{3}\mu \right) / f & (\text{longitudinal}) \\ \mu / f & (\text{transverse}) \end{cases}$$

These modes scatter light passing through the gel. The longitudinal mode gives rise to polarized, and the transverse modes to depolarized light scattering. The depolarized scattering is much harder to detect, and will not be considered here. The polarized scattering from the longitudinal diffusive mode can be written (2) as:

$$\langle E_{\text{pol}}(\mathbf{q}, t) E_{\text{pol}}(\mathbf{q}, 0) \rangle \propto \left(\frac{\partial \epsilon}{\partial \rho} \right)_T^2 \rho^2 \frac{k_B T}{K + \frac{4}{3}\mu} \exp \left[- \frac{\left(K + \frac{4}{3}\mu \right) q^2 t}{f} \right] \quad (20)$$

where ϵ stands for the diagonal elements of the dielectric tensor ($\epsilon = n^2$) and ρ is the density. The proportionality factor depends only on the scattering geometry.

From the point of view of our discussion this is the most important result of the collective diffusion theory.

2.3.3 Summary

The nonergodic theory predicts the existence of two components in the scattered electric field – a dynamic component which is a zero-mean complex Gaussian variable in time, and which is position (scattering volume) independent, and a static component, which is a zero-mean complex Gaussian variable when taken over the whole ensemble, but is time independent. The dynamic component arises from the fluctuations of the scatterers about their average positions, while the static component is due to the restriction of the motion of scatterers. The time correlation of the fluctuating part cannot be predicted from these considerations.

The collective diffusion theory predicts a specific behavior of the scatterers by modeling their motion with an elastic motion of a continuous medium. It does not take into account the static component due to scattering from the average positions.

It does not seem contradictory to augment the collective diffusion model by incorporating the static part predicted by the nonergodic theory. The motion of the scatterers can still be described by the elastic continuum approach, but bearing in mind that the physical reality requires that the average positions of the particles be considered as scatterers too. The experiments reported in further chapters of this thesis support this conclusion, at least for simple systems, since in these cases the electric field correlation function can be decomposed into a static offset, and a single-exponentially decaying part – a signature of the collective diffusion.

2.4 SOME EXPERIMENTAL RESULTS

A number of the concepts introduced and discussed above can be effectively illustrated with some simple experimental results. This section describes a number of these and explains their relevance to the discussion above.

2.4.1 Correlation Function Statistics

Section 2.2.1 discussed the statistics of the raw correlation data. The number of counts in the correlator channel i (denoted $C[i]$), is proportional to $I^2 \cdot T$, where I is the total intensity and T the collection time. The relative deviation (σ) was said to be

$$\frac{\sigma(C[i])}{\bar{C}[i]} \cong \frac{1}{\sqrt{\bar{C}[i]}}$$

Figure 3 plots the relative deviation σ (obtained using $\sigma^2 = \chi^2/M$ from a good quality least-squares fit to M channels) versus $C^{-1/2}$. It is evident from the graph that there is a one-to-one correspondence between the two.

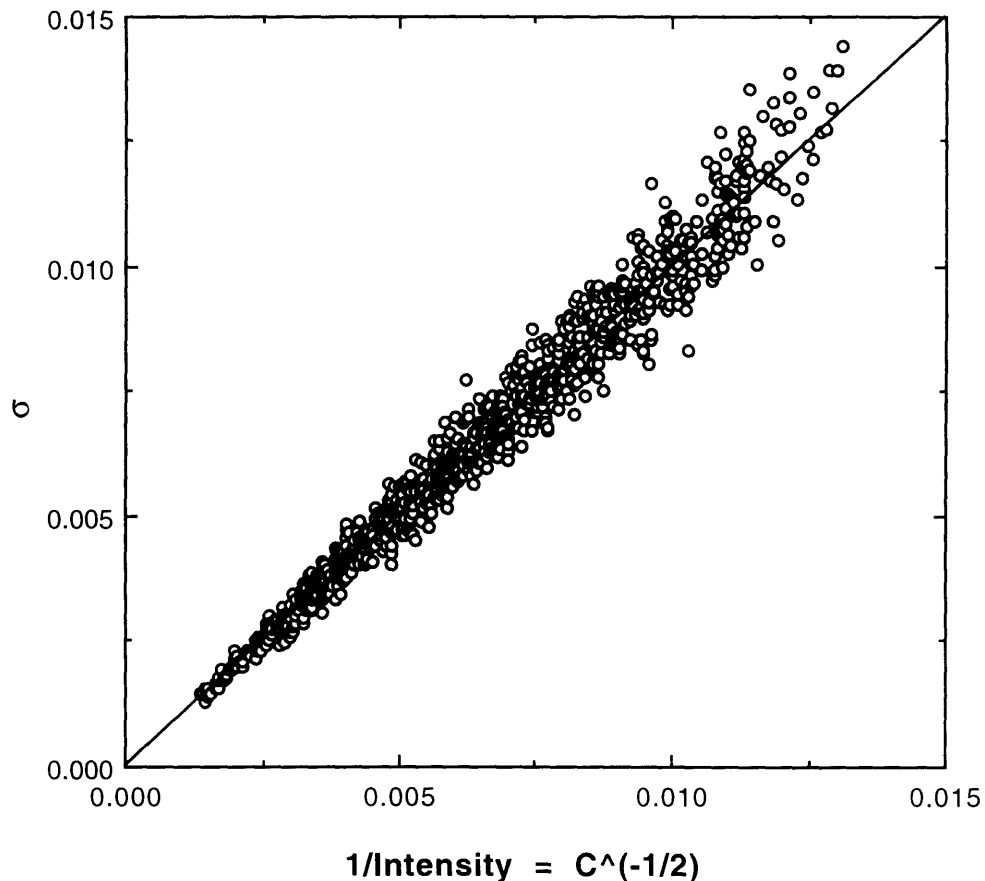


Fig. 3 Plot of average deviation of the normalized correlation function (obtained by dividing the χ^2 from a good quality double-exponential fit by the number of fitted channels) versus $1/\text{Intensity}$ (which equals the inverse of the square root of the number of counts per correlator channel C). The one-to-one correspondence is evident.

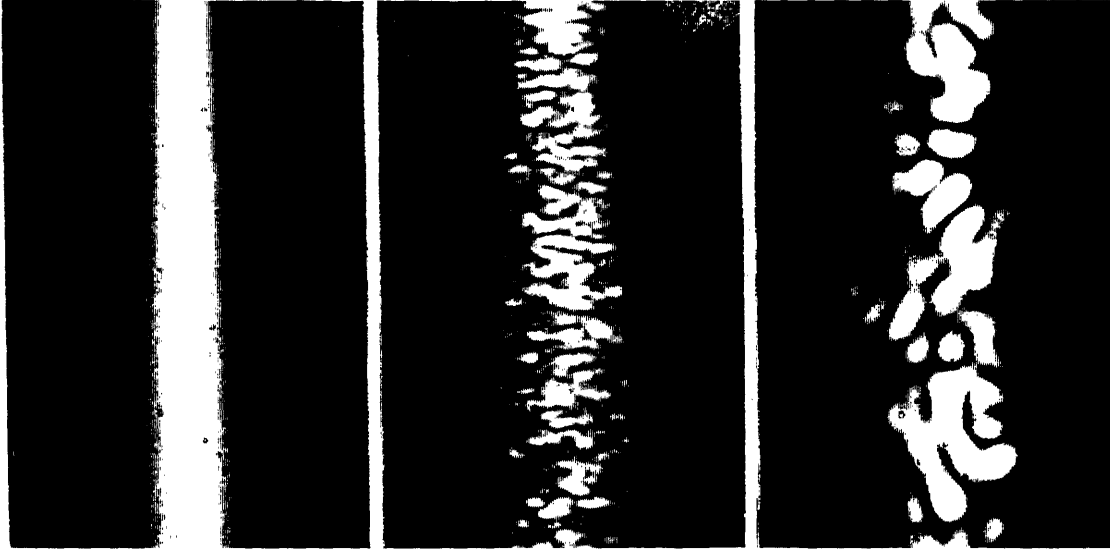


Fig. 4 Microscope photographs (320x magnification) of laser light passing through an ergodic medium (54nm polystyrene latex spheres – left figure) and through a non-ergodic medium (an AMPS-MAPTAC gel – center and right figures). Note the presence of bright and dark areas (the speckle pattern) in the latter cases. The center photograph was taken with the aperture open, while in the right one it was at its minimum. This proves that the speckles are due to an interference of scattered light (and not to some intrinsic length scale within the gel).

2.4.2 Speckle Pattern

One of the manifestations of gel's nonergodicity is the speckle pattern produced by a laser beam passing through the gel. Figure 4 compares the microscopic image of light passing through a liquid (ergodic medium – left panel) and a gel (nonergodic medium – center and right panels). What is evident in the gel sample is the presence of bright and dark areas (the speckle pattern). When the gel is rigid enough (and practically all the gels considered in this thesis were), the arrangement of the pattern does not change in time. The exact size of the speckles depends on the numerical aperture of the objective lens. The higher the aperture the finer the pattern. The middle photograph of Figure 4 shows the speckle pattern for a large aperture, while the right photograph was taken with small aperture. This follows from the fact that the higher aperture mixes light from a

larger solid angle. It also demonstrates directly that the speckle pattern is an interference phenomenon and does not correspond to some "macroscopic" structure (observable through a microscope). Another evidence for this is that when the sample is moved the speckle pattern changes much more rapidly than its apparent size would warrant, so a speckle is not "fixed" to some particular position.

2.4.3 Reproducibility

As mentioned above, the speckle pattern can persist over extended periods of time. Figure 5 shows the result of measuring the intensity at different positions within the gel – "scanning" the gel. Two traces are superimposed on top of each other showing an excellent reproducibility.

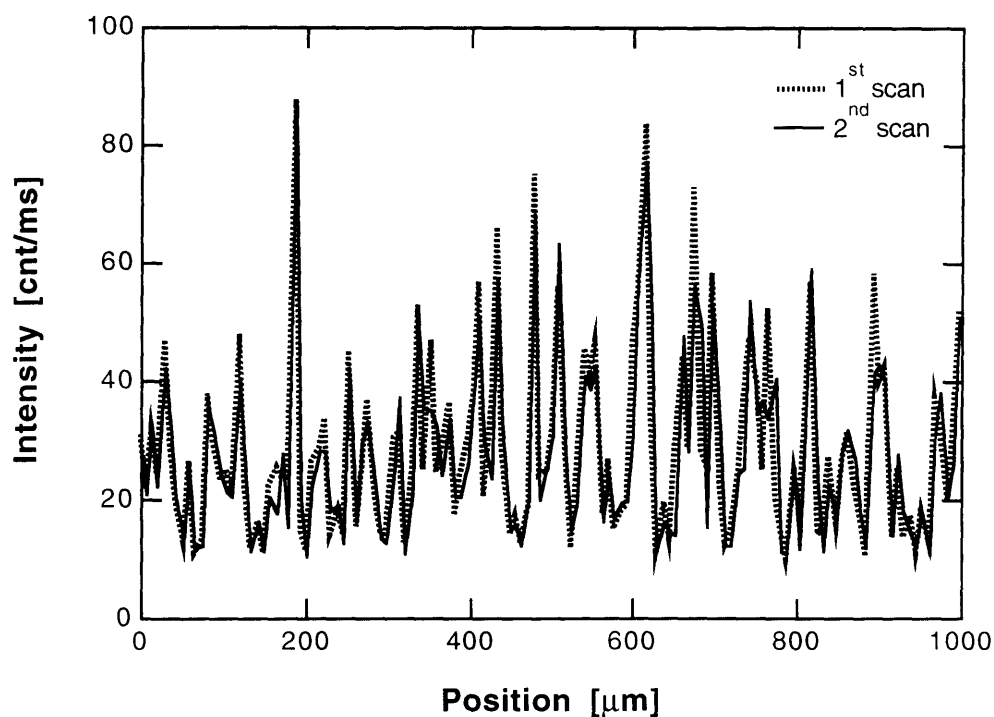


Fig. 5 Two scans over the same positions show excellent reproducibility of the speckle pattern. Two other features are also evident. First is the randomness of the pattern. The second is that the intensity does not drop below a certain value (dynamic portion).

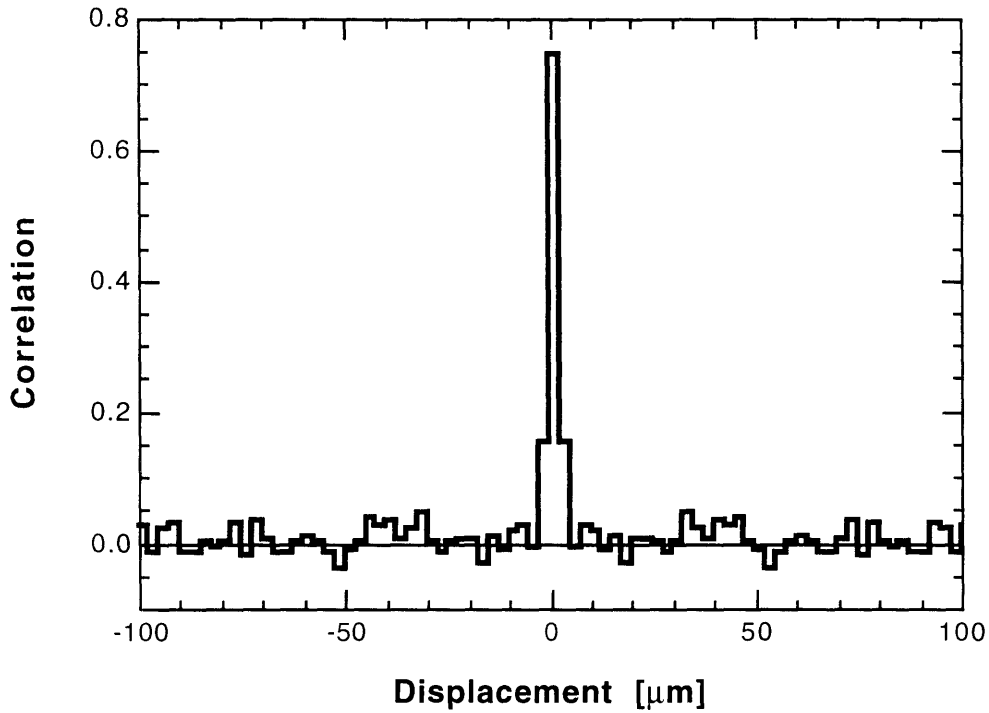


Fig. 6 Autocorrelation of the speckle pattern. In an exact analogy to the time autocorrelation function the position autocorrelation function is computed from intensity data collected at 1000 points spaced $2.5\mu\text{m}$ apart. The figure shows that the intensities are not correlated beyond one step of $2.5\mu\text{m}$. The peak at 0 displacement corresponds to $\langle I^2 \rangle / \langle I \rangle^2$.

2.4.4 Randomness

Figure 6 shows the position autocorrelation of the total intensity. It is calculated and normalized in an exact analogy to the time autocorrelation functions discussed earlier:

$$G_q = G_{-q} = \frac{N \cdot \sum_{p=1}^N I_p \cdot I_{p+|q|}}{\left(\sum_{p=1}^N I_p \right) \cdot \left(\sum_{p=1}^N I_{p+|q|} \right)} - 1$$

It is evident from Figure 6 that the intensities are not correlated over distances larger than one step size ($2.5\mu\text{m}$). This length scale roughly corresponds to the size of the scattering volume, so it shows that non-overlapping scattering volumes are independent of each other. N.B. the speckle size in the right of Figure 4 is about $15\mu\text{m}$,

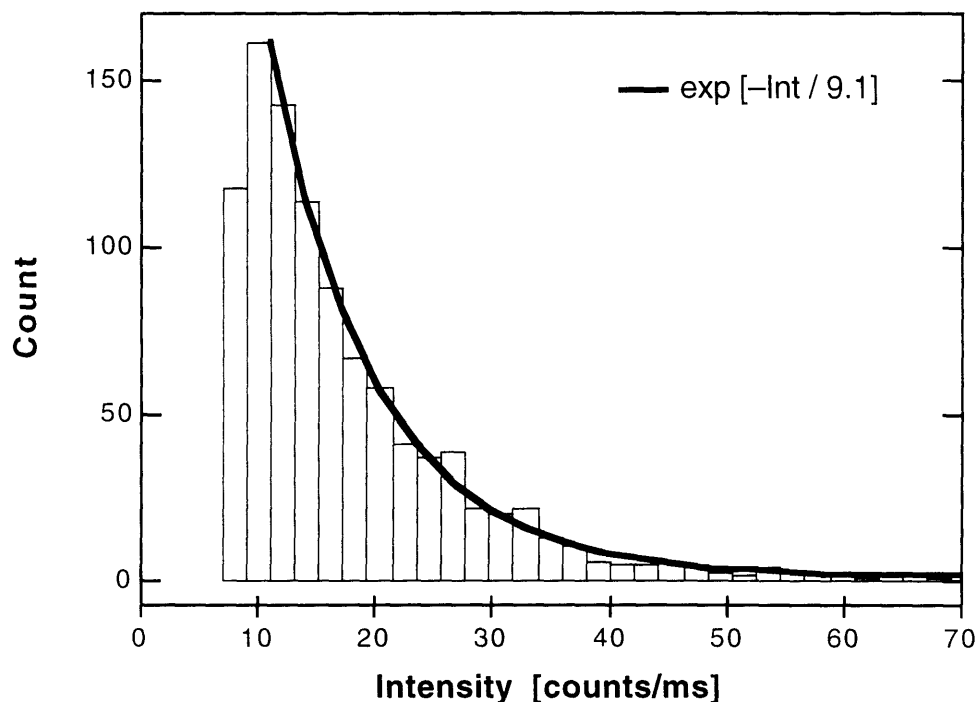


Fig. 7 The histogram of the scattering intensities taken at 1000 different positions within one gel sample. The dynamic intensity is represented by the offset from the vertical axis (total intensity never falls below that value – thus the zero count). The static intensity is exponentially distributed. A fit to an exponential is plotted (heavy line). The deviation from exponential around the dynamic cutoff is due to the finite size of the detector.

2.4.5 Intensity Histogram

The results of Section 2.2.2.2 (Equation (5)) predict that the intensity probability distribution over different positions should be exponentially decaying. The position independent dynamic component introduces an offset in this distribution – at no point should the total intensity I be less than I_D . It is interesting to observe how this works in

practice. Figure 7 shows a histogram of intensities. One notices immediately both the horizontal offset I_D , and the exponentially decaying distribution of I_S . What differs from the prediction is a rounded-off transition around I_D (as opposed to a sharp cutoff one would expect). This is explained by the finite size of the detector. Reference (4) gives a formula for the probability distribution taking into account the number n of coherence areas focused on the detector:

$$P_n(\Delta I) = \frac{\left(\frac{n}{\langle \Delta I \rangle}\right)^n \Delta I^{(n-1)} e^{-n\Delta I/\langle \Delta I \rangle}}{\Gamma(n)} \quad (21)$$

where $\Delta I = I - I_D$. N.B. for the ideal case of $n=1$ this distribution reduces to

$$P_{n=1}(\Delta I) = \left(\frac{1}{\langle \Delta I \rangle}\right) e^{-\Delta I/\langle \Delta I \rangle}$$

which is the result of Section 2.2.2.2. For $n>1$ P_n has a smooth transition to 0, as observed in Figure 7.

2.4.6 Local Oscillator Effects (Heterodyning)

In the case of a simple system (where by simple I mean a system with a single exponential correlation function) it is easy to illustrate the effects of heterodyne mixing of the dynamic part with the static component (which acts as a local oscillator coherent with the dynamic part) in a time averaged correlation function. Let us investigate its effects on the apparent diffusion constant (the diffusion constant obtained if nonergodic effects are ignored). Here we have, using the notation introduced in the previous section

$$|g_D^{(1)}(t)| = e^{-t/\tau} \quad (22)$$

An argument similar to that in Section 2.2.2.3 gives the form of the normalized time averaged correlation function:

$$\begin{aligned} g_{T,p}^{(2)}(t) - 1 &= R_p^2 |g_D^{(1)}(t)|^2 + 2R_p(1 - R_p) |g_D^{(1)}(t)| \\ &= R_p^2 e^{-2t/\tau} + 2R_p(1 - R_p) e^{-t/\tau} \end{aligned} \quad (23)$$

where $R_p = I_D/I_p$. The first term represents the homodyne (self-beating) of the dynamic component, and the second – heterodyning with the static component (entering here as $1 - R_p$). The functional form of $g_{T,p}^{(2)}(t)$ is very close to that of a single exponential. This is because it is hard to distinguish between two exponentials with narrowly spaced decay times. One would be tempted to fit it with a homodyne correlation function (a single exponential), and would obtain a good fit with a decay time τ^* somewhere between τ and 2τ , depending on the value of R_p . The functional form is so simple that one can play this game analytically. Define

$$\chi^2 = \int_0^{\infty} \left(g_{T,p}^{(2)}(t) - A e^{-2t/\tau^*} \right)^2 dt$$

and then minimize χ^2 with respect to τ^* and A . One then obtains a relationship between $\gamma \equiv \tau^*/\tau$ and R_p

$$R_p = \frac{2(1 - 2\gamma)(1 + \gamma)^2}{1 - 3\gamma - 6\gamma^2} \quad (24)$$

If I_D is indeed constant from position to position, then R_p depends only on the total intensity, and the equation above can be used to obtain a function relating γ to I . Figure 8 shows the values of τ^* , obtained by fitting a single exponential to data obtained at different positions of one gel sample, plotted against the total intensity at each point. Two features of this graph are immediately apparent. First, the intensity never goes below a certain value (which we can assume to be the dynamic intensity I_D). Second, the value of τ^* at high intensities is twice that obtained at low intensity, consistent with the view that when the static intensity is low, the homodyne term is significant, while at high intensity the heterodyne term dominates. Also plotted is a fit of $\tau \cdot \gamma(I)$ to this data using only two parameters: τ and I_D . The quality of this fit is quite good, which lends credibility to the explanation outlined above.

2.4.7 Extracting Decay Time from Ensemble Average

The procedure outlined in the previous section can be used to extract the decay time (and thus the diffusion constant) also from an ensemble averaged correlation function. All we need to know is $R = I_D/I$. For a system with a single-exponential correlation function we have, using Equations (6), (11), and (22):

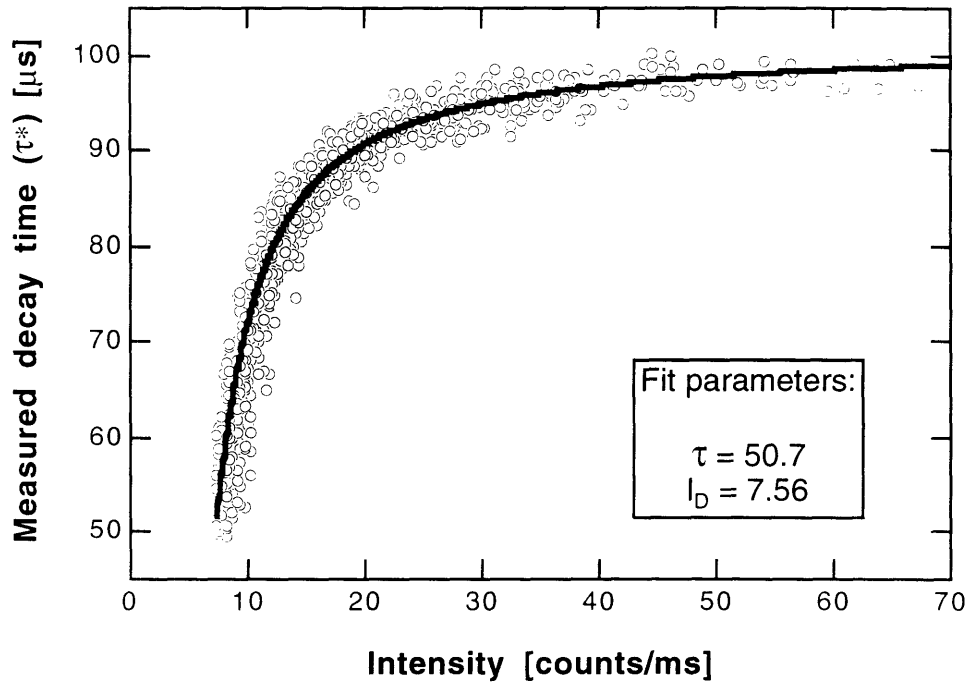


Fig. 8 Plot of the measured decay time τ^* (obtained from a single-exponential fit) versus the intensity. Data comes from 1000 locations within one gel sample. τ^* is obtained by fitting a single-exponential to the time-averaged correlation function at each point. The solid line is a two parameter fit using the function described in the text. At low intensities the correlation function behaves like a homodyne, at high intensities like a heterodyne.

$$\begin{aligned}
 g_E^{(2)}(t) - 1 &= |g^{(1)}(t)|^2 = \left(R |g_D^{(1)}(t)| + (1-R) \right)^2 \\
 &= R^2 e^{-2t/\tau} + 2R(1-R)e^{-t/\tau} + (1-R)^2
 \end{aligned}$$

which has the same functional form (except for a constant) as $g_{T,p}^{(2)}(t)$ in the previous section. Thus the same procedure of fitting $g_N^{(2)}(t)$ with a single exponential would apply (since $g_N^{(2)}(t) = g_E^{(2)}(t) + \text{const}$, by Equation (10)). So the recipe is as follows:

1. Use Equations (16)-(17) to obtain R . One can get $\{g_N^{(2)}(0) - g_N^{(2)}(\infty)\} / \beta$ directly from the amplitude of a fit to $g_N^{(2)}(t)$ with a floating baseline (an additive constant).

2. Use the value of R and the fit parameter τ^* to obtain $\tau = \tau^*/\gamma(R)$, where $\gamma(R)$ is defined by Equation (24).

Why not fit with the expected functional form of $g_E^{(2)}(t)$ directly? The problem is the reliability of the fitting procedure. A single exponential fit is very robust, a sum of two exponentials with close decay times is not. A numerical experiment of fitting both a single exponential and a sum of two exponentials to simulated noisy data of the form of $g_E^{(2)}(t)$ shows that the procedure outlined above is able to recover τ much more reliably.

CONCLUSION

From the practical point the procedures for processing raw correlation data introduced in this section are significant. The most important ones are Equations (12)-(14) for recovering the shape of the dynamic structure factor $f(t)$, Equations (16)-(17) for obtaining dynamic and static contributions to the average intensity, and the procedure of Section 2.4.7 for calculating the corrected decay time from single exponential fit parameters.

From the theoretical point of view an important result is the conclusion in Section 2.3 that the collective diffusion theory is not incompatible with the nonergodic theory, and that taken together they can predict the shape of the correlation function.

REFERENCES

- [1] Pusey, P. N. and van Megen, W.: *Physica A*. **157**, 705 (1989).
- [2] Tanaka, T., Hocker, L.O. and Benedek, G.B.: *J. Chem. Phys.*, **59**, 5151 (1973).
- [3] Reif, F.: *Fundamentals of Statistical and Thermal Physics*, McGraw-Hill, New York, (1963).
- [4] Goodman, J.W. in: *Laser Speckle and Related Phenomena*, ed. Dainty, J.C., Springer-Verlag, Berlin (1964).
- [5] Joosten, J.G., McCarthy, J.L., Pusey, P.N.: *Macromolecules*, **24**, 6690 (1991).
- [6] Fang, L. and Brown, W.: *Macromolecules*, **25**, 6897 (1992).
- [7] Joosten, J.G.H.: *Progr. Colloid Polym. Sci.*, **91**, 149 (1993).
- [8] Skouri, R., Munch, J.P., Schosseler, F. and Candau, S.J.: *Europhys. Lett.*, **23**, 635 (1993).
- [9] Pusey, P.N. in: *Photon Correlation Spectroscopy and Velocimetry*, Cummins, H.Z. and Pike, E.R., eds. Plenum, New York, p. 45ff (1977).
- [10] Tanaka, T., "Light Scattering from Polymer Gels" in *Dynamic Light Scattering*, ed. R. Pecora. Plenum, New York (1985)

CHAPTER 3

FROZEN GEL INHOMOGENEITIES - TEMPERATURE OF GELATION DEPENDENCE

The last chapter introduced the notion of nonergodicity in gels. This chapter investigates some of the mechanisms that contribute to this phenomenon. Structure of a cross-linked polymer network depends not only on its chemical constituents, but also on the conditions under which the gel is polymerized. Highly non-uniform spatial distributions of polymer network concentration and cross-linking density are observed in most polymer gels. The inhomogeneities, as studied using light scattering, are shown to result from two origins: one from the dynamic critical fluctuations of polymer solution at the onset of gelation, and the other from the domain formation due to the micro-phase separation. Both are directly related to the phase equilibrium properties of the gel during the gelation process. Those fluctuations of polymer density are frozen in the gel structure permanently. In addition to these permanent spatial fluctuations, a polymer network undergoes thermal dynamic concentration fluctuations which diverge at the critical point. These three types of fluctuations, two static, and one dynamic, account for the nature of gel inhomogeneities. The static spatial fluctuations reversibly increase and diverge at the spinodal line, although they are permanent inhomogeneities. A qualitative interpretation is given to account for this phenomenon.

3.1 INTRODUCTION

The formation of heterogeneous structures of cross-linked polymer gels has been the subject of great interest for many years, since the physical properties of gels are directly affected by the degree of heterogeneities in gels. The structural inhomogeneities of a gel affects greatly its physical properties such as permeability, elasticity, optical and phase properties. Extensive studies have been made on the characterization of the gel inhomogeneities. Weiss and Silberberg showed that high permeability of acrylamide gels is related to the inhomogeneous cross-link distribution (1,2). Hsu and colleagues examined the effects of inhomogeneities of polymer network on the swelling equilibrium of acrylamide gels and on the diffusion of water molecules within the gels (3). The ring structures and intramolecular chemical reactions during gelation were studied by Standford and Stepto (4). They found that the shear moduli of the polyester and polyurethane gels were reduced markedly in the presence of such elastically ineffective polymer network loops. Funke reviewed several different polymer networks with non-uniform distribution of cross-links (5). The groups of Candau and Geissler quantified the inhomogeneities using various neutron, X-ray and static light scattering techniques, and proposed models explaining the difference between gels and equivalent solutions (6, 7).

The parameters used commonly to vary the network structure and its inhomogeneities are the concentration of polymers and the proportion of cross-linkers to polymers. For polyacrylamide gels, Richards and Temple described a model which relates gel compositions with swelling ratio, turbidity elastic modulus and volume fractions (8). Bansil and Gupta determined the boundary between a clear state and an opaque, heterogeneous state for a gel as a function of monomer and cross-linker concentrations (9). Nishio and co-workers compared gels prepared at two different temperatures and qualitatively described the difference (10).

It is well known that the turbidity of a gel is a direct result of light scattered from the spatial inhomogeneities of its refractive index.

Dusek proposed a model of microsineresis, where a dispersion of separated pure liquid phase and the remaining gel structure is responsible for the scattering of light (11). This chapter presents a more general picture for the physical principle underlying the formation of spatial inhomogeneities in polymer gels. From examinations of the effects of gelation temperature on the spatial distribution of polymer network density using quasielastic and elastic light scattering techniques, we conclude that there are three types of causes for the structural inhomogeneities within a gel. First, the dynamic

concentration fluctuations of pre-gel polymer solutions are frozen in the final network structure upon gelation process. Second, if the polymer solution is in the phase separation regime, there appear two gel phases having two different concentrations. The domain sizes of these two phases depend on the condition of gelation process, and their size can sometimes be on the order of wavelength of light and scatter light tremendously giving strong opacity to the gel (11). In both cases the phase equilibrium properties of the gel play an essential role in determining the permanent structural inhomogeneities within a gel. Third, besides having these permanent structural inhomogeneities, a gel undergoes temporal thermal concentration fluctuations. These inhomogeneities give an opacity to a gel similar to the critical opalescence of binary fluids. These dynamic concentration fluctuations have been previously investigated using the technique of quasielastic light scattering (12-15).

Extensive studies of dynamic and static light scattering from gels with various chemical compositions showed the presence of inhomogeneous structures embedded within the polymer networks and their influence on dynamic properties of the gels (11). The permanent inhomogeneities contribute to the phenomenon of non-ergodicity of a gel, which attracted much attention from experimentalists and theorists (16-21).

3.2 EXPERIMENTS

3.2.1 Sample Preparation

The gels were formed by free radical copolymerization of N-isopropylacrylamide (7.8g) and N,N'-methylenebisacrylamide (0.130g) in 100ml of deionized water. Tetramethylethylenediamine (TEMED, 240 μ l) was used as accelerator. Thus prepared pre-gel solution was filtered using a 0.22 μ m filter and degassed in vacuo for 10-15 minutes. Finally 43mg of ammonium persulfate (an initiator) were added and then the solution transferred into micropipettes for gelation. The temperature of the gelation process was controlled by immersing the micropipettes into a circulating heat bath (Lauda model RM 6) for 18 hours. The gels thus prepared had the lower critical point at approximately 34°C.

The light scattering cells used in the experiments were 100 μ l glass micropipettes (1.31mm inner diameter) placed inside optical square cuvettes of 1cm inner side filled with water (for room temperature measurements), or in a sample holder with a thermoelectric device temperature control (for more details see Section 0.4)

3.2.2 Light Scattering

In order to quantify the inhomogeneities of gel network structure, we determined the scattered light intensity and the intensity auto-correlation function at an angle of 90° using a microscopic laser light scattering (MLLS) setup described in detail in the Introduction to this thesis. Some important points are summarized here. The sample cell was mounted on a microscope stage, which could be moved perpendicularly to the scattering plane. In a typical experiment the sample cell was moved every $7.5\mu\text{m}$ using a stepping motor. The scattered light intensity and the intensity auto-correlation function (collected with a Brookhaven BI-2030AT correlator with 136 linear channels) were determined simultaneously at N different positions. In the measurement temperature dependence experiments the temperature of the sample cell was controlled to within 0.01°C . The gelation temperature dependence experiments were run at room temperature.

The samples exhibited a large degree of nonergodicity, so they had to be analyzed using the method described in Chapter 2. Raw correlation functions were measured at N different locations obtained by laterally translating the sample. They were summed and normalized forming an approximation $g_N^{(2)}(t)$ to the ensemble average $g_E^{(2)}(t)$. We used $N=50$ for measurement temperature and $N=150$ for gelation temperature dependence. This allowed us to obtain the average intensity to within 14.1% and 8.2% respectively (see Chapter 2).

The diffusion coefficient D was obtained by fitting $g_N^{(2)}(t)$ with a single exponential $A e^{-D^*q^2t} + B$ and then correcting D^* for heterodyning of \bar{I}_D with $\langle I_S \rangle_N$ (see again Chapter 2).

3.3 RESULTS

3.3.1 General Observations

The positional dependence of the scattered light intensity measured at room temperature is shown in Figure 1. The scattered light intensity of the gel made at 20°C fluctuates substantially as the scattering position is scanned within the gel. It is important to observe that the fluctuation profile is reproducible when measurements are repeated

along the same path along the gel as shown in the figure (in agreement with (21)). This indicates that the light scattering is from a structure that is restricted in the gel rather than from dynamic fluctuations. If the scattering were due to the dynamic fluctuations of the polymer network, the scattering intensity would not depend on the position within the gel, because the scattering intensity is an average over a time period much longer compared to the fluctuation time. The intensity of the scattered light did not become zero even when it was at minimum value. This further confirms the validity of the analysis proposed above where the residual intensity \bar{I}_D originates from light scattered by the dynamic collective mode of the polymer network and is present at every point within the gel.

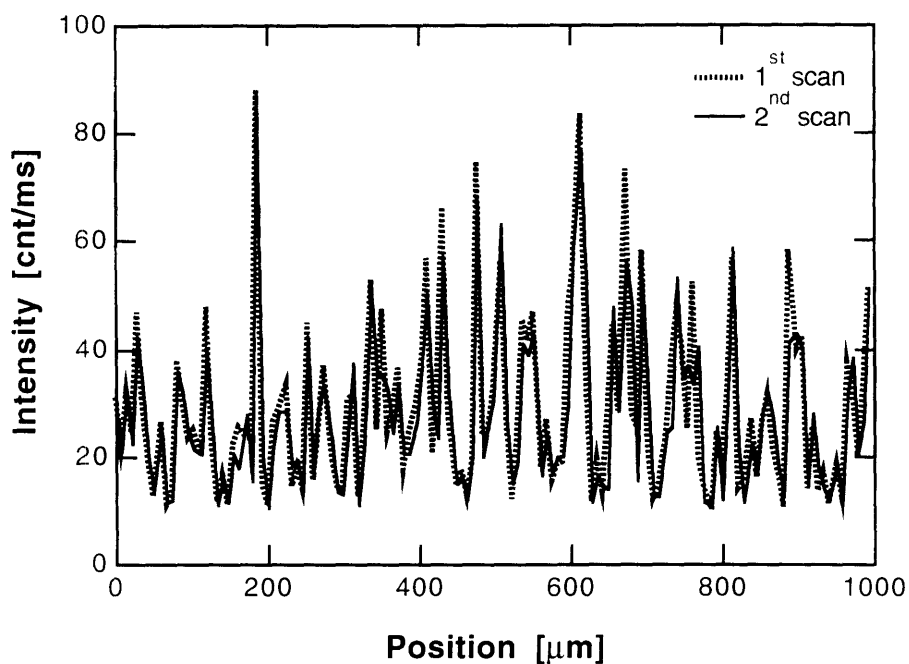


Fig. 1 Position dependence of scattered light intensity from an N-isopropylacrylamide gel, prepared at 20°C. Positions were changed in 7.5 μm steps using a motor. Two measurements were carried out along the same measurement paths to show the permanency and reproducibility of the profile of light intensity scattered from gel inhomogeneities.

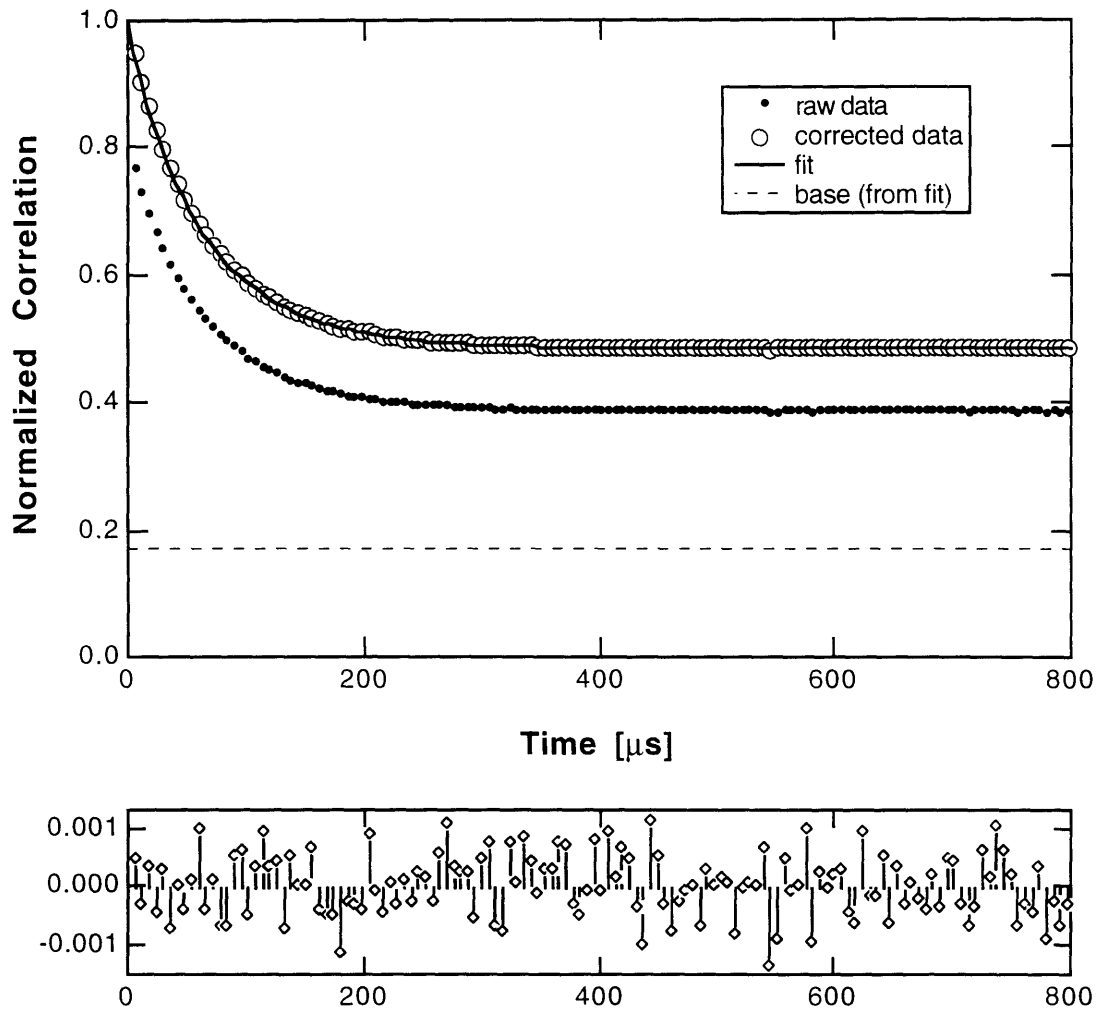


Fig. 2 Typical autocorrelation curve (dots) obtained by summing, and then normalizing the raw correlation functions obtained at each point. Also shown (open circles) is this curve corrected for finite N and for the instrumental parameter β . The solid line is a fit of $A (e^{-t/\tau} + R)^2 + B$ to this curve. The dashed line shows B for this fit. The residuals (data-fit) are plotted in the bottom graph (units are the same as in the upper graph).

Figure 2 depicts a typical $g_N^{(2)}(t)$ curve obtained by summing, and then normalizing the raw correlation functions obtained at each point. Also shown is a curve corrected for finite N and for the instrumental parameter β according to

$$G^2(t) \equiv 1 - \{g_N^{(2)}(0) - g_N^{(2)}(t)\} / \beta$$

As described above, the values of $\langle I_S \rangle_N / \langle I \rangle_N$ and $\bar{I}_D / \langle I \rangle_N$ can be easily read off from $G^2(\infty)$. A fit of the function $A (e^{-t/\tau} + R)^2 + B$ to the corrected curve is also shown. Two points should be mentioned. As seen from the residuals, the quality of the fit is indeed excellent. However, the analysis presented above assumes $B=0$, whereas a positive value is obtained from the fit (indicated as the dashed line on the graph). This is most easily explained by the presence of light which is incoherent with the dynamic part (it does not take part in the heterodyning), but contributes to the total intensity. In such case our analysis lumps it with the \bar{I}_S introducing only a small error to the overall result.

3.3.2 Dependence on Gelation Temperature

The scattered light intensity fluctuations are strongly dependent on the temperature at which the gels were made. As shown in Figures 3-a, 3-b, and 3-c, the amplitude of the fluctuations increased substantially as the gelation temperature was increased. The results are summarized in Figure 4. Both \bar{I}_S and \bar{I}_D are plotted as a function of the temperature at which gelation takes place. All measurements were carried out at room temperature. For the gels made at low temperatures the average intensities, \bar{I}_S and \bar{I}_D , were low. However, \bar{I}_S increased as the gelation temperature increased, and seemed to jump quite drastically around 28°C. The gels made above this temperature showed a permanent translucence turning to opacity at even higher temperatures. It should be noted that the polymerization of N-isopropylacrylamide is an exothermic reaction, so the actual gelation temperature might have been slightly higher than the temperature of the heat bath that is reported here. \bar{I}_D remained almost constant, decreasing only at high temperatures. The diffusion coefficient D plotted in Figure 6-a is practically independent of the gelation temperature, even at the high end.

3.3.3 Dependence on Measurement Temperature

The position dependence of scattered light intensity of an N-isopropylacrylamide gel made at 20°C was determined as a function of measurement temperature. The results are shown in the right half of the Figure 3 (d, e, and f), and summarized in Figure 5. Both \bar{I}_S and \bar{I}_D are plotted as a function of the temperature at which gelation takes place. In the figure the inverses of these intensities are also plotted. As the temperature approached

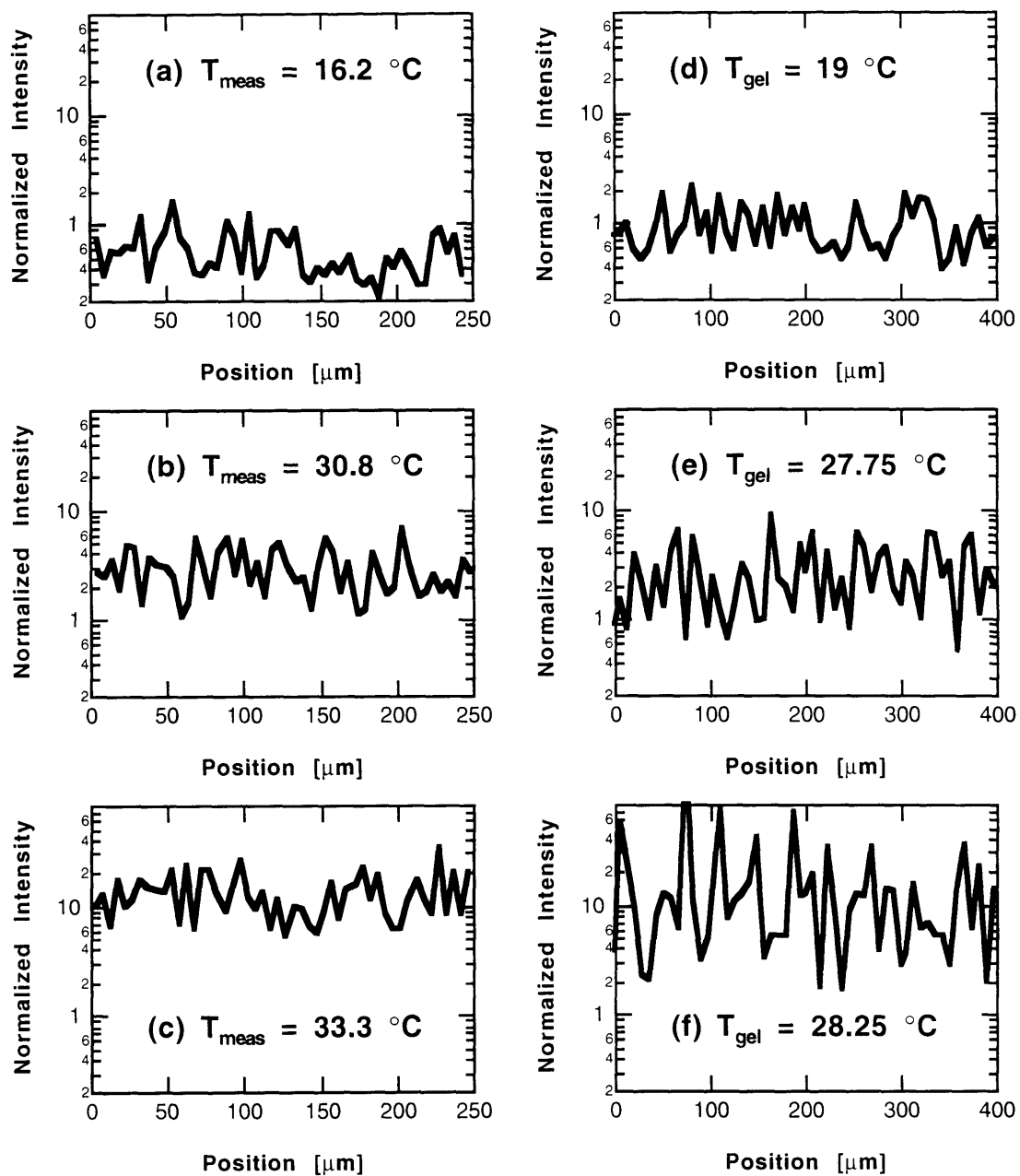


Fig. 3 The position dependence of light intensity scattered from an N-isopropylacrylamide gel is shown as a function of gelation temperature (a, b, and c). The measurement temperature was 23°C . On the right side of the Figure (d, e, and f), the position dependence of scattered light intensities is shown for different measurement temperatures (gelation temperature = 20°C).

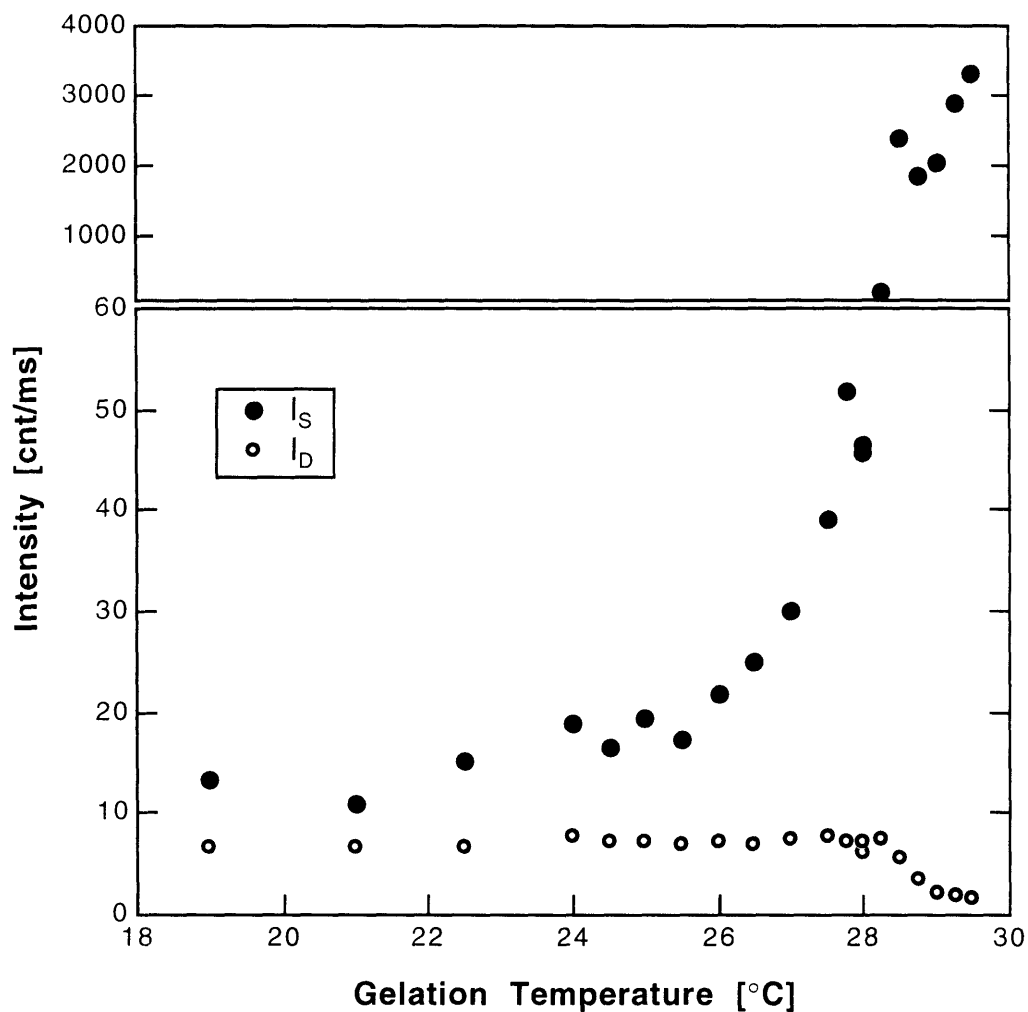


Fig. 4 The amplitudes of the spatial (\bar{I}_S) and dynamic (\bar{I}_D) fluctuations of scattering intensity are plotted as a function of the temperature at which the gel is prepared. The measurements were carried out at 23°C. \bar{I}_S appears to jump at 28°C. \bar{I}_D remains almost constant.

the critical temperature of 33.4°C, the static (\bar{I}_S) and dynamic (\bar{I}_D) amplitudes increased and appeared to diverge. The divergence of the dynamic amplitude can be understood as the critical divergence of the density fluctuations of the polymer network. This was confirmed by observing the collective diffusion coefficient of the gel, which showed critical slowing-down at the same temperature (Figure 6-b) (13).

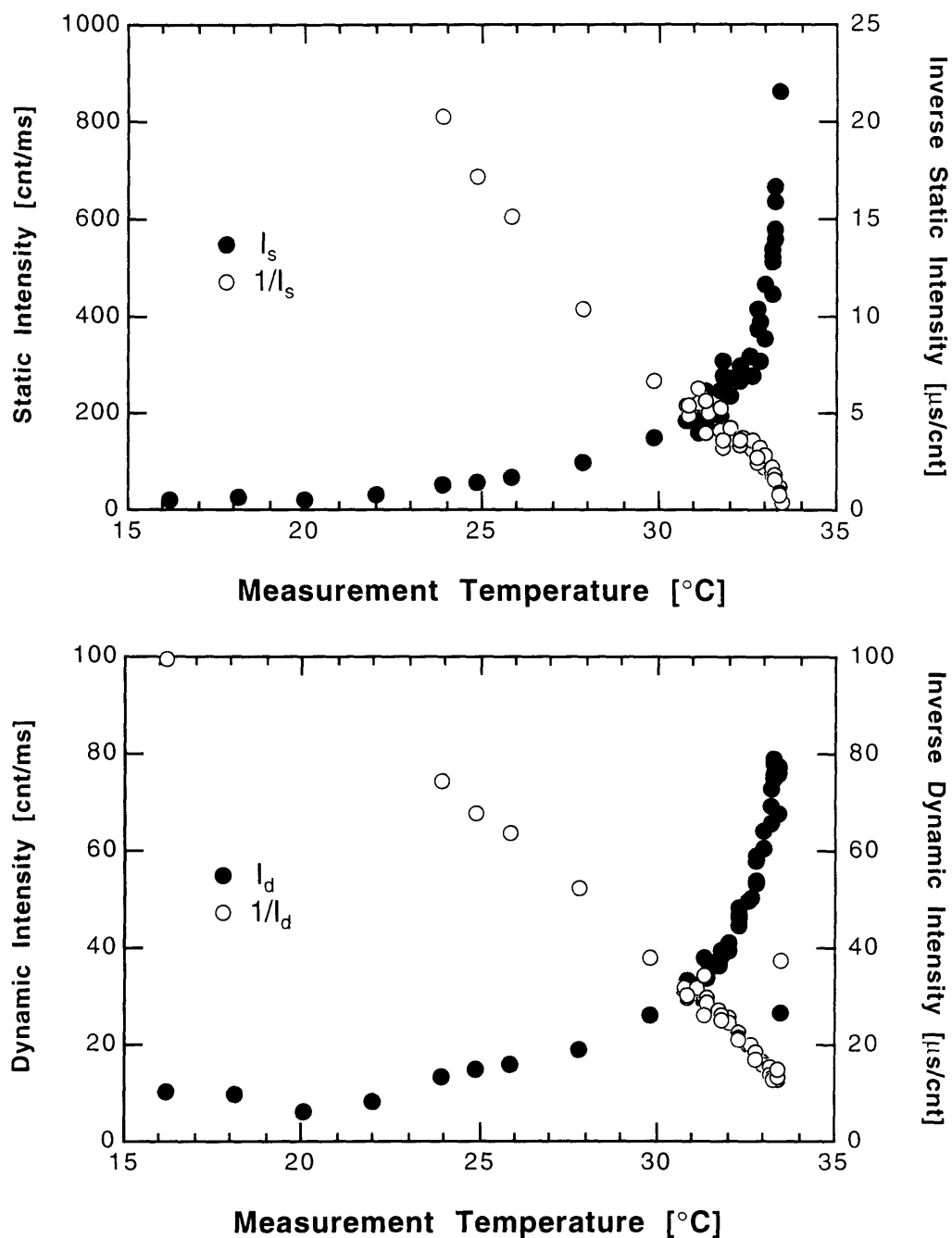


Fig. 5 The amplitude \bar{I}_S , of the spatial fluctuations of scattering intensity, and its inverse, are plotted as a function of the measurement temperature at which the light scattering was carried out (upper graph). The sample was made at 20°C. The amplitude appears to diverge at 20°C. The amplitude of dynamic fluctuations, \bar{I}_D , also diverges (lower graph).

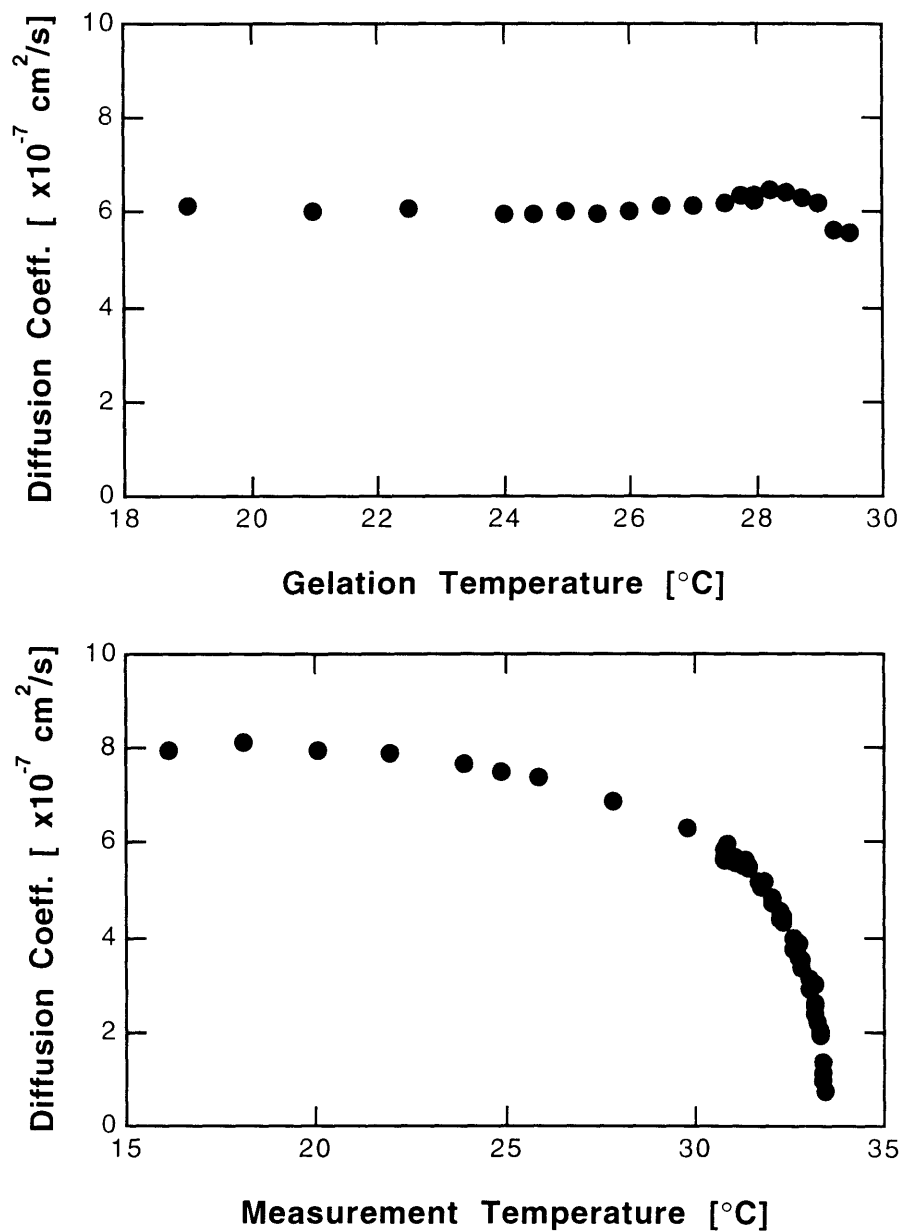


Fig. 6 The collective diffusion coefficient of concentration fluctuations of N-isopropylacrylamide gel (as determined by quasielastic light scattering) is plotted as a function of gelation temperature (upper graph) and of measurement temperature (lower graph). In the first case the measurements were carried out at 23°C. In the second, the gel was prepared at 20°C. In the lower graph the diffusion coefficient diminished at 33.4°C, showing the critical slowing-down.

3.4 DISCUSSION

Generally, one would not need to invoke the frozen concentration fluctuations to explain the positional fluctuation of the scattered intensity in Figures 1 and 3. It can result from the restricted motion of the scatterers (17). However, the data on gelation temperature dependence strongly suggests the existence of frozen concentration fluctuations. In the limiting case of a translucent or opaque gel we know explicitly that their size is at least on the order of the wavelength of light. The fact that \bar{I}_S increases strongly with rising gelation temperature can be interpreted as an effect of larger and larger clusters being formed during the gelation process (see below). The fact that \bar{I}_D and the diffusion coefficient D remain unaffected would indicate that the dynamic fluctuations are due to chains connecting the clusters. Furthermore, the perfect fit by a single exponential in Figure 2 confirms the applicability of the collective diffusion theory to these portions of the gel. The decrease of \bar{I}_D at high gelation temperatures, coinciding with the samples becoming translucent, could be accounted for by the onset of multiple scattering and/or saturation of the photomultiplier tube at high intensity. It could also be interpreted as a decrease in the fraction of chains not bound within the clusters.

The origin of the frozen concentration fluctuations can be understood from the schematic phase diagram as shown in Figure 7, where the horizontal axis indicates the polymer network density and the vertical axis shows the reduced temperature (corresponding to Flory-Huggins interaction parameter (22)). Note that the reduced temperature of N-isopropylacrylamide gels is a monotonically decreasing function of temperature. For a binary system consisting of polymers and solvent, the phase boundary is dependent on the molecular weight of the polymer (22). At the early stage of the gelation process, the effective molecular weight of the polymer is small. The phase boundary of such a system is relatively symmetric with the critical concentration located near 50%. As the polymerization proceeds the effective molecular weight of the polymer increases. The phase boundary moves; the critical reduced temperature decreases and so does the critical concentration. When the gelation threshold is reached, the evolution of the phase boundary in the phase diagram stops. The dynamic fluctuations of the polymer solution will then be frozen in space and give rise to the spatial concentration fluctuations within the gel. The inhomogeneities of the gel structure are then uniquely characterized by the correlation length of dynamic fluctuations at the onset of gelation. This correlation length is determined by the relative location of the state point in the phase diagram with

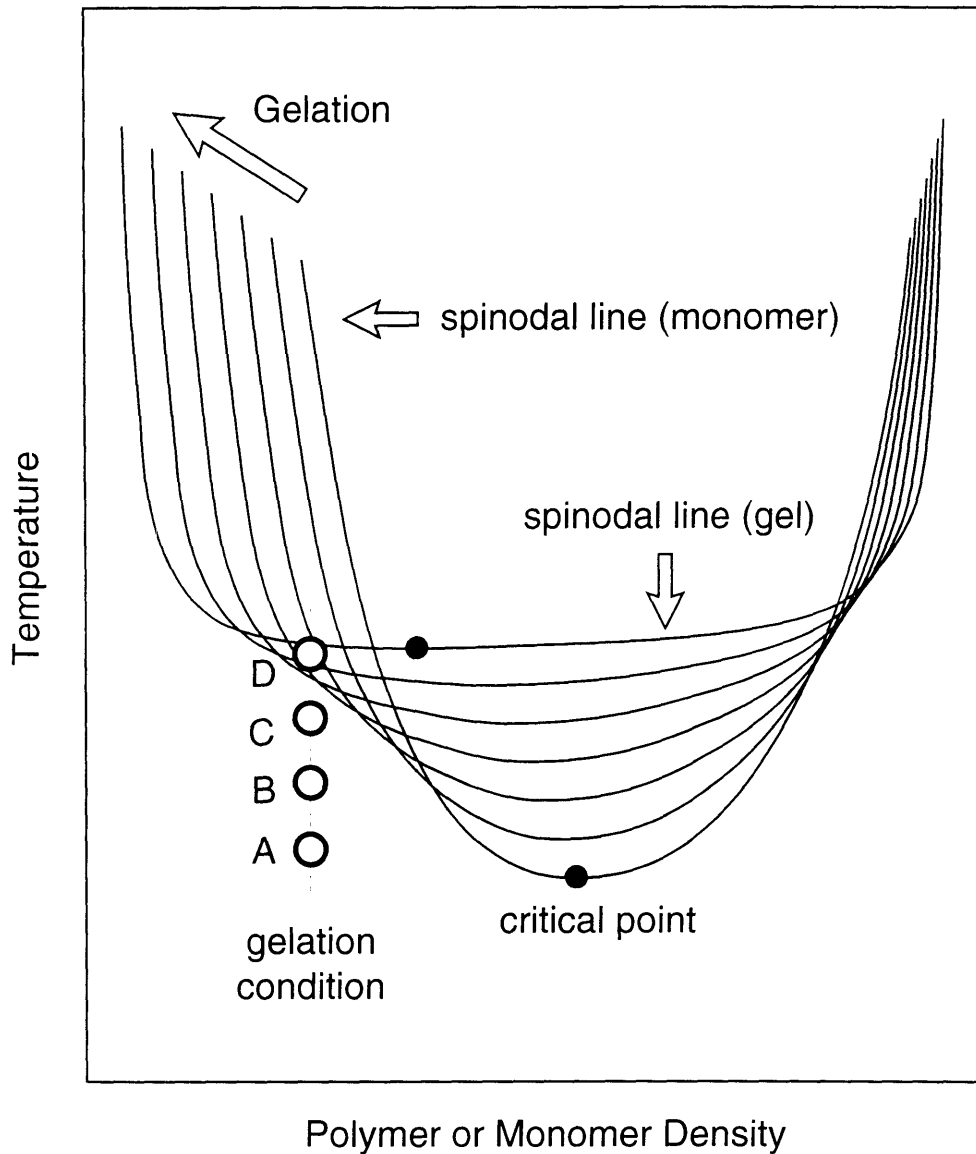


Fig. 7 Schematic phase diagram of the intermediate gelation products (from monomers to a gel). As the gelation progresses the size of polymerized clusters increases and the phase diagram changes from the monomer (the lowest curve) to the gel (the top curve). If gelation occurs far below the spinodal line (points A and B) the gel is homogeneous and clear. If it occurs near the spinodal line (C) the gel is translucent and less homogeneous. If it occurs within the spinodal line the gel is completely opaque (D). Since the monomer phase boundary is below that of a polymer, the opacity will occur even below the gel critical temperature.

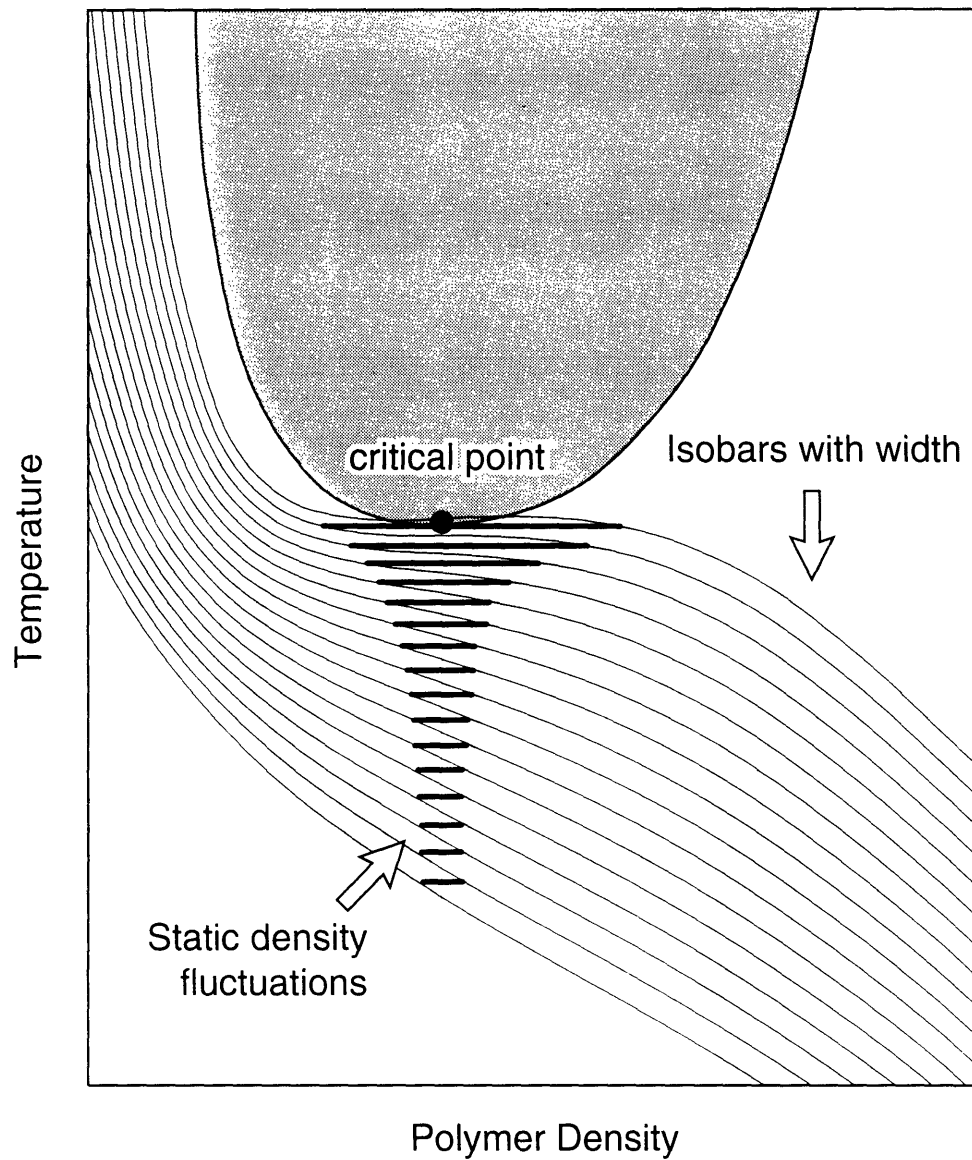


Fig. 8 The isobar of a gel has a width due to the inhomogeneities within the gel. The density distribution is narrow far from the spinodal line, but diverges at the line. This explains why the amplitude of spatial inhomogeneity increases and diverges at the spinodal line.

respect to the phase boundary at the gelation. For gels prepared at high reduced temperatures (for example, point A in Figure 7), the phase boundary is well below this state point, which ensures small fluctuations and a uniform gel structure. The gel made in such a condition is very clear. In contrast, the gels made at lower reduced temperatures (Points B and C in Figures 7), are more inhomogeneous as a result of the increasingly strong dynamic concentration fluctuations, since the state point is near the phase boundary and the pre-critical behavior emerges. The static concentration fluctuations appear to critically diverge at 33.4°C.

It is important to notice that although the structural inhomogeneities are permanently embedded within the polymer network, their amplitude, or the contrast between dense and dilute regions, is enhanced as the gel approaches the spinodal line. This phenomenon can be interpreted as follows. At equilibrium, the osmotic pressure within a gel is homogeneous. Due to the structural inhomogeneities, the isobar is different from place to place within the gel. The isobar for the entire gel is, therefore, represented by a blurred line as illustrated in Figure 8. The distribution of polymer density is indicated by the intercept of the horizontal line at a fixed temperature and the blurred isobar. The distribution is finite far from the spinodal line, but increases and diverges as the reduced temperature approaches the spinodal point. As the gel approaches the spinodal line the originally denser regions become denser, and the originally dilute regions become more dilute. This leads to a larger contrast in the refractive index fluctuations, and thus to a larger light scattering.

CONCLUSIONS

Using light scattering we have studied the origin of structural inhomogeneities within a gel. There are two kinds of permanent structural inhomogeneities, and dynamic fluctuations. All of these are determined by the relative position of the gel state point within the phase diagram either at the onset of gelation process, or at the measurements of inhomogeneities. Therefore, the concept of phase transitions of gel and polymer solution is important to predict the gel network structure. The spatial inhomogeneities, although their structure is permanent, can be enhanced as temperature approaches the spinodal line, and diverge at the line.

The findings and the concept presented here will be useful in controlling the gel structure and thus the physical properties of gels such as permeability, viscoelasticity, and optical clarity. Moreover, the studies presented here show that information may be stored in a distributed way as spatial inhomogeneities within the 3-dimensional gel, and that it can be readily observed by the angular dependence of scattered laser light. This may be useful in various applications including 3-dimensional holography.

FURTHER RESEARCH

There are several interesting unsolved questions concerning the inhomogeneities. For example, the discrepancy between the temperatures of divergence for static and dynamic scattering is not addressed here (but see (23)). The inhomogeneities created near gelation threshold are also an interesting problem.

The gelation temperature was shown to be a parameter influencing the static intensity (which is directly related to the inhomogeneities in a gel). It would be interesting to systematically study its dependence on other parameters. These would certainly include the network concentration, which can be controlled either by preparing the gel at the desired volume fraction, or by swelling the gel. These need not be equivalent, since the conformation of the polymers is expected to be different in both cases – the chains can be assumed to be Gaussian when the gel is made, but become stretched as the gel swells. Comparison of the two should be interesting. Another parameter that would certainly affect the inhomogeneities is the crosslinking ratio.

The study of these questions will lead us to better understanding of the structure and properties of polymer gels.

REFERENCES

- [1] Weiss, N. and Silberberg, A.: *Polym Prep. Am. Chem. Soc., Div. Polym. Chem.* **16** (2) 289 (1975).
- [2] Weiss, N., van Vliet, T. and Silberberg, A.: *J. Polym. Sci., Polym. Phys. edition* **17**, 2229 (1974).
- [3] Hsu, T.P., Ma, D.S. and Cohen, C.: *Polymer* **24**, 1273 (1983).
- [4] Stanford, J.L. and Stepto, R.F.T.: *Polym. Prepr.* **22**, 165 (1981).
- [5] Funke, W.: *Plastics and Rubber Processing and Applications*, **3**, 243 (1983).
- [6] Hecht, AM., Duplessix, R. and Geissler, E.: *Macromolecules*, **18**, 2167 (1985).
- [7] Candau, S.J., Ilmain, F., Schosseler, F. and Bastide, J.: *Mat. Res. Soc. Symp. Proc.*, **177**, 3 (1990)
- [8] Richards, E.G. and Temple, C.J.: *Natural Physical Science* **230**, 92 (1971).
- [9] Bansil, R. and Gupta, M.K.: *Ferroelectrics* **30** 64 (1980).
- [10] Suzuki, Y., Nozaki, K., Yamamoto, T., Itoh, K. and Nishio, I.: *J. Chem. Phys.*, **97**, 3808 (1992).
- [11] Dusek, K. in *Polymer Networks*, eds. A.J. Chompff and S. Newman. Plenum, New York, pp. 245-260 (1971).
- [12] Tanaka, T.: *Phys. Rev.* **A17**, 763 (1978).
- [13] Tanaka, T., Ishiwata, S. and Ishimoto, C.: *Phys. Rev. Lett.* **38**, 771 (1977).
- [14] Hockberg, A. and T. Tanaka, T.: *Phys. Rev. Lett.*, **43** 217 (1979).
- [15] Munch, J.P., Candau, S., Duplessix, R., Picot, C., Herz, J. and Benoit.: *J. Polym. Sci. Polym. Phys. Ed.*, **14**, 1097 (1976).
- [16] Goldbart, P., and Goldfeld, N.: *Phys. Rev. Lett.*, **58**, 2676 (1987).
- [17] Pusey, P. N. and van Megen, W.: *Physica A*. **157**, 705 (1989).
- [18] Chu, B.: *Laser light scattering*, Academic Press, London (1991).
- [19] Joosten, J.G., McCarthy, J.L., Pusey, P.N.: *Macromolecules*, **24**, 6690 (1991).

- [20] Fang, L. and Brown, W.: *Macromolecules*, **25**, 6897 (1992).
- [21] Skouri, R., Munch, J.P., Schosseler, F. and Candau, S.J.: *Europhys. Lett.*, **23**, 635 (1993).
- [22] Flory, P.J.: *Principles of Polymer Chemistry*, Cornell Univ. Press, Ithaca, pp. 495-540 (1953).
- [23] Rabin, Y. and Onuki, A., to be published

CHAPTER 4

PHASE DIAGRAM OF NIPA MONOMER

This chapter does not deal directly with light scattering, but it helps understand the results obtained in the previous chapter (on gel inhomogeneities). The formation of the frozen gel inhomogeneities during the gelation process depends on the phase properties of all the participants of the gelation process: monomers, dimers, oligomers, linear chains of various lengths, branched polymer clusters, etc., up to the whole gel. Among them the monomers and the whole gel play a key role as the most extreme cases. The phase diagram of the NIPA gel is well established (*1*), but the monomer diagram had to be determined. This is the goal of this chapter.

A complete phase diagram of N-isopropylacrylamide monomer is obtained and compared to that of the corresponding polymer and gel. It is observed that the solution undergoes a binary liquid phase separation. The liquid-liquid and solid-liquid coexistence curves are determined. They are found to intersect each other, so a triple point is measured. The existence of a lower critical point for the binary liquid mixture is demonstrated, though not explicitly observed, because it occurs below the solid-liquid line. A simple model qualitatively accounting for this phase behavior is presented.

4.1 INTRODUCTION

The N-isopropylacrylamide (here called NIPA) gels are among the best studied ones. The same is true about Poly(NIPA) polymers. A testimony to that is a recent

monograph on Poly(NIPA) by Schild (2), and the references therein. One of the interesting aspects of Poly(NIPA) is that its water solutions exhibit a lower critical solution temperature (LCST), that is at low temperatures the polymer is miscible with water, while at high temperatures it undergoes a binary liquid phase separation. This inverted temperature dependence is characteristic of hydrophobic systems where the entropy change associated with introducing a chain into the aqueous solution is negative (see, e.g., Taylor et al. in (3)). Fujishige et al. (4) studied the phase diagram of various Poly(NIPA) molecules and determined that it is rather flat as a function of concentration. Moreover, it is independent of the molecular weight in the range studied ($M=5 \cdot 10^4$ – $8.4 \cdot 10^6$). The NIPA gel phase diagram was determined by Hirotsu et al. (1) (reproduced in Figure 2). It is also quite flat, except for the extremes (concentration $\phi \approx 0$ and $\phi \approx 1$). An interesting feature is that the critical temperature for the gel is several degrees higher than that of a polymer (34.6°C from (1) versus $\sim 30^\circ\text{C}$ from (4)).

Given the extensive study of NIPA polymers and gels it seemed relevant to determine the phase diagram of the NIPA monomers. There are several important implications of that. First, the phase behavior of polymers is governed to a large extent by the monomer unit interactions. Second, they influence the processes of polymerization and gelation. The formation of frozen inhomogeneities in the gel was of particular interest here. Phase separation occurs first at a microscopic level. If during the gelation process any of the components is brought into its phase separation zone, one can expect the phase separated micro domains to be frozen in the form of permanent inhomogeneities in the gel network (as reported in Chapter 3).

Models describing the phase behavior of a gel system are well established and accepted (1, 5). Here we present a simple model that qualitatively accounts for the observed properties of NIPA monomer solution.

4.2 EXPERIMENTS

N-Isopropylacrylamide monomers from Kodak Chemical Co. were used. They contain a small amount of inhibitor, necessary to prevent spontaneous polymerization at elevated temperatures. A comparison with purified NIPA at lower temperatures showed no effects of the inhibitor on the phase diagram of NIPA.

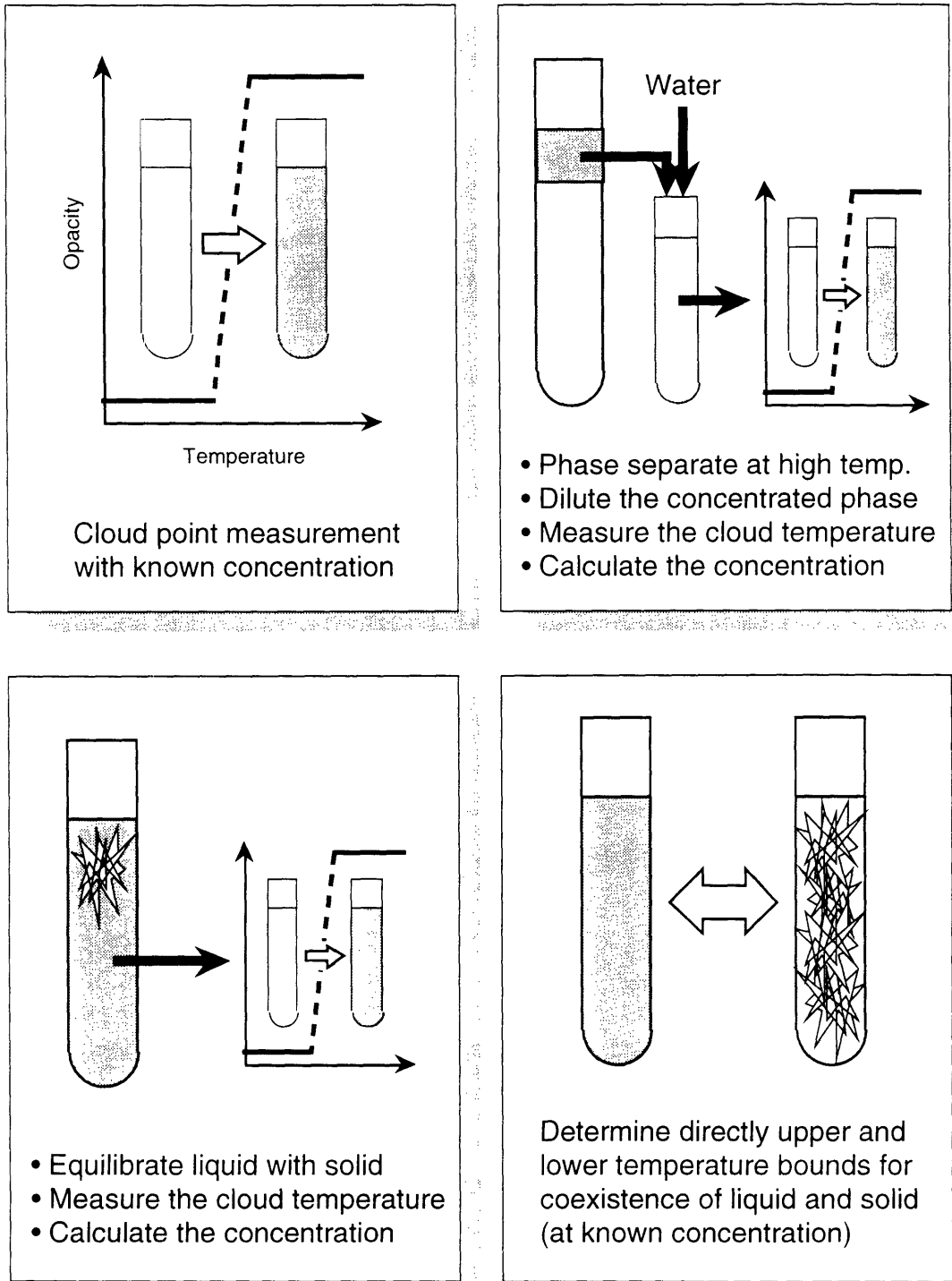


Fig.1 Experimental methods used in determining the phase diagram. UV absorption measurements at known concentration (not illustrated) were also performed. The cloud point measurements (top left) were used to calculate the concentration in other instances.

4.2.1 Liquid-Liquid Phase Boundary

Several methods were used to determine the liquid-liquid phase boundary (see the schematic diagram in Figure 1). First of them involved a direct measurement of the cloud point for a solution of known concentration. The cloud point was determined visually by placing the solution in a micropipette (100 μ l) and immersing it in a cell with water circulating through a temperature controller (Neslab). As the temperature was repeatedly raised and lowered, the cloud point was observed with an accuracy of $\pm 0.1^\circ\text{C}$. Given a very steep concentration dependence of the cloud point in this range the data was very consistent. This set of data was also used as a reference to determine the concentration when T_{cloud} was known (see below). The other methods involved phase separating the solution at a given (high) temperature, extracting the phases and determining their concentration. This was done either by UV spectrometry (with the spectrometer calibrated by NIPA solutions of known concentration), or by determining the cloud point (as above) and using the reference (the first set of data) to calculate the concentration. The supernatant (concentrated) phase was diluted with a measured amount of water (about 1:4.5 ratio) to bring it into range accessible to the methods just described.

4.2.2 Solid-Liquid Phase Boundary

The solid-liquid phase boundary was determined in two ways (shown schematically in Figure 1). In the low-concentration regime the solution was left for several days to equilibrate with the crystalline phase. The liquid was then collected and heated until its cloud point was reached (as described above). The concentration was determined from the cloud temperature using the reference described above.

In the high concentration region solutions of known concentration were prepared by dissolving NIPA at an elevated temperature. The temperature was then adjusted, gradually narrowing the range between completely dissolved and crystallized conditions. Thus the boundary was determined to $\pm 0.5^\circ\text{C}$. The melting point was taken from the manufacturer's specifications.

4.3 RESULTS

Figure 2 summarizes the results, presented in the form of a phase diagram. Different markers are used for data obtained by each of the methods described above. The

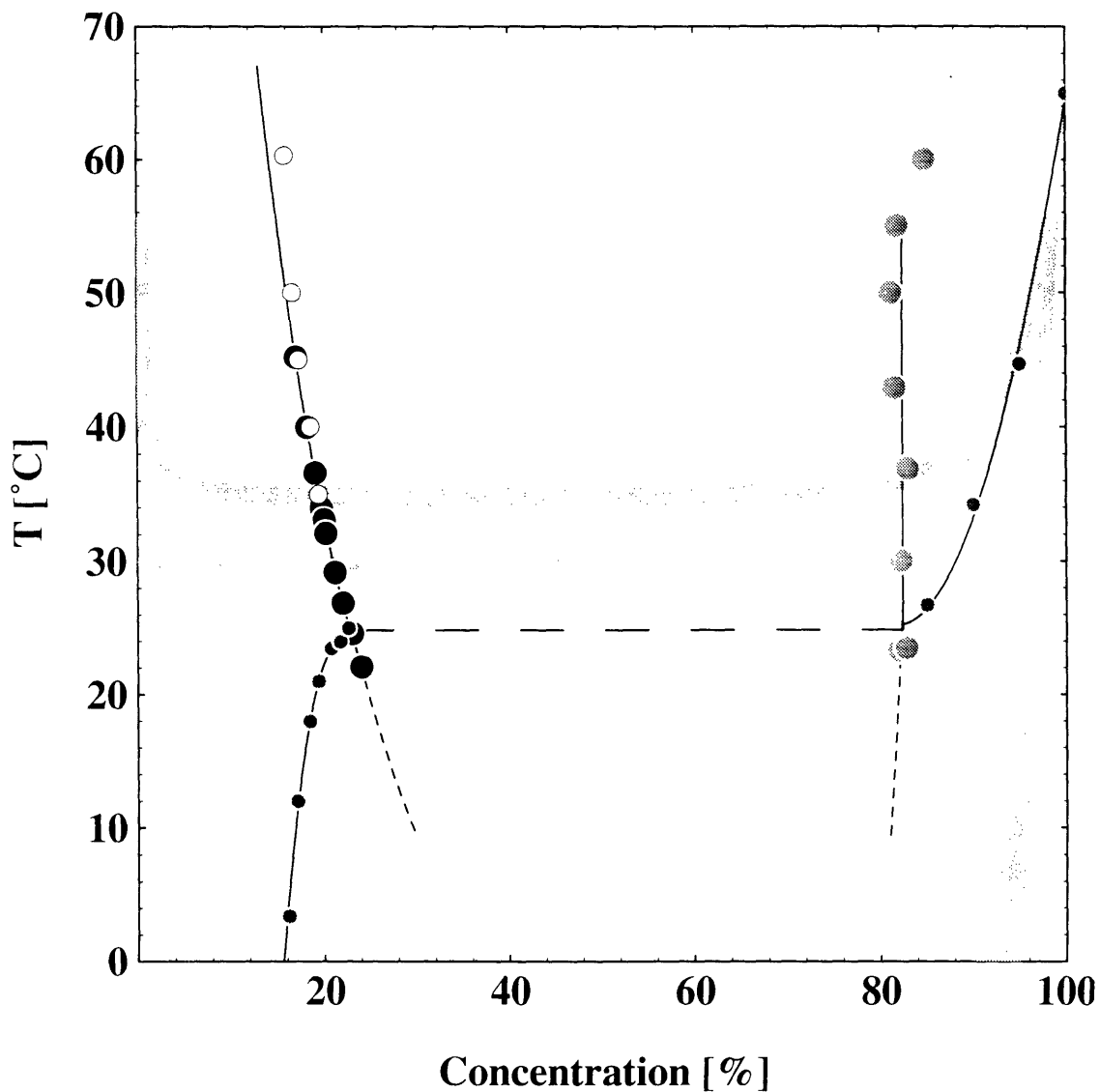


Fig. 2 Observed phase diagram of the NIPA monomer. Black circles -- T_{cloud} measured for given concentration ϕ ; open circles -- ϕ measured by UV spectrometry; gray circles -- T_{cloud} measured for unknown ϕ , ϕ then determined by fitting to the black circles. Small circles -- solid-liquid boundary. Dashed line marks the triple point (coexistence of one solid and two liquid phases). The gray region represents a hypothetical concentration of a hydrated solid. The heavy solid line is the NIPA gel phase diagram (from (1)). The heavy dashed line is the Poly(NIPA) phase diagram (after (4)).

critical point of the liquid-liquid transition was not observed because it occurs well into the solid region. Several points represent a supercooled liquid (from which the solid phase subsequently precipitated). The triple point at which one solid and two liquid phases coexist (marked by a thin dashed line on Figure 2) was determined to be 24.9°C and corresponds to $\phi=22.8\%$ and $\phi=82.4\%$. Figure 2 also schematically summarizes the phase behavior of a NIPA gel (heavy solid line – from (1)) and a NIPA polymer (heavy dashed line – according to (4)). It is important to observe that the gel and polymer critical points ($\sim 35^\circ\text{C}$ and $\sim 30^\circ\text{C}$) are much higher than the critical point for the monomer (around or below 0°C). Also, no crystalline phase exists in the case of gels and polymers.

4.4 DISCUSSION

A simple qualitative model can be used to describe the behavior of this system. Let's consider the liquid-liquid case first. The chemical potential of the NIPA monomer in the liquid phase (μ_L) can be, in the first approximation, represented by

$$\mu_L(\phi, T) = \mu_L^\circ(T) + k_B T \ln \phi + k_B T (1 - \phi)^2 \chi$$

where ϕ is the concentration of the NIPA monomer. The first term is the chemical constant, representing the energy change when one NIPA molecule is brought into pure water, the second represents the mixing entropy, while the third -- the solute-solvent interaction. Here χ is the Flory parameter (6) defined as $\chi = (\Delta H - T\Delta S) / 2k_B T$, with ΔH and ΔS representing respectively the changes of enthalpy and entropy (per molecule). They are taken to be constants independent of temperature. In order to produce a lower critical point both ΔH and ΔS must be negative. The latter can be explained in terms of a hydrophobic interaction where the presence of a hydrophobic molecule causes the formation of ice structure in water surrounding the molecule, thus decreasing the entropy. The critical point is determined by the conditions $\partial\mu_L / \partial\phi = \partial^2\mu_L / \partial\phi^2 = 0$. It occurs at

$$T_c = \Delta H / (\Delta S + 4k_B)$$

$$\phi_c = 1/2$$

Above this temperature the equilibrium concentrations can be found using the Maxwell loop construction (see, e.g., (7)). Around the critical point they exhibit the $|T - T_c|^{1/2}$ behavior characteristic of a mean field theory.

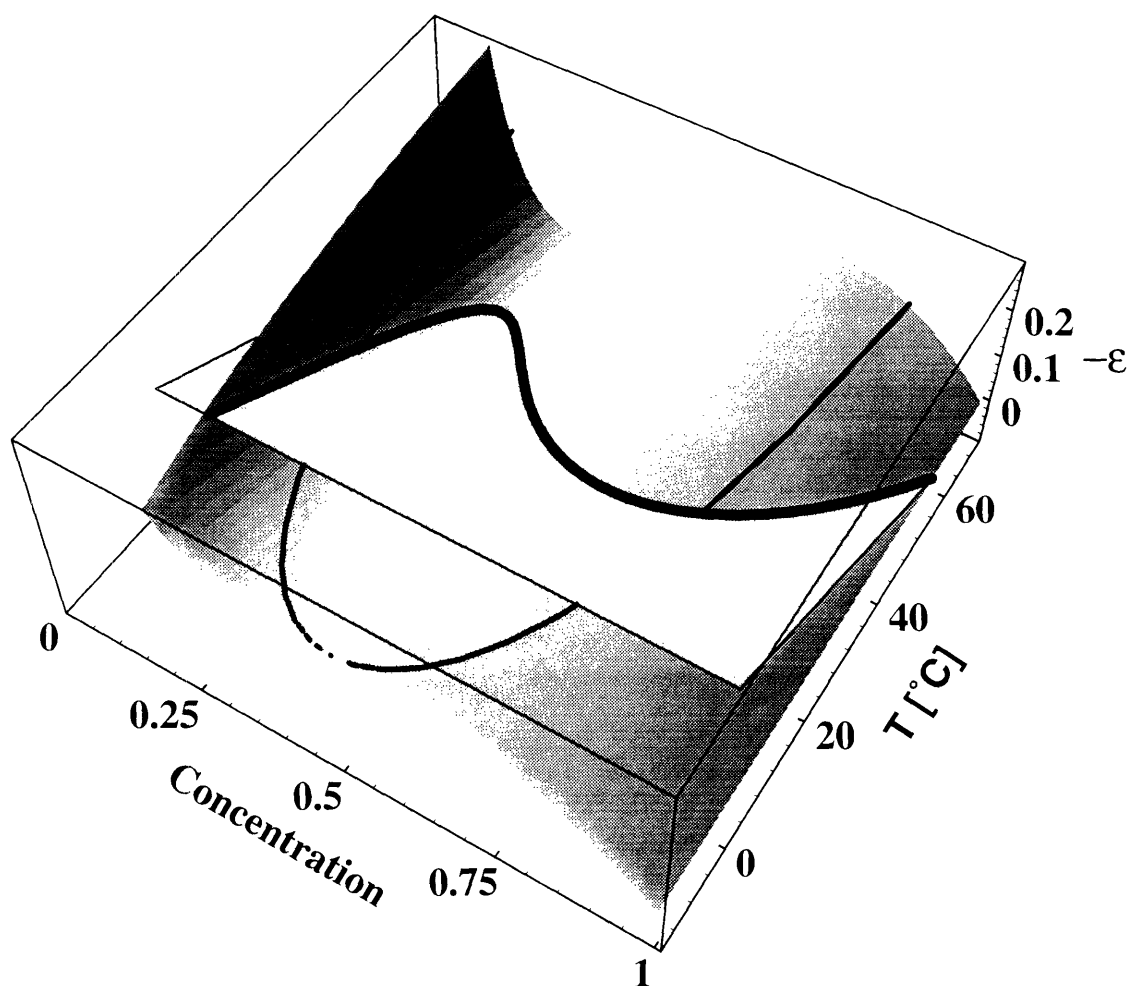


Fig. 3 The intersection of the plane of $-\varepsilon(T)$ (light gray) with the surface of $-v(\phi, T) \equiv -(T/T_c)[\ln \phi + (1-\phi)^2 \chi]$ determines the solid-liquid coexistence curve (thick line). Note that $\varepsilon(T)$ is independent of concentration, so the plane is used only to determine the concentration at which $\varepsilon(T) = v(\phi, T)$. The negatives are plotted, so that at any given point the upper surface corresponds to the stable phase. Thus at low temperatures and concentrations larger than ~ 0.1 the solid phase is stable (i.e., the system can separate into a solid phase and a dilute liquid). At higher temperatures the solid is unstable and is dissolved. The liquid-liquid boundary is also plotted (thin line). In the regions where the liquid phase is preferred, it can further separate into dilute and concentrated phases (to the left and to the right of the thin line).

In this simple model the solid phase is assumed to be anhydrous. This is not strictly true, but the water concentration in the NIPA crystal cannot be very significant. (An experiment on dehydration of NIPA at elevated temperature failed because the NIPA sublimated away.) The chemical potential of the solid (μ_S) is thus assumed to depend only on temperature. In general, the chemical potential of a solid can be written (7):

$$\mu_S(T) = -\eta - T \int_0^T \frac{dT'}{T'^2} \int_0^{T'} c(T'') dT''$$

where $c(T)$ is specific heat per molecule and η the latent heat of dissolving at $T=0$. The double integral is a positive increasing function of temperature. Thus μ_S is a decreasing function of temperature. Furthermore, over the range of interest (which is small on the absolute scale), it can be assumed that the decrease is linear with T .

The solid-liquid coexistence curve is thus determined from the condition $\mu_S(T) = \mu_L(\phi, T)$. This can be rewritten in terms of a non-dimensional quantity $\varepsilon(T) = (\mu_S(T) - \mu_L^0(T)) / k_B T_c$ as

$$\varepsilon(T) \cdot k_B T_c = k_B T \ln \phi + k_B T (1 - \phi)^2 \chi \quad (1)$$

We take $\varepsilon(T)$ to depend linearly on temperature in the range of interest. Figure 3 shows the solid-liquid curve as an intersection of surfaces determined by LHS and RHS of (1).

Figure 4 shows the results obtained from this model when the parameters were adjusted to match the actual data. The liquid parameters were $T_c = -15^\circ\text{C}$, $\Delta S = -8.02 \cdot k_B$ ($-1.16 \cdot 10^{-15}$ erg/K). This gives $\Delta H = -4.02 \cdot k_B T_c$ ($-1.43 \cdot 10^{-13}$ erg). This value is quite close (given different conditions and the crudeness of this model) to the value that Hirotsu et al. (1) reprints (from (8)) for a NIPA polymer in aqueous solution: $\Delta H = -0.87 \cdot 10^{-13}$ erg.

The concentration-independent factor ε was taken to be $\varepsilon(T) = -1.73 + T[\text{K}]/190$. It should be noted that this is an increasing function of temperature, while $\mu_S(T)$ was said to decrease with T . This requires that $\mu_L^0(T)$ decrease even faster than $\mu_S(T)$. This is reasonable, because the hydrogen bonding in water is stronger at lower temperature, so the penalty for breaking it by introducing a NIPA molecule drops with T .

It is interesting to compare the behavior of the monomers with that of polymers and gels. One observes that at a given temperature the monomer solution can exist in a single phase up to a much higher concentration than either polymer or gel. This is especially striking in the case of the polymer. The phase diagram seems to be flat up to an

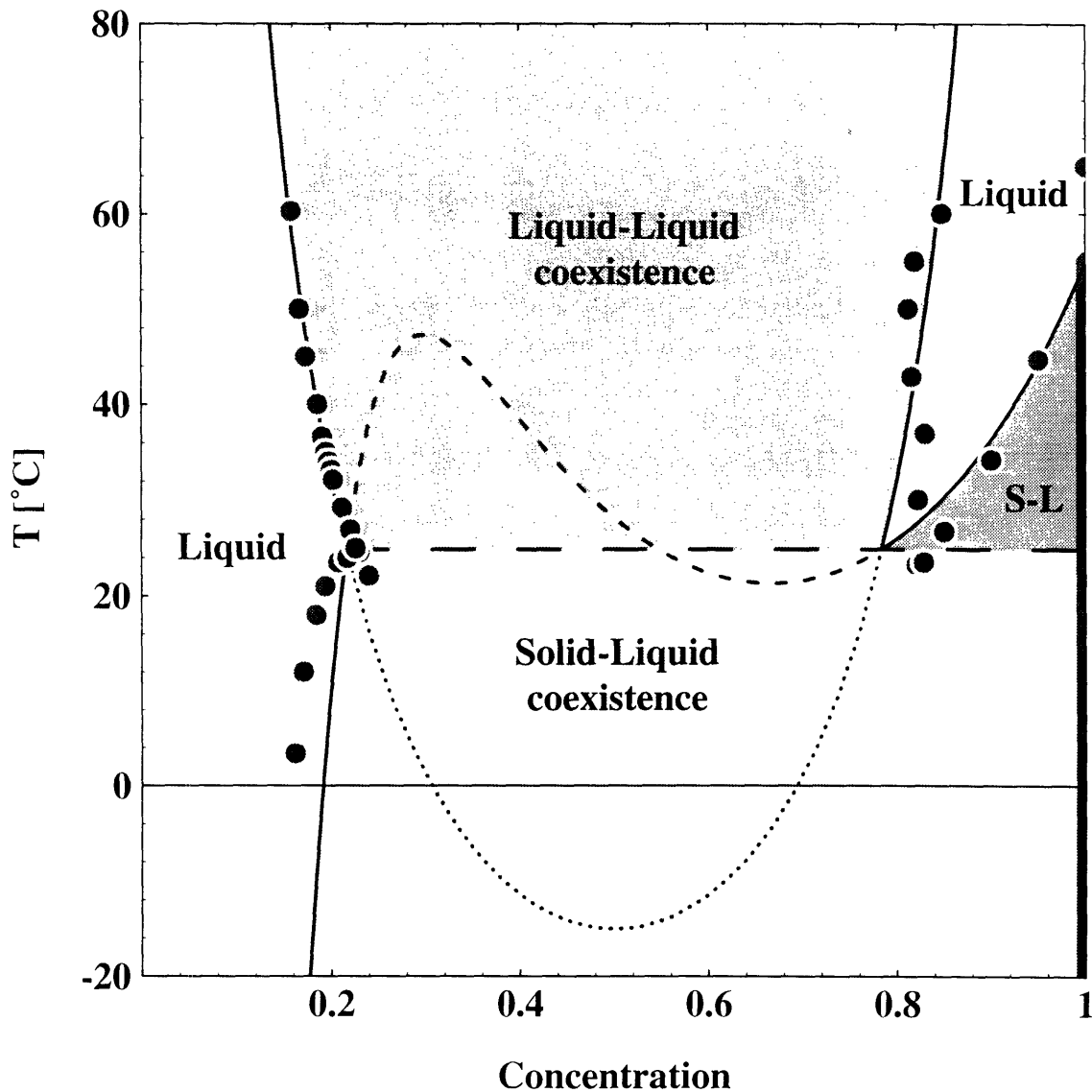


Fig. 4 Plot of the model results with the experimental data. The different regions are also marked. Solid lines represent the coexistence curves. The wide-dashed line is the marks the triple point – the place where two liquid phases and the solid ($\phi=1$) coexist. Two white areas represent the regions where dilute and concentrated liquids exist in a single phase. The gray area between them stands for the liquid-liquid coexistence. The solid is marked by the thick line at $\phi=1$. It can coexist with dilute liquid (light gray area) or concentrated liquid (dark gray). The narrow-dashed line marks the Maxwell loop of the solid-liquid coexistence. The dotted line extends the liquid-liquid line into the region where solid forms.

infinitesimal concentration, while pure water ($\phi=0$) exists in a single phase. This paradox is resolved when one considers that for a dilute polymer (different chains are not in contact) the local concentration of monomer units is fixed by the fact that they are linked together. It is independent of the "global" polymer concentration. Therefore the polymer can still collapse (coil-globule transition - see (6)). It seems that the gel behavior is intermediate between that of a monomer and a polymer. It might be related to the fact that the chains in a gel behave like polymers of length corresponding to the distance between the crosslinks (order 100) – much shorter than the linear polymers discussed.

CONCLUSION

It was observed that the phase diagram of NIPA monomer is qualitatively similar to that of Poly(NIPA) and of NIPA gels, at least in the liquid part. The hydrophobic interaction of the monomers manifests itself in the occurrence of a lower critical solution temperature in all three cases. Quantitatively there is a huge difference. The critical point of a monomer solution is much lower than in the other two cases. Dilute monomers can exist in a single phase in concentrations much higher than the gels and the solutions (and concentrated monomers in much lower). Finally, the crystallization occurs in monomers, while it is not observed in polymers and gels.

FURTHER RESEARCH

Given the original motivation of this project – determining the phase behavior of all the participants of the gelation process, including the intermediate products, it would be interesting to consider at least NIPA dimers, and other very low molecular weight Poly(NIPA) chains. One can reasonably expect them to fall somewhere between the coexistence curve for monomers and for gels, but the exact transition is hard to estimate.

It would be interesting to see at which molecular weight does the coexistence curve of these oligomers cross the point at which the gel is prepared. If this happens at a low molecular weight we can expect large gel inhomogeneities to be formed (since the mobility of small molecules is high). If it happens at high molecular weight, then the critical fluctuations should have little effect on the gel formation, and another explanation should be found to explain the origin of gel inhomogeneities. These experiments can reveal many interesting aspects of the gelation process.

REFERENCES

- [1] Hirotsu, S., Hirokawa, Y. and Tanaka, T.: *J. Chem. Phys.*, **87**, 1392 (1987).
- [2] Schild, H.G.: *Prog. Polym. Sci.*, **17**, 163-249 (1992).
- [3] Taylor, L.D. and Cerankowski, L.D.: *J. Polym. Sci. Pt. A: Polym. Chem.*, **13**, 2551 (1975).
- [4] Fujishige, S., Kubota, K. and Ando, I.: *J. Chem. Phys.*, **93**, 3311 (1989).
- [5] Tanaka, T., Fillmore, D., Sun, S.T., Nishio, I., Swislow, G. and Shah, A: *Phys. Rev. Lett.*, **45**, 1636 (1980).
- [6] Flory, P.J.: *Principles of Polymer Chemistry*, Cornell Univ. Press, Ithaca, pp. 495-540 (1953).
- [7] Reif, F.: *Fundamentals of Statistical and Thermal Physics*, McGraw-Hill, New York, (1963).
- [8] Ito, S. and Mizoguchi, K.: *Sen-i Kobunshi Zairyo Kenyuusho Houkoku (Bulletin of Fiber and Polymer Research Laboratories, in Japanese)*, **114**, 7 (1984).

CHAPTER 5

LIGHT SCATTERING FROM A NIPA GEL NEAR A TEMPERATURE INDUCED PHASE TRANSITION

The previous two chapters dealt with N-isopropylacrylamide (NIPA). They explored the origin of inhomogeneities in a gel and the significance of the NIPA monomer phase diagram in the process of gelation of NIPA. This chapter goes into more depth dealing with a subject that was introduced in Chapter 3 – the temperature of measurement dependence of light scattering from a NIPA gel made at a relatively low temperature, away from the critical fluctuations of the pre-gel solution (thus more homogenous). The experiments described in this chapter demonstrate various aspects of light scattering near the discontinuous volume transition of a NIPA gel. This system has been investigated before, but the light scattering data from a collapsed NIPA gel are new. It is presented together with the data from a swollen gel. The relevance of several of the models described in previous chapters (Chapter 2 and Chapter 3) is confirmed by these experiments. Furthermore, new light is shed on the question of network-solvent friction, as the scattering data seemingly contradict results obtained by mechanical measurements by other authors.

5.1 INTRODUCTION

As mentioned previously, the NIPA gel is quite well studied (see the monograph by Shild (1) and the references therein). In particular, swelling (2-7), light scattering (4-

5), Small Angle Neutron Scattering (SANS) (6), molecular transport (7), and forced flow friction (8) experiments were performed in this lab. NIPA gel is interesting, because it exhibits a lower critical temperature: the gel is homogenous below this temperature, but can coexist in two phases above it. This is different from the behavior of most other gels, which tend to exhibit an opposite temperature dependence. The swelling curve is also inverted – the gel is collapsed at high temperature and swollen at low temperature. This is opposite to what one would expect from a simple physical intuition: normally at high temperatures the increased entropy contribution would shift the free energy minimum towards the swollen gel (lower restriction on chain conformations thus higher entropy). As explained in Chapter 4 (see also (9)), the NIPA units are highly hydrophobic, so the entropic contribution from moving them apart is negative, therefore the gel collapses, rather than swelling at a high temperature.

Figure 1 shows the chemical structure of both a NIPA unit and a crosslinker unit – N,N'-methylenebisacrylamide (BIS). It is the hydrocarbon chain attached to the amide group that makes NIPA hydrophobic.

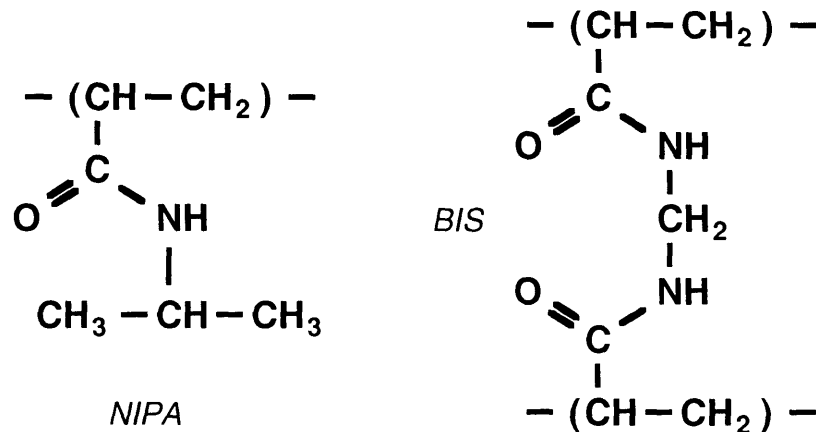


Fig. 1 Chemical structure of the units of N-isopropylacrylamide (left) and N,N'-methylenebisacrylamide (BIS, right). NIPA unit has a hydrocarbon group that makes it hydrophobic. BIS unit can be linked to two separate chains. It acts as a crosslinker.

5.2 EXPERIMENTS

5.2.1 Sample Preparation

The gels used throughout this chapter were formed by free radical copolymerization of 7.8g of N-isopropylacrylamide (Kodak Chemical, purified by recrystallization) and N,N'-methylenebisacrylamide (0.130g) in 100ml of deionized water. 240 μ l of Tetramethylethylenediamine (TEMED) were used as accelerator. Thus prepared pre-gel solution was filtered using a 0.22 μ m filter and degassed in vacuo for 10-15 minutes. Finally 43mg of ammonium persulfate (initiator) were added and the solution transferred into a test tube holding some open micropipettes. The temperature of the gelation process was kept at 20°C by immersing the test tube into a circulating heat bath (Lauda model RM 6). After allowing 18 hours for gelation the micropipettes were extracted from the bulk of the gel. All measurements were performed on a sample that has never been taken out of the micropipette in which it was made. Two different sets of samples prepared according to the same recipe were used – one for the swollen gel (for temperatures below the transition temperature- to be called Batch A) and one for the collapsed gel (Batch B).

5.2.2 Temperature

Temperature was the independent parameter in this series of experiments. The temperature of the sample was stabilized to within 0.01°C using a computer-driven thermoelectric temperature controller (see the apparatus description in the Introduction). The temperature was changed in small steps, especially near the transition where the kinetics was expected to be slow. In the case of Batch A, 2 hours were allowed for equilibration between two sets of measurements. The collapsed gel was left alone for at least a day before a new set of data was taken and several days were allowed for the phase transition itself.

5.2.3 Approach to the Transition

Figure 2 shows the path followed during the experiment. At low temperatures the gel was kept at its original diameter d_0 , being constrained by the micropipette (thus the points lay on an isochore). Close to the transition point the gel started shrinking below d_0

(now following an isobar). Finally, after the transition the gel was unconstrained in an excess of solvent (expelled from the gel). However, for the collapsed gel the diameter remains almost independent of temperature. Thus it can be said that, with the exception of the immediate vicinity of the transition, the experiments followed two segments of an isochore.

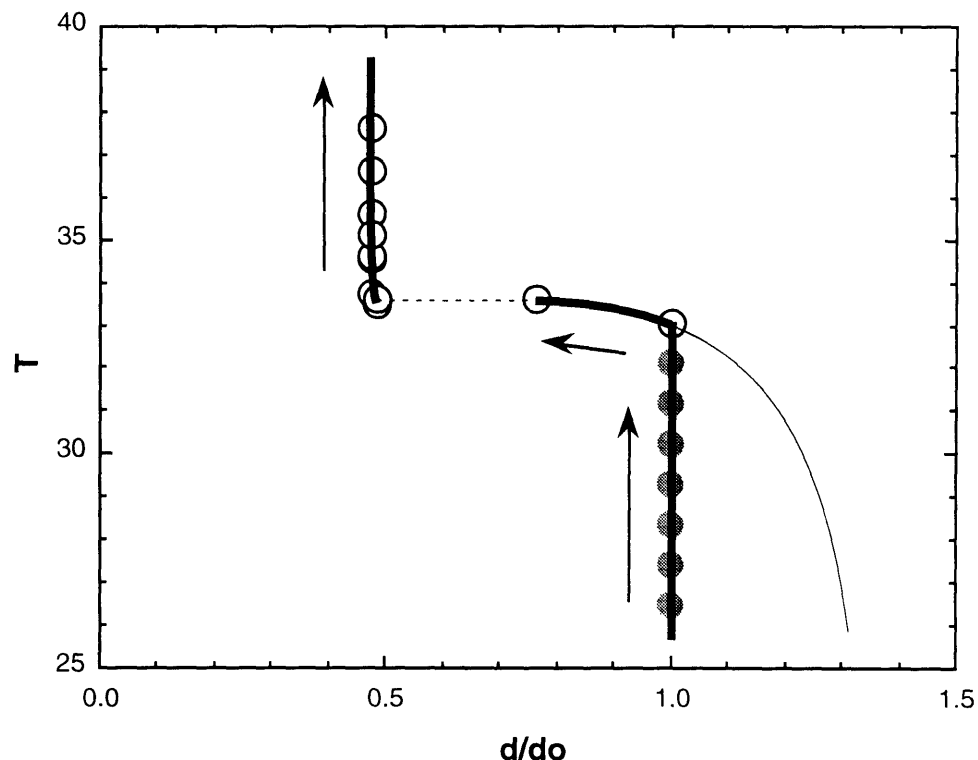


Fig. 2 Swelling curve of a NIPA gel. The circles represent actual data points for collapsed gel. The heavy line is the path followed. The gel is constrained by the micropipette in which it was made to have $d/d_0 \leq 1$, so it follows the isobar only after it starts shrinking. The dashed line represents the discontinuous transition.

5.2.4 Light Scattering

The scattered light intensity and the intensity auto-correlation function were determined at an angle of 90° using the microscopic laser light scattering setup described in the Introduction to this thesis. In the case of Batch A the auto-correlation function was collected with a Brookhaven BI-2030AT correlator with 136 linear channels. For Batch

B the software correlator with logarithmically spaced channels (described in Chapter 1) was used. The sample cell was mounted on a microscope stage, which could be moved perpendicularly to the scattering plane by a stepping motor (see Introduction) to perform the measurements at different locations. A step size of $7.5\mu\text{m}$ was used.

Because of the samples' nonergodicity the method outlined in Chapter 2 was used to analyze the data. Raw correlation functions were measured at N different locations obtained by laterally translating the sample. They were summed and normalized forming an approximation $g_N^{(2)}(t)$ to the ensemble average $g_E^{(2)}(t)$. $N=50$ was used for Batch A and $N=150$ for Batch B. This translates respectively to 14.1% and 8.2% accuracy in obtaining the average intensity (see Chapter 2).

Since the scattering from Batch A and Batch B was done using a slightly different optical setup, the absolute value of the scattering intensity (which is apparatus-dependent) was expected to be different between the two batches. To be able to compare them directly, the intensity from Batch B was multiplied by a factor of 1.41. This value was chosen so that the dynamic intensity from Batch A and B would overlap at the same temperature. The dynamic intensity was chosen as a standard because the gels of Batch A and B were prepared separately, and experiments indicate (see Chapter 3) that it is the static intensity that is much more sensitive to the sample preparation.

The decay time τ was obtained by fitting $g_N^{(2)}(t)$ with a single exponential $A e^{-t/\tau^*} + B$ and then correcting τ^* for heterodyning of \bar{I}_D with $\langle I_S \rangle_N$ (see again Chapter 2).

5.3 RESULTS

5.3.1 The Transition

It is very easy to induce a phase transition in the NIPA gel – one just has to heat it and it collapses. However, due to microphase separation, the gel becomes opaque (white). This state persists indefinitely. It is impossible to perform light scattering measurements from a gel in this state. It was observed, though, that if the temperature is brought to the vicinity of the phase transition and then changed very slowly, the gel remains fully transparent. This observation allowed for the light scattering study of the collapsed gel. The phase transition was very slow – it took several days during which the gel was kept at the temperature of 33.5°C . For several days both phases (swollen and

collapsed) were observed to coexist. Figure 3 reproduces a photograph of a gel in which two phases coexist. As the time progresses the boundary moves towards the swollen end (more and more of the gel collapses).



Fig. 3 A microscope photograph of the coexistence of swollen and collapsed portions of the NIPA gel. The left side of the gel is collapsed, the right is swollen. Both are transparent. The boundary between the two is opaque. The height of the picture corresponds roughly to 1mm. The gel temperature is 33.5°C.

5.3.2 Correlation Functions

Figure 4 shows some typical normalized ensemble averaged electric field correlation functions (obtained from the intensity correlation functions according to the method described in Chapter 2). Sample data obtained from both swollen and collapsed gels are plotted. Several observations can be made. The correlation functions are quite well fitted by a single exponential plus an offset. The fits are indeed excellent for the swollen gel. They are worse for the collapsed gel, but the single exponential behavior is still recognizable. It is thus justifiable to use the single-exponential function fit to obtain the decay time from the data. This decay time is one to two orders of magnitude slower for the collapsed gel. In both cases it is slower close to the transition than away from it.

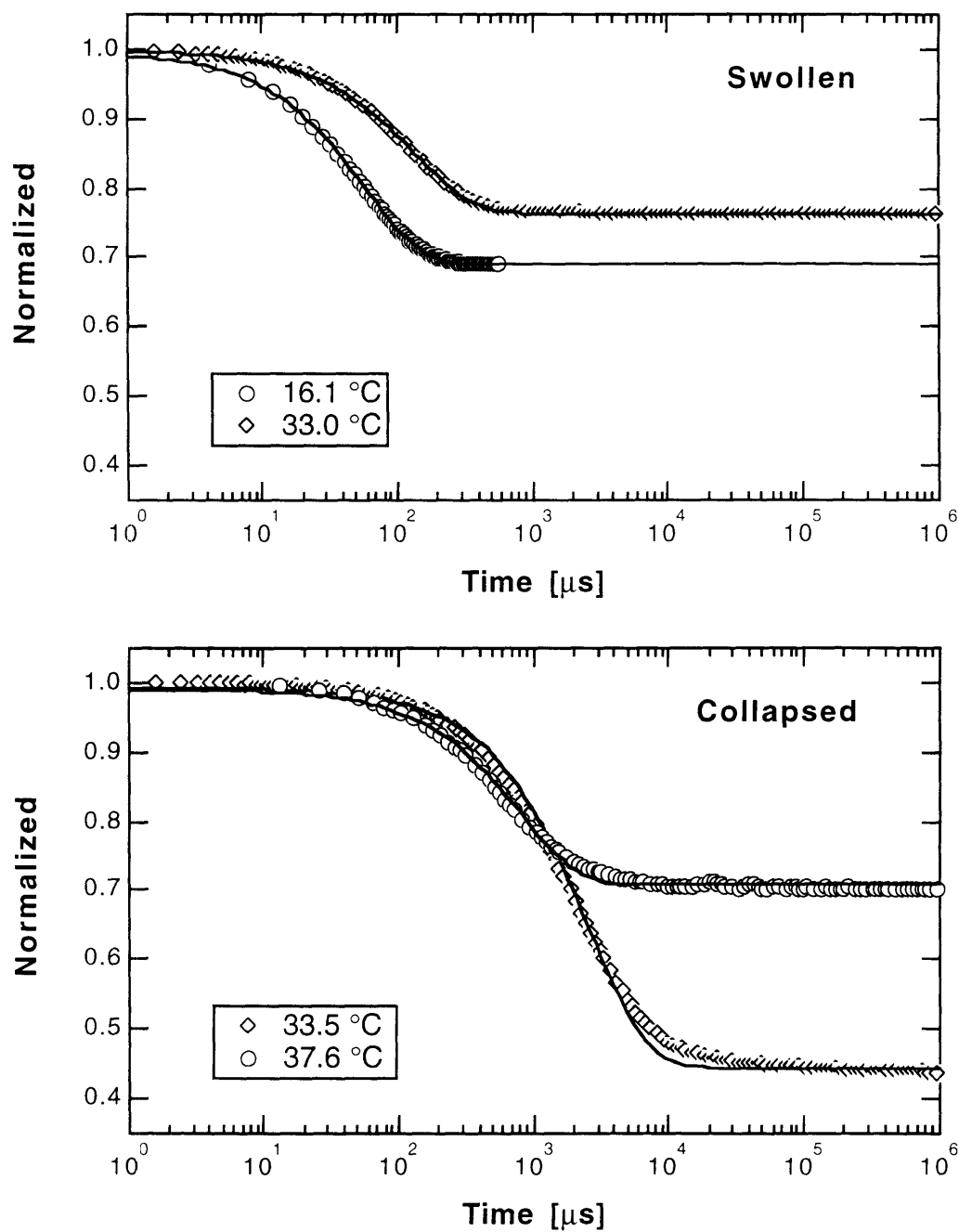


Fig. 4 Normalized electric field correlation function for swollen (upper graph) and collapsed (lower graph) NIPA gel. Two curves are plotted in each case. One is far from the transition point (circles) while the other is near (diamonds). Single exponential fits are also plotted. Notice that in case of the swollen gel the fits are very good, while for collapsed gel they are poorer.

5.3.3 Light Scattering Results

The three parameters obtained from the light scattering data – the decay time, dynamic, and static intensities – are presented in Figure 5. The existence of the phase transition is evident from these plots. There is a jump of at least an order of magnitude in the decay time and the static intensity. Moreover, all the parameters seem to diverge near the transition point. The "equilibrium" values (away from the transition) also appear very different. Figure 6 shows the plots of some of the ratios of these parameters. The ratio of static to dynamic intensity is important because it relates the divergence of the static fluctuations to that of the collective diffusion modes. The ratio of decay time to dynamic intensity is interesting because it is related to the network-solvent friction. Both of them show a marked discontinuity at the transition, but there is no hint of any divergence. This is especially evident in case of the static/dynamic intensity ratio. There are two regimes – one below and one above the transition. In both cases the ratio changes almost linearly with temperature, but they do not match each other at the transition. There are some points exactly at the transition temperature where the ratio appears to diverge. They occur only at the transition, so their abnormal value can be explained by the fact that the gel was not equilibrated. The rate of relaxation is, in fact, related to the decay time obtained from the scattering (Figure 5), and that decay time increases rapidly near the transition point.

The intensity ratio is a "good" parameter, in the sense that it does not depend on the absolute intensity (and thus on the apparatus). One would then expect the gels from batch A and B to match exactly. It is interesting to observe that the match is not quite perfect. There are three points from a collapsed gel of Batch B, which fall below the line of Batch A. Thus the gel from Batch A has a slightly higher proportion of the static intensity.

5.4 DISCUSSION

5.4.1 Shape of the Correlation Function

As presented in Figure 4, the ensemble averaged electric field correlation function is very well fitted by a model based on the collective diffusion (single exponential) plus a nonergodic static component (a constant offset). The validity of the model is thus further

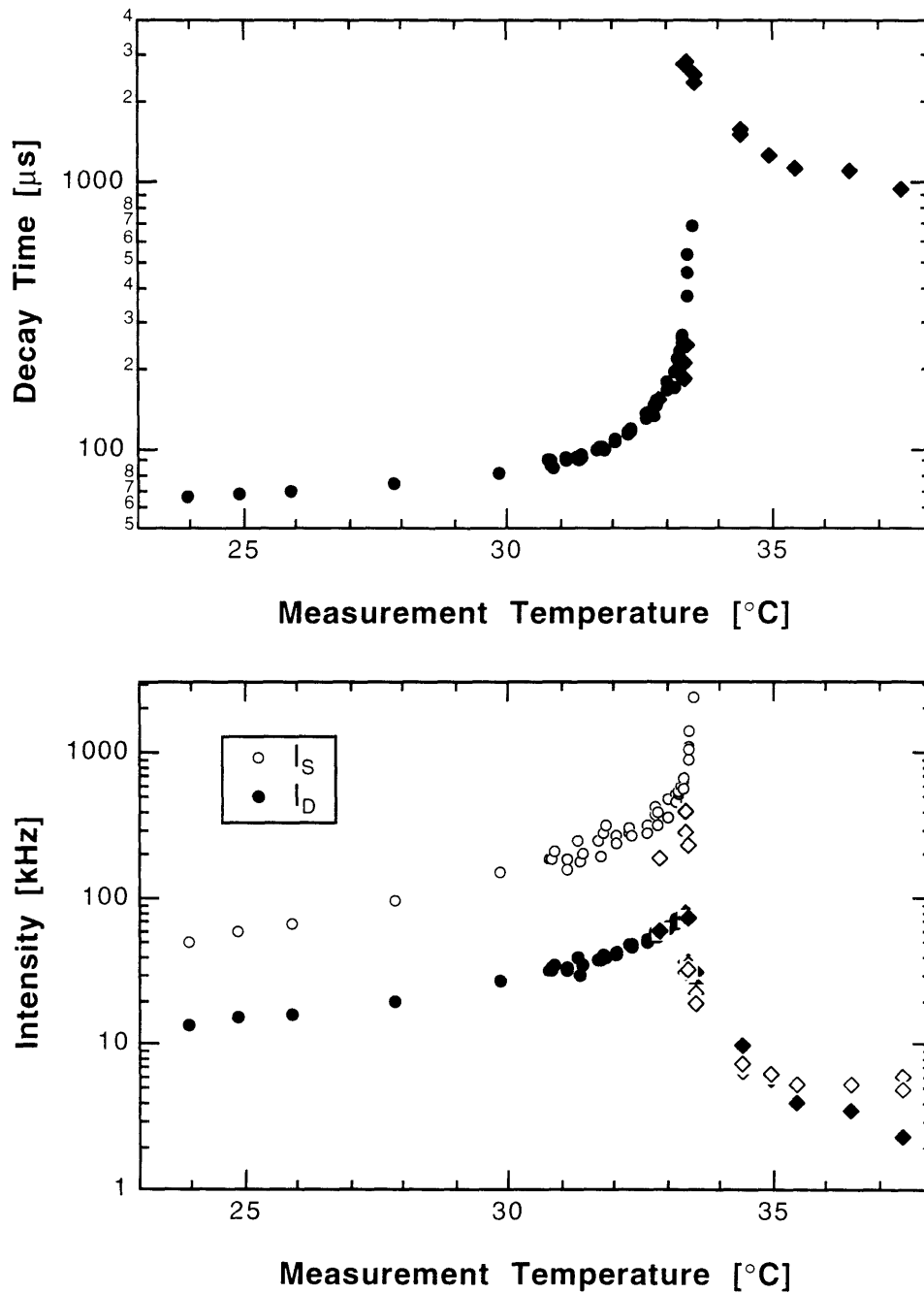


Fig. 5 Light scattering data for NIPA gel near the phase transition. Upper graph shows the decay time. Lower graph has both the dynamic (black) and the static (white) components of the scattered intensity. Here and in the subsequent graphs circles and diamonds refer to two separate sets of data (measured for two different gels prepared in the same way).

confirmed. This result seems to be almost independent of temperature, at least for the swollen gel. It was mentioned before that the collapsed gel's correlation function is more markedly non-single-exponential. This can be explained by the fact that the concentration of the gel is much higher in this case than when the gel fills the micropipette (9.26 times higher, to be exact). Therefore the entanglements have a more profound effect, making the effective crosslinking density dependent on the local density (which fluctuates dynamically). This introduces a non-linearity which could manifest itself in relaxation modes more complex than a single exponential.

The fact that the entanglements play an important role can be also inferred from the dependence of the gel transparency on the speed of transition. As mentioned before, the major obstacle in performing scattering measurements on the collapsed NIPA was that ordinarily collapsed NIPA becomes permanently opaque. Only when the transition is approached extremely slowly does the gel collapse into a transparent form. A possible explanation uses the well-known fact of a microphase separation (10), where during the transition the coexistence of phases occurs first on a microscopic level, with coexistence of separate microdomains of swollen and collapsed gel (i.e., the local concentration fluctuations are amplified). If the volume transition occurs quickly the chains do not have the time to relax. They become permanently entangled. Thus the gel remains opaque due to continuing existence of large concentration fluctuations. When, on the other hand, the gel is allowed to collapse slowly, the chains have the opportunity to disentangle before the global collapse freezes their configuration. Thus the gel becomes clear again.

Another interesting aspect of this problem can be observed from figures 5 (bottom) and 6 (top). Both the static intensity (Figure 5) and the static/dynamic intensity ratio (Figure 6) are much lower for the collapsed gel than for the swollen one. This might be explained by the fact that at the higher concentration the distribution of chains in space has to be more uniform than at lower concentration. Since the static intensity depends on the non-uniformity of the "equilibrium distribution" of the chains, it is natural that it should be lower when the chains are arranged more uniformly.

Finally, another aspect of Fig 6 (top) is worth mentioning. The static/dynamic ratio seems to depend only weakly on temperature, even as both static and dynamic intensities themselves diverge. The divergence of the dynamic intensity can be understood in terms of the vanishing of bulk modulus as the spinodal line is approached. Chapter 3 gave an explanation for the divergence of the static part. The frozen inhomogeneities were argued to cause the blurring of the isobars in the gel phase

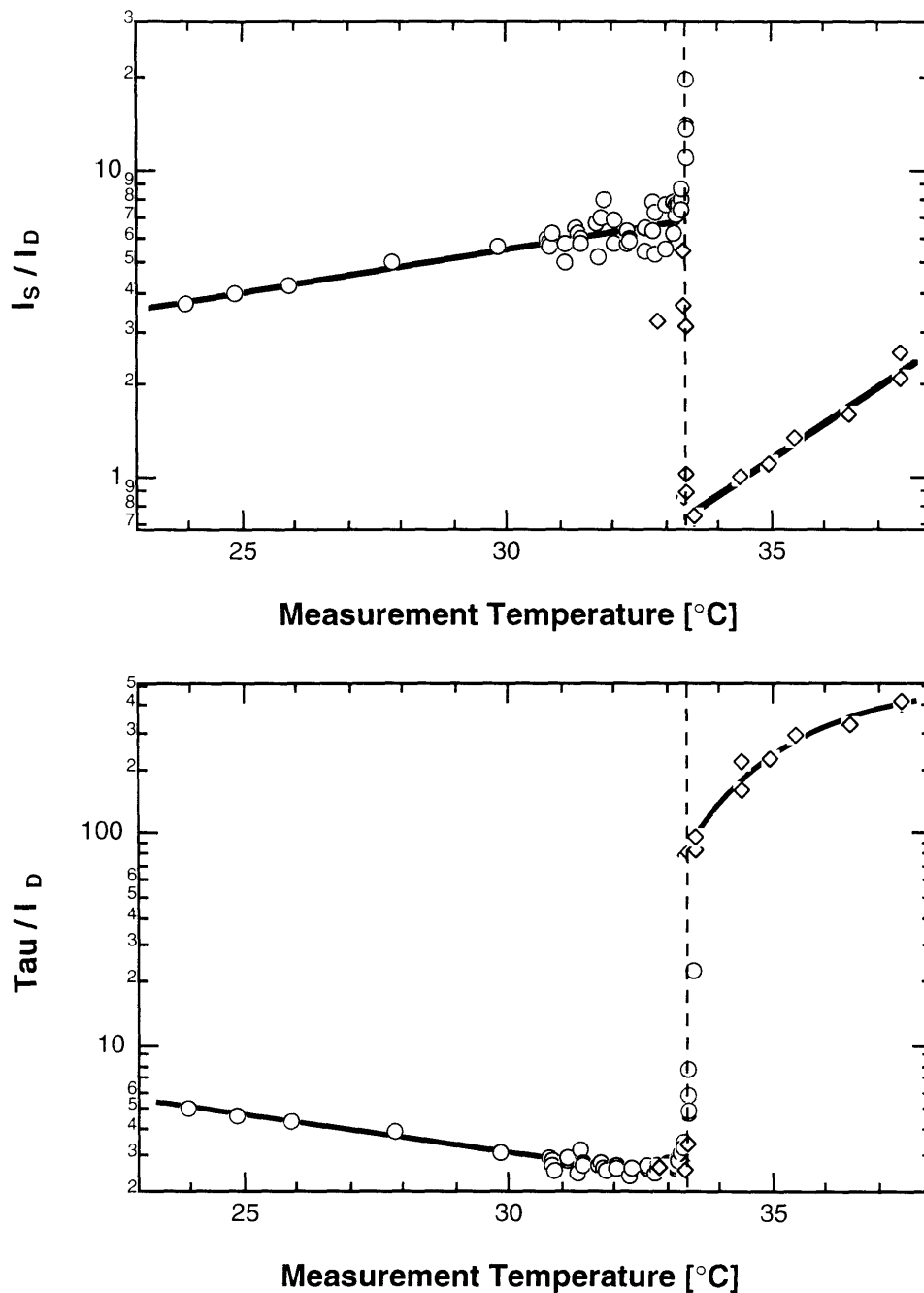


Fig. 6 Discontinuous transitions in various ratios. Top graph shows the static over dynamic intensity ratio. There are clearly two regimes – below and above the transition (marked by dashed line). The dispersion at the transition is probably due to transition kinetics (microphase separation). The bottom graph shows the ratio of decay time to dynamic intensity (proportional to network-solvent friction)

diagram. This blurring diverges as the temperature approaches the spinodal line. The denser regions become denser and the originally dilute regions – more dilute. This gives rise to larger contrast in the refractive index fluctuations and consequently leads to stronger static scattering. The fact that the ratio of the intensities varies only slightly indicates that a single mechanism (prompted by the approach to the spinodal line) is responsible for both divergences. This lends further credibility to the theory outlined in Chapter 3 and summarized above.

5.4.2 Near-Critical Behavior

All three light scattering parameters – decay time, static and dynamic intensities – appear to diverge near the transition temperature (Figure 5). It is, however, evident from that figure that they do not diverge AT the transition. This can be termed near-critical behavior, and merits some investigation (if this was critical behavior, the parameters would diverge exactly at the same point).

It appears, as illustrated in Figure 7, that the parameters of the swollen gel diverge at a temperature higher than the transition, while those of the collapsed gel – below the transition. Figure 7 shows the fits of a power-law function of the form $A \cdot |T - T_c|^{-\delta} + B$ (with T_c , δ , A and B as fit parameters) to the scattering data. Some points lying very close to the transition were excluded since the gel was probably not completely equilibrated (as mentioned previously). For the decay time (Figure 6 top) the value of δ thus obtained was about 1.06 both above and below the transition. For the dynamic intensity (Figure 6 bottom) it was hard to obtain any meaningful value, since the fit results were extremely dependent on the inclusion of points near the transition. However, it is clear that the exponent is negative (δ positive) also in this case.

Figure 8 presents the inverse of the dynamic intensity. Thus δ was arbitrarily chosen to be 1 in this figure, but the data show this to be a reasonable choice. The top graph shows the expanded view of the plot, whereas the bottom one focuses on the immediate vicinity of the transition. In this figure the lines are extrapolated to intersect the horizontal axis (infinite intensity). This figure shows all the essential features – a discontinuous jump at the transition, and divergence at two temperatures above and below the transition.

It was briefly mentioned above that the intensities diverge at the spinodal line. The spinodal line is a place where the isobar is horizontal, i.e., the derivative with respect

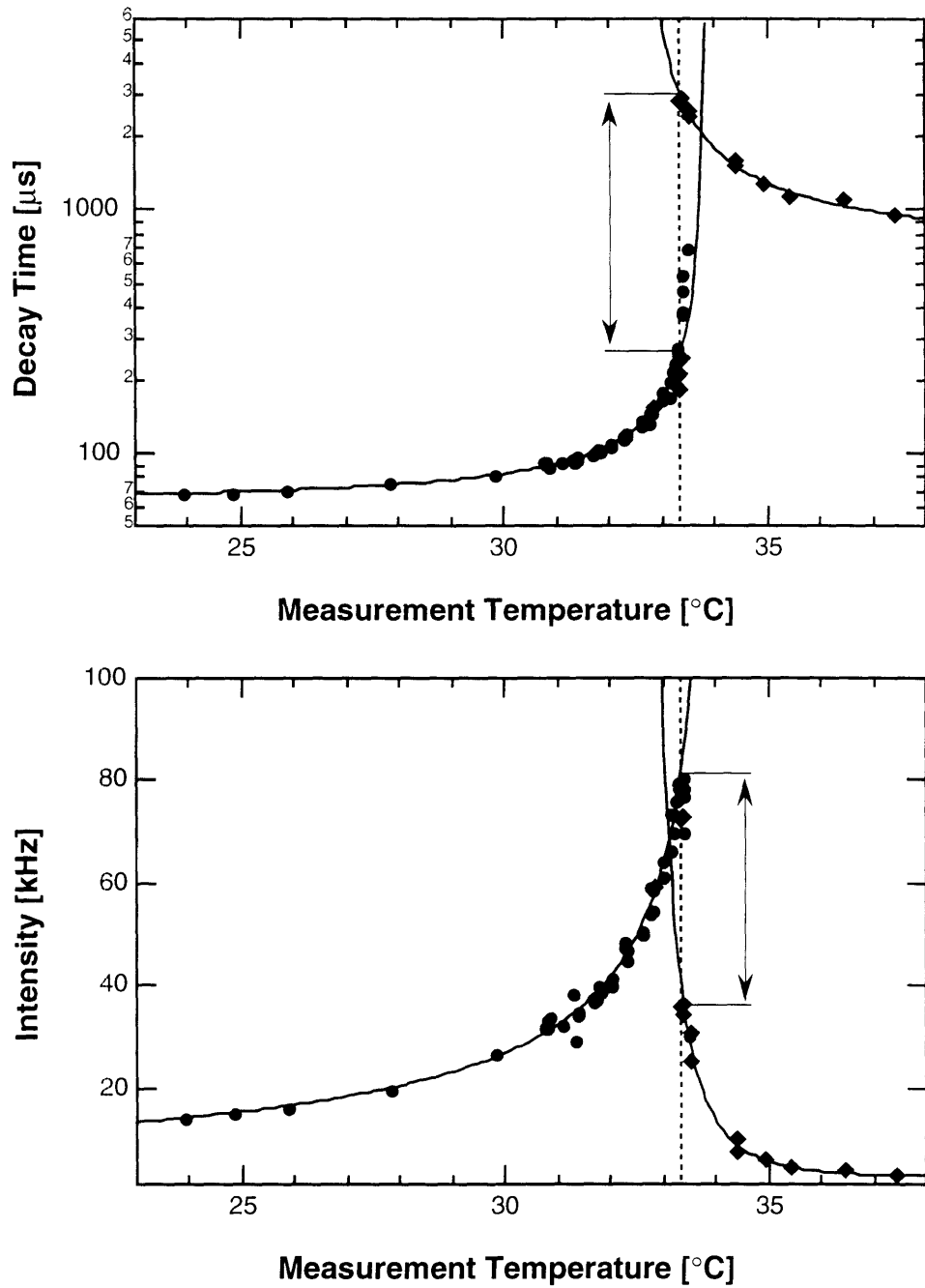


Fig. 7 Demonstration of the near-critical behavior. Both the decay time (upper graph) and the dynamic intensity (lower graph) show a power-law like behavior near the transition point (marked by the dashed line). However, a discontinuous "jump" (indicated by the arrow) occurs before the singularity can be reached. The solid lines are fits to a power law function.

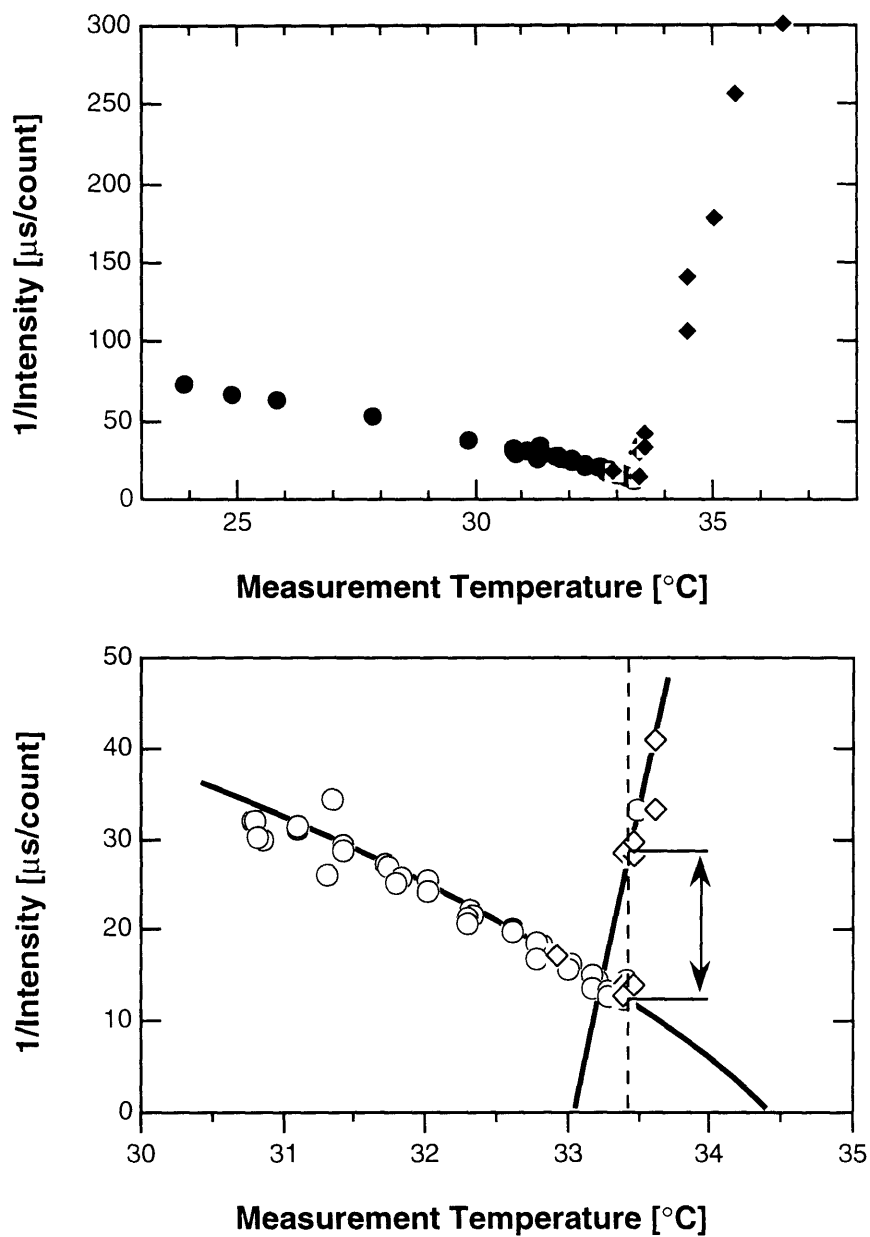


Fig. 8 Inverse dynamic intensity versus temperature of measurement. Lower figure shows details near the phase transition (occurring at the dashed line). The heavy lines extrapolate to infinite intensity. It is evident that these infinity values do not coincide with the phase transition

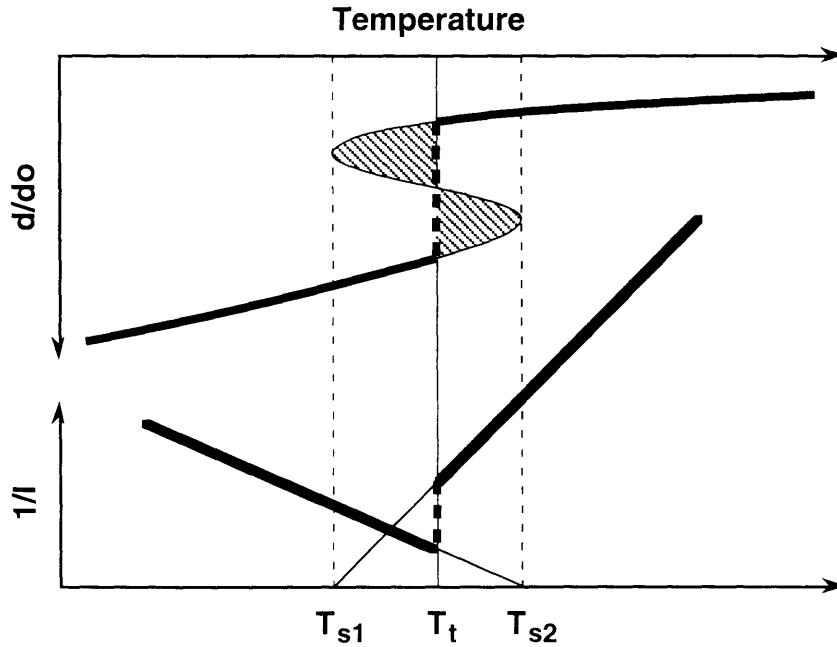


Fig. 9 Qualitative explanation for different divergence temperatures in ascending and descending approach to the transition point. The top curve shows an isobar together with the metastable and unstable regions (shaded). The transition point (marked by a thin vertical line) is determined by the Maxwell construction (the shaded area to the right must equal the shaded area to the left). The dashed lines represent the spinodal points (where the bulk modulus vanishes). The lower curve represents the inverse dynamic intensity (but it could be any other relevant quantity). The divergence points correspond to the spinodal temperatures T_{s1} and T_{s2} .

to the concentration (or d/d_0) vanishes. The bulk modulus is defined as:

$$K = \phi \left(\frac{\partial \Pi}{\partial \phi} \right)_T$$

where Π is the osmotic pressure, and ϕ the network concentration. Thus the bulk modulus vanishes, by definition, at the spinodal line.

Figure 9 uses this concept to illustrate the different points of divergence for the upper and lower approach to the critical point. When the isobar is followed below the

transition temperature (T_t) the measured parameters tend towards divergence at the upper spinodal point (T_{s2}). That point is never reached, however, since the discontinuous transition occurs before the gel gets there. Analogous situation takes place above the transition point. The isobar tends to the lower spinodal point (T_{s1}), which, again, is never reached, because of the transition. Since the slopes of the curves are different, they do not intersect each other at the transition, so there is a discontinuous jump at T_t .

The complication is, of course, that below the transition we don't follow an isobar, but an isochore, so the osmotic pressure is not zero. Apparently, though, this does not affect the behavior very significantly.

5.4.3 Network-Solvent Friction

Figure 6 (bottom) presented the temperature dependence of the ratio of the decay time to the dynamic intensity. As it was mentioned, this ratio is related to the network-solvent friction. This shall be examined now more carefully. As explained in Chapter 2, the collective diffusion model leads to the following electric field autocorrelation function:

$$\langle E(\mathbf{q}, t) E(\mathbf{q}, 0) \rangle \propto \left(\frac{\partial \varepsilon}{\partial \phi} \right)_T^2 \phi^2 \frac{k_B T}{K + \frac{4}{3} \mu} \exp \left[- \frac{(K + \frac{4}{3} \mu) q^2 t}{f} \right]$$

where K and μ are the bulk and osmotic moduli, f the network-solvent friction, \mathbf{q} is the scattering vector, and ε the dielectric constant of the medium. The proportionality constant depends only on the apparatus and the scattering geometry (which is fixed). Thus we may identify:

$$I_D \propto \left(\frac{\partial \varepsilon}{\partial \phi} \right)_T^2 \phi^2 \frac{k_B T}{K + \frac{4}{3} \mu}$$

$$\tau = \frac{f}{(K + \frac{4}{3} \mu) q^2}$$

Therefore the ratio is

$$\tau / I_D \propto f \frac{(d / d_0)^6}{k_B T (\partial \varepsilon / \partial \phi)_T^2}$$

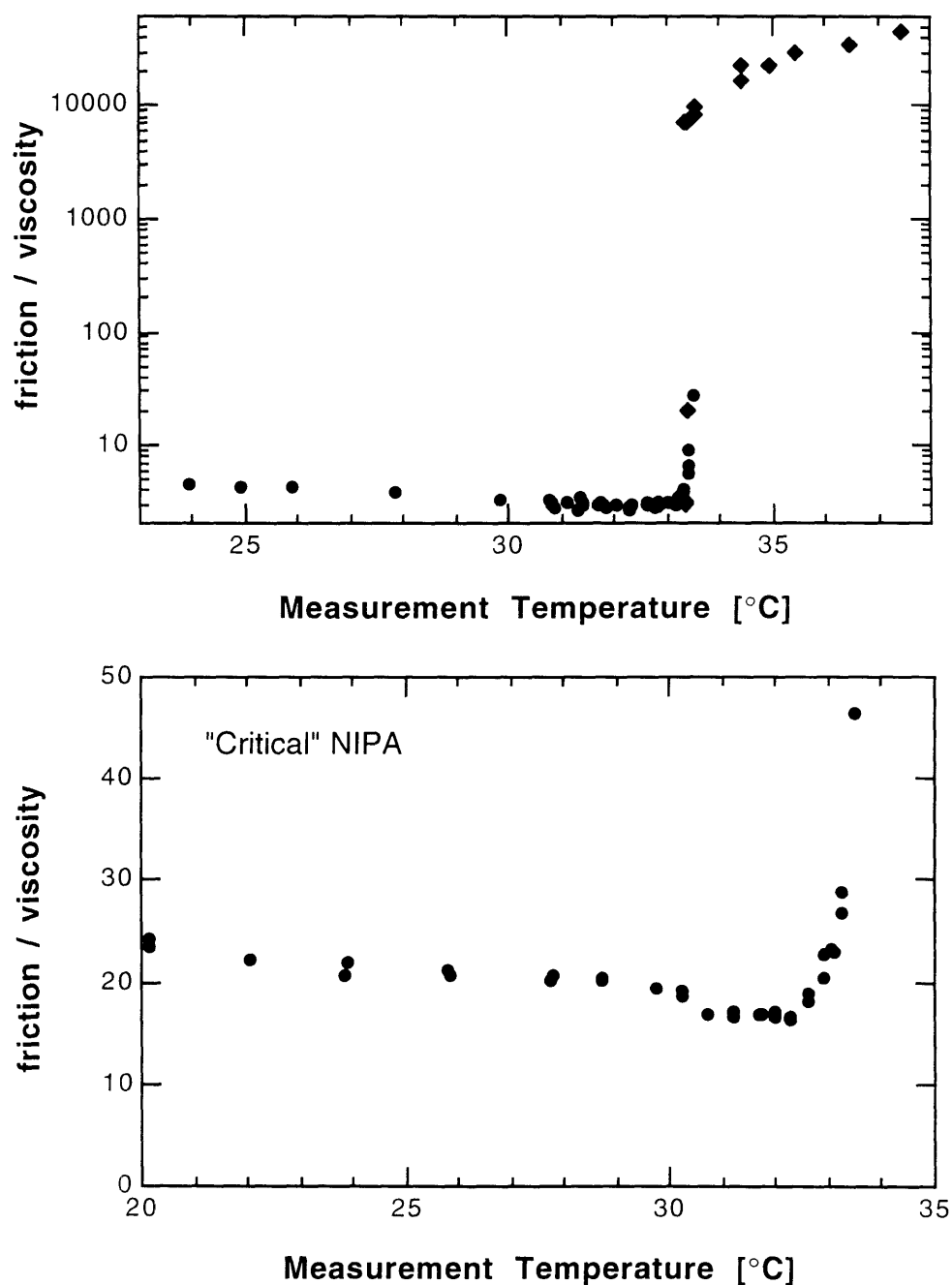


Fig. 10 Friction coefficient calculated from the τ/l_D ratio (as explained in the text). The friction increases tremendously (3 orders of magnitude) at the transition. There is no sign of the friction vanishing at the transition (contrary to (8)), neither in the top nor in the bottom graph, which shows analogous data for a "critical" NIPA gel – a gel whose isobar passes through the critical point.

The friction coefficient f can be assumed to be directly proportional to the viscosity of the solvent (which in turn is temperature-dependent). One can approximate further by making an assumption that $(\partial\varepsilon / \partial\phi)_T$ is a constant, which is justified by the fact that $\varepsilon=n^2$ (n being the index of refraction), and the index of refraction doesn't change significantly with the concentration. Then one can recover the viscosity-independent friction coefficient from the scattering data:

$$f_o = f / \eta(T) \propto \frac{T}{\eta(T)(d / d_o)^6} \left(\frac{\tau}{I_D} \right)$$

Figure 10 (top) shows the result of this transformation. It is clear that the friction coefficient increases drastically (by several orders of magnitude). This is, in fact, what one would expect to happen when the concentration increases. As the network gets "tighter" the flow of solvent is much more hampered than when the network is "loose". The same argument can be used to explain the fact that the friction decreases as we approach the transition from either side. Using the reasoning from Chapter 3, the density fluctuations increase as the spinodal line is approached. Therefore the solvent can flow more effectively through the less dense regions. This effect seems to be much more pronounced in case of the collapsed gel, presumably because any local decrease in concentration is likely to have a relatively bigger effect than in the case of the swollen gel when the friction is not that high to begin with.

What is conspicuously missing from Figure 10 is any hint of critical divergence. To make the case even stronger, the bottom graph of Figure 10 shows the analogous data for a "critical" gel – a gel prepared according to a different recipe, where the increase of the cross-linker concentration makes the transition occur at (or near) the critical point. All other experimental details remain the same. Even in this case, as the transition is approached, there is no critical vanishing of the friction coefficient. This is in direct contradiction with the data obtained by Tokita et al (8). In that work the coefficient of friction in a "critical" NIPA gel is determined through a macroscopic measurement of a water flow rate through a gel as the temperature is varied. The authors observe that this macroscopic friction coefficient vanishes as the temperature approaches the critical point.

The discrepancy between the light scattering and mechanical measurement data can be explained as follows. In case of the mechanical measurement the flow of water is determined by "the path of least resistance" through the gel. This is similar to the problem of percolation – one needs enough dilute domains that the two edges of the gel are connected by low-resistance path. Thus the mechanically determined friction

coefficient measures the largest openings in the network due to critical density fluctuations. The light scattering, on the other hand, measures the average friction coefficient – since both dense and dilute domains contribute to scattering (one would, in fact, expect the dense domains to contribute more significantly). Hence, at the length scale of the scattering vector (ca. 70nm), the large scale fluctuations, which cause the percolating path through the gel, do not affect much the light scattering results.

CONCLUSIONS

A discontinuous temperature-induced transition in NIPA gel was studied using light scattering. The scattering from a collapsed gel was investigated for the first time. The results of these studies confirm a number of results mentioned earlier in this thesis.

The shape of the correlation function, as well as the temperature dependence of the ratio of the static to dynamic intensities support the model that contributes the dynamic portion to the collective diffusion and traces the static intensity to scattering from the average positions.

The vanishing of the bulk modulus at the spinodal line is useful in explaining the near-critical behavior in the light scattering parameters near the transition point.

The network-solvent friction coefficient obtained by light scattering is found to behave very differently from the friction coefficient measured by a macroscopic liquid flow. This sheds further light on the nature of the macroscopic friction coefficient.

FURTHER RESEARCH

A number of further experiments can be performed. First, many discontinuous phase transitions in gels exhibit a hysteresis – they collapse at a different temperature than they swell. It would be instructive to perform such a measurement on the NIPA gel described in this section. The only problem is the time involved in such experiments. The d/d_0 ratio can be determined quickly without much attention being paid to the internal structure of the gel. However, as was seen throughout this chapter, the relaxation of the internal configuration involves a significant amount of time. Nevertheless, such experiments would shed more light on the near-critical divergence of the light scattering parameters, by determining whether the divergences yield the same temperatures on the two branches of the hysteresis curve (confirming that these are the spinodal points).

Furthermore, one could perform the experiments described in this chapter by letting the gel follow an isobar (i.e., by allowing it to swell freely). This would resolve any doubts whether any of the effects described may be due to the isochoric approach. Also, the freely swollen gel is not subject to unidirectional stress, which, according to the literature, affects the scattering along different directions.

Another series of experiments might involve a gel of different composition, which follows the critical isobar. Experience shows that the static light scattering is much stronger for such a gel, making it more difficult to perform the measurements. However, in such a case, everything should diverge at one temperature (the critical temperature).

Finally, one could measure the friction coefficient by doing light scattering at different angles (different values of the scattering vector q). This information should be interesting, because it might allow for reconciliation of the mechanically measured friction coefficient ($q=0$) with the one measured by light scattering ($q>0$). This, however, would require a different scattering setup, capable of ensemble averaging (moving) the sample, and changing the scattering angle.

REFERENCES

- [1] Schild, H.G.: *Prog. Polym. Sci.*, **17**, 163-249 (1992).
- [2] Hirokawa, Y. and Tanaka, T.: *J. Chem. Phys.*, **81**, 6379 (1984).
- [3] Hirotsu, S., Hirokawa, Y. and Tanaka, T.: *J. Chem. Phys.*, **87**, 1392 (1987).
- [4] Matsuo, E.S.: Ph.D. Thesis, M.I.T. (1987)
- [5] Li, Y.: Ph.D. Thesis, M.I.T. (1989).
- [6] Shibayama, M., Tanaka, T. and Han, C.C.: *J. Chem. Phys.*, **97**, 6829 (1992).
- [7] Yu, X.H., Ph.D. Thesis
- [8] Tokita, M. and Tanaka, T.: *Science*, **253**, 1121 (1991).
- [9] Taylor, L.D. and Cerankowski, L.D.: *J. Polym. Sci. Pt. A: Polym. Chem.*, **13**, 2551 (1975).
- [10] Dusek, K. in *Polymer Networks*, eds. A.J. Chompff and S. Newman, Plenum, New York, (1971).

CHAPTER 6

LIGHT SCATTERING FROM A POLYELECTROLYTE GEL

Previous chapters dealt with NIPA gels which were neutral. The gels would collapse at high temperature due to the hydrophobic interaction between NIPA units. A slightly more complicated system can be prepared, in which some of the units are charged. The macroscopic behavior of the gel is not qualitatively affected – the transition temperature and the equilibrium diameter are increased, but that is the extent of the macroscopic change. However, as this chapter will reveal, there is a significant change at the microscopic level, which can be probed by light scattering.

Several results are presented. The light scattering data is compared to Small Angle Neutron Scattering (SANS) results available for the same gel in literature. A qualitative agreement is found. In addition a novel dynamic behavior is reported where the correlation function decays like power law with a temperature-dependent exponent.

6.1 INTRODUCTION

This chapter deals with scattering from a NIPA+Acrylic Acid (AAc) copolymer gel. Figure 1 shows the chemical structure of the two co-monomers. The bulk of the gel is NIPA, which is neutral. A small amount of AAc is added, which can dissociate to provide an effective network charge. An extensive study of the swelling properties of similar gels (NIPA+sodium acrylate – an AAc derivative, which also dissociates to AAc⁻)

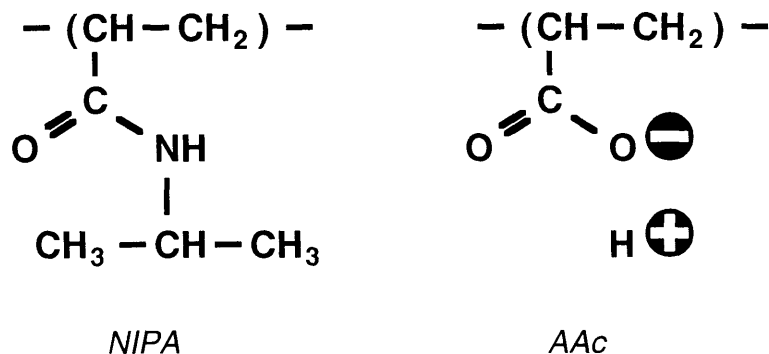


Fig. 1 Chemical structure of NIPA and acrylic acid (AAc) units. The NIPA units are neutral (and hydrophobic), while the AAc units provide a network charge.

was done by Hirotsu et al. (1), following a theory developed by Tanaka (2). A conceptual model of a polyelectrolyte is presented in Figure 2. In contrast to the neutral gels discussed before, the network is now charged (negatively in this case). The effect of charge on the phase transition is shown in Figure 3. To maintain electroneutrality, counter ions are distributed through the solvent. A naive interpretation would assume that the biggest contribution comes from the Coulombic repulsion of the like charges fixed to the network. It is, however, not very important, because the charges are effectively screened by the ions present in the solution, so the range of the Coulombic repulsion is greatly reduced (Debye screening). An important contribution comes from another source – the counter ion osmotic pressure. These ions cannot leave the network, because this would violate the bulk electroneutrality, thus imposing a stiff energetic penalty. Therefore the counterions behave as an ideal gas confined in a closed volume (the bulk of the gel). They exert a pressure on the "walls" – the gel-solvent boundary thus attempting to swell the gel. The gel osmotic pressure Π is derived rigorously in (1):

$$\begin{aligned} \Pi &= \Pi_{\text{mixing}} + \Pi_{\text{elastic}} + \Pi_{\text{ion}} \\ &= -\frac{NkT}{\nu_1} \left[\phi + \ln(1 - \phi) + \chi\phi^2 \right] + \nu kT \left[\frac{\phi}{2\phi_0} - \left(\frac{\phi}{\phi_0} \right)^{1/3} \right] + \nu f kT \left(\frac{\phi}{\phi_0} \right) \end{aligned}$$

where ϕ is the volume fraction (concentration) of the network (ϕ_0 when the gel was made), χ is the Flory interaction parameter (3), ν_1 the molar volume of the solvent, ν the number of chains per unit volume, and f the charge per chain.

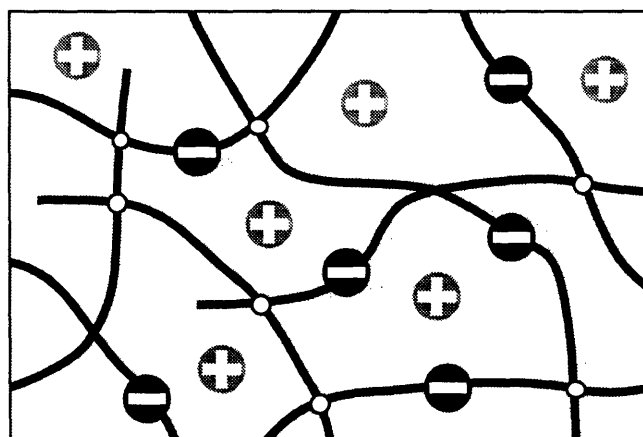


Fig. 2 Conceptual diagram of a polyelectrolyte. Here the negative charges are attached to the network, while the positive ones are the counterions in the solution. The bulk of the gel (network and solvent) remains electroneutral.

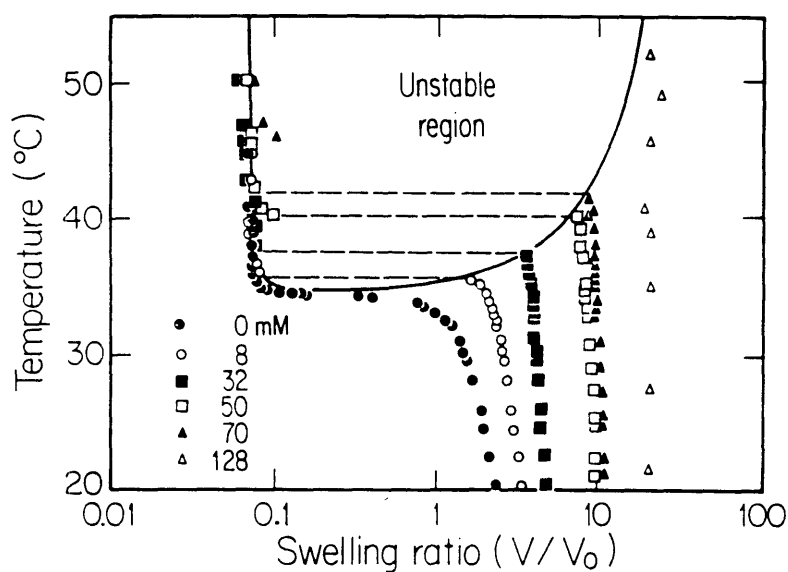


Fig. 3 Coexistence curve of charged NIPA gel determined by measuring the transition points for gels with various degrees of network charge (obtained by varying the molar ratios of NIPA and sodium acrylate). Data reproduced from (1).

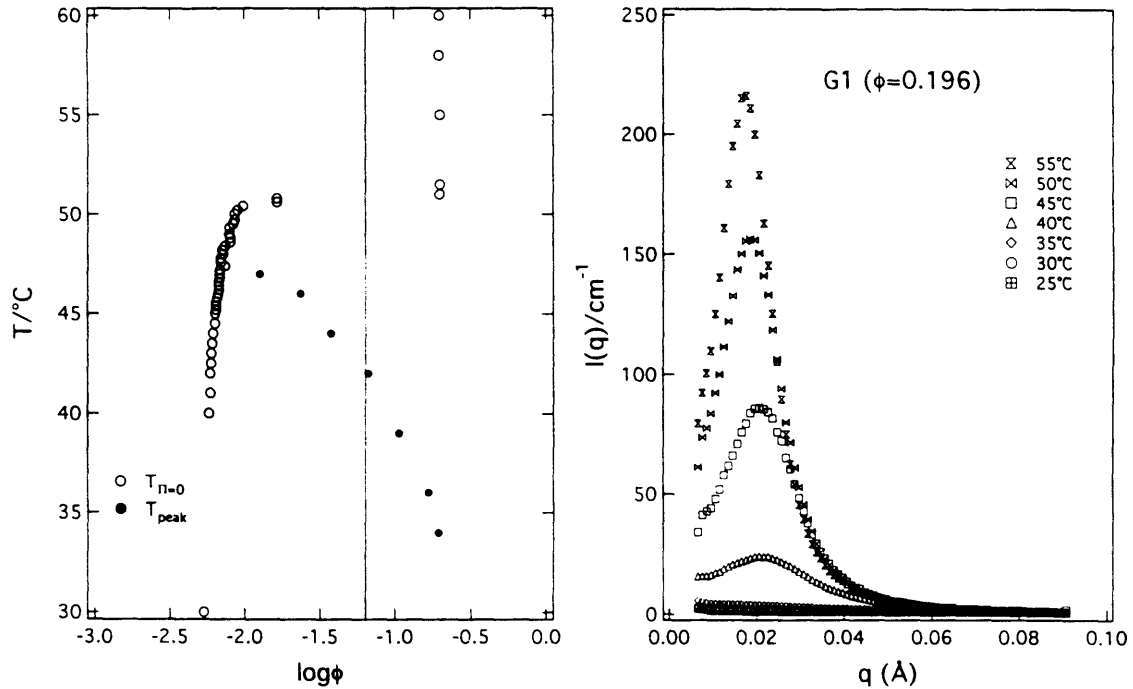


Fig. 4 SANS Data reproduced from (4). The left graph shows the isobar (open circles), and the concentration dependence of the temperature at which a peak appears in the SANS spectrum. The measurements reported in this chapter were carried out along an isochore at $\log\phi=-1.19$. The right graph shows the temperature dependence of SANS profiles for a gel with $\log\phi=-0.71$. The peaks present at high temperatures are evident.

Small Angle Neutron Scattering (SANS) studies of this system were carried out by Shibayama et al. (4). Figure 4 summarizes some of their results that are relevant to this discussion. One observes that the transition temperature is elevated with respect to that of a neutral gel (consistent with Figure 3). Above certain temperature (corresponding to the temperature at which the quality of the solvent for this gel changes from good to poor) a scattering peak is detected in the SANS data. It is due to the formation of gel structure by microphase separation. The onset of this phenomenon is concentration dependent (evident from Figure 4).

6.2 EXPERIMENTS

6.2.1 Sample Preparation

The gel sample used throughout this chapter was formed by free radical copolymerization of 7.462g of N-isopropylacrylamide (Kodak Chemical, purified by recrystallization), 217 μ l Acrylic acid (AAc – purified to remove polymerization inhibitors) and 132.5mg N,N'-methylenebisacrylamide (BIS – crosslinker) in 100ml of deionized water. The resulting molar concentrations of NIPA, AAc, and BIS were 668/32/8.6mM respectively. 43mg of ammonium persulfate (APS – initiator) were also mixed in. Thus prepared pre-gel solution was filtered using a 0.22 μ m filter and degassed in vacuo for 10-15 minutes and cooled in a freezer for 15 minutes. To initiate the gelation 480 μ l of Tetramethylethylenediamine (TEMED – accelerator) were added and the solution transferred into a cold test tube holding some open micropipettes. The temperature of the gelation process was kept at 20°C by immersing the test tube into a circulating heat bath (Lauda model RM 6). After allowing 18 hours for gelation the micropipettes were extracted from the bulk of the gel. All measurements were performed on a sample that has never been taken out of the micropipette in which it was made. Therefore the scattering was performed along an isochore, except for a few points at highest temperatures where the gel was collapsed.

6.2.2 Temperature

Temperature was the independent parameter in this series of experiments. A range from 10°C to 60°C was investigated. The temperature of the sample was stabilized to within 0.01°C using a computer-driven thermoelectric temperature controller (see Introduction). The temperature was changed in small steps, and the measurements at different temperatures were spaced 2.5 hours apart to allow for gel's equilibration. Two sets of data were collected at each temperature.

6.2.3 Light Scattering

The scattered light intensity and the intensity auto-correlation function were determined at an angle of 90° using the microscopic laser light scattering setup described

earlier in this thesis. The sample cell was mounted on a microscope stage, which could be moved perpendicularly to the scattering plane by a stepping motor (see Introduction) to perform the measurements at 50 different locations spaced $5\mu\text{m}$ apart. At each location two auto-correlation functions with different channel widths ($2\mu\text{s}$ and $20\mu\text{s}$ per channel) were collected (70 second each) using a Brookhaven BI-2030AT correlator with 136 linear channels. In order to study the shape of the correlation function, one set of 70 different locations (at 18°C) and one of 600 (at 46°C) were collected using BI-2030AT's multiple-tau mode to obtain four decades of time resolution.

Since the data was gathered over a long time (8 continuous days), a device was added to the scattering apparatus to correct for the drift of the scattering beam (which would result in a loss of intensity). After every scan, a stepping motor would move the fiber focuser laterally back and forth while the intensity was monitored. The sample was also moved back and forth at each focuser position to average over the inhomogeneities. The focuser was then brought to the point of maximum intensity, corresponding to a centered beam.

Because of the sample's nonergodicity the method outlined in Chapter 2 was used to construct the ensemble average. Raw correlation functions from N different locations were summed and normalized forming an approximation $g_N^{(2)}(t)$ to the ensemble average $g_E^{(2)}(t)$. Because of the complexity of the correlation functions, an approach different from the one employed in other chapters was used to analyze the data than. At each temperature the normalized ensemble averaged electric field correlation function $|g_E^{(1)}(t)|$ was obtained from $g_E^{(2)}(t)$ with the help of the Siegert relationship (see Chapter 2 for the exact procedure of correcting for finite N):

$$g_E^{(2)}(t) = 1 + |g_E^{(1)}(t)|^2$$

This $|g_E^{(1)}(t)|$ was then fitted using a functional form of a single exponential plus a power law plus a constant:

$$|g_E^{(1)}(t)| = A e^{-t/\tau} + B(\sqrt{t^2 + t_0^2})^{-d} + C$$

where the square root asymptotically approaches t , while eliminating the singularity at $t=0$. The various contributions to the total intensity could then be read off directly from the fitting parameters:

$$I_{\text{exp}} = A \cdot I_{\text{total}}$$

$$I_{\text{power}} = B t_0^{-d} \cdot I_{\text{total}}$$

$$I_{\text{static}} = C \cdot I_{\text{total}}$$

The decay time is simply τ from the fit.

6.3 RESULTS

6.3.1 Scattering Parameters

Figure 5 shows the shape of the correlation functions at two different temperatures. At low temperatures the correlation function is very well fitted by a single exponential. At high temperatures it is obvious that the single exponential is not a good model. On the other hand, the single exponential plus power law function described above was found empirically to provide an excellent fit to the data (the function showed in the graph does have a singularity at $t=0$, so it does not fit well the first two channels).

The temperature dependence of the fit parameters is shown on Figure 6. Initially the decay time stays almost constant, but takes a sharp turn around 41.5°C . It then seems to reach a minimum around 52°C , and then take another turn around 56°C . These could be artifacts, though, since the decay time is now approaching the lower limit of temporal resolution (the channel width is $20\mu\text{s}$). Also the fraction of dynamic intensity is very small at these temperatures.

The bottom graph of Figure 6 shows even more interesting data. As seen from Figure 5, at low temperatures the correlation function is very much single-exponential like. Therefore the value of the power d obtained at these temperatures is an artifact of an improper fitting procedure. A power law with $d=0.8$ is quickly decaying, so it does not significantly alter the correlation function shape. Above 41.5°C the nature of the correlation function changes. The power law term appears, and the exponent decreases, until it reaches a minimum around the volume transition temperature. It then begins increasing again. These two transition points are even more evident in the other curve of the graph, representing $1/d$. $1/d$ stays at a low constant level below 41.5°C (no power law term present), then increases almost linearly to a maximum at 52°C , after which it begins decreasing again.

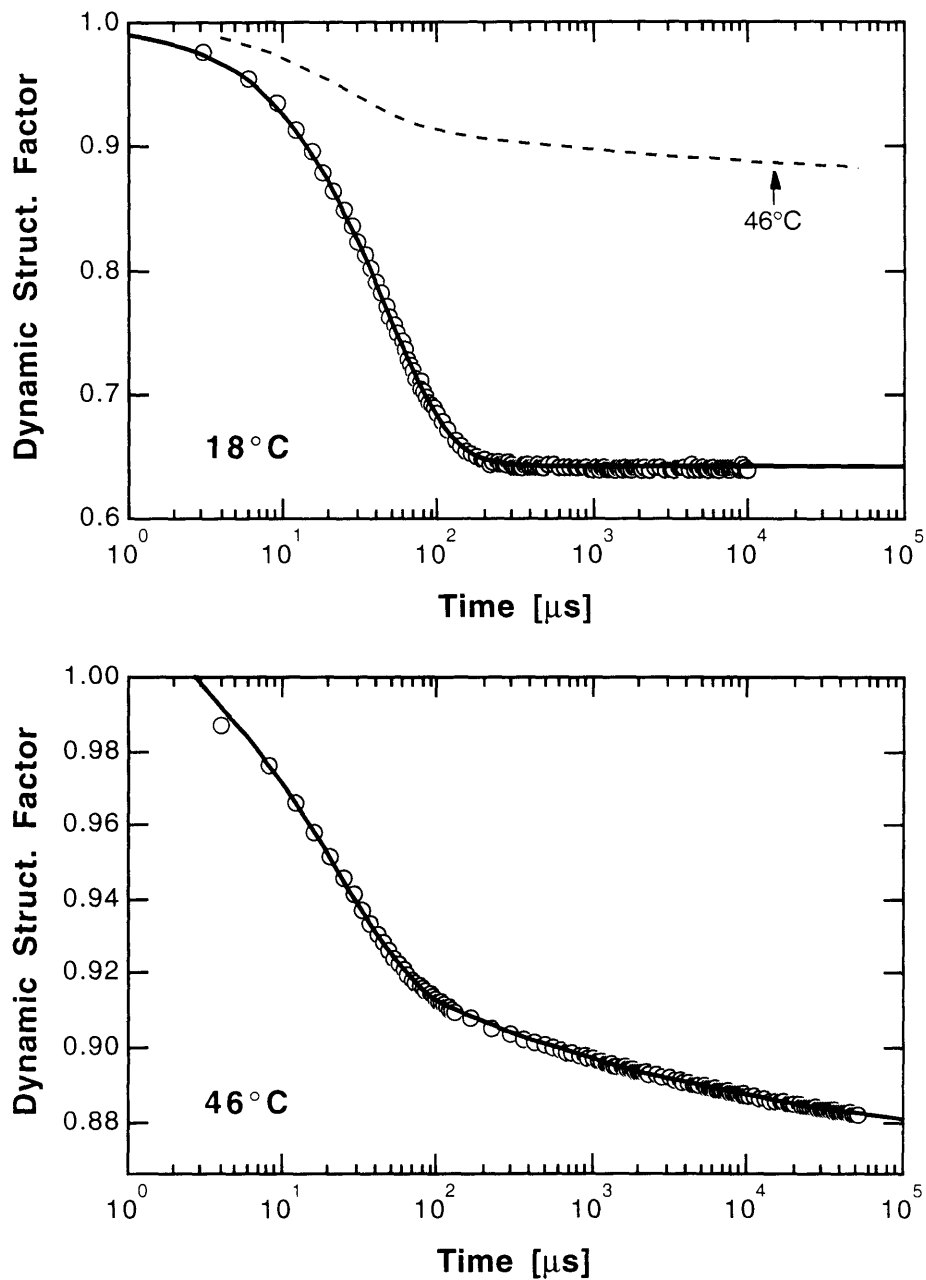


Fig. 5 The shape of the normalized electric field autocorrelation function at different temperatures. The top graph is at 18°C (the dashed line shows the 46°C data). The bottom graph shows an expanded view of the 46°C data. At 18°C the correlation function is well fitted by a single exponential (heavy line). At 46°C the fit used is a sum of a single exponential and a power law (heavy line). The actual parameters are $(.866) + (.098) t^{-.168} + (.056) e^{-t/(26.0)}$. The quality of this fit is very good.

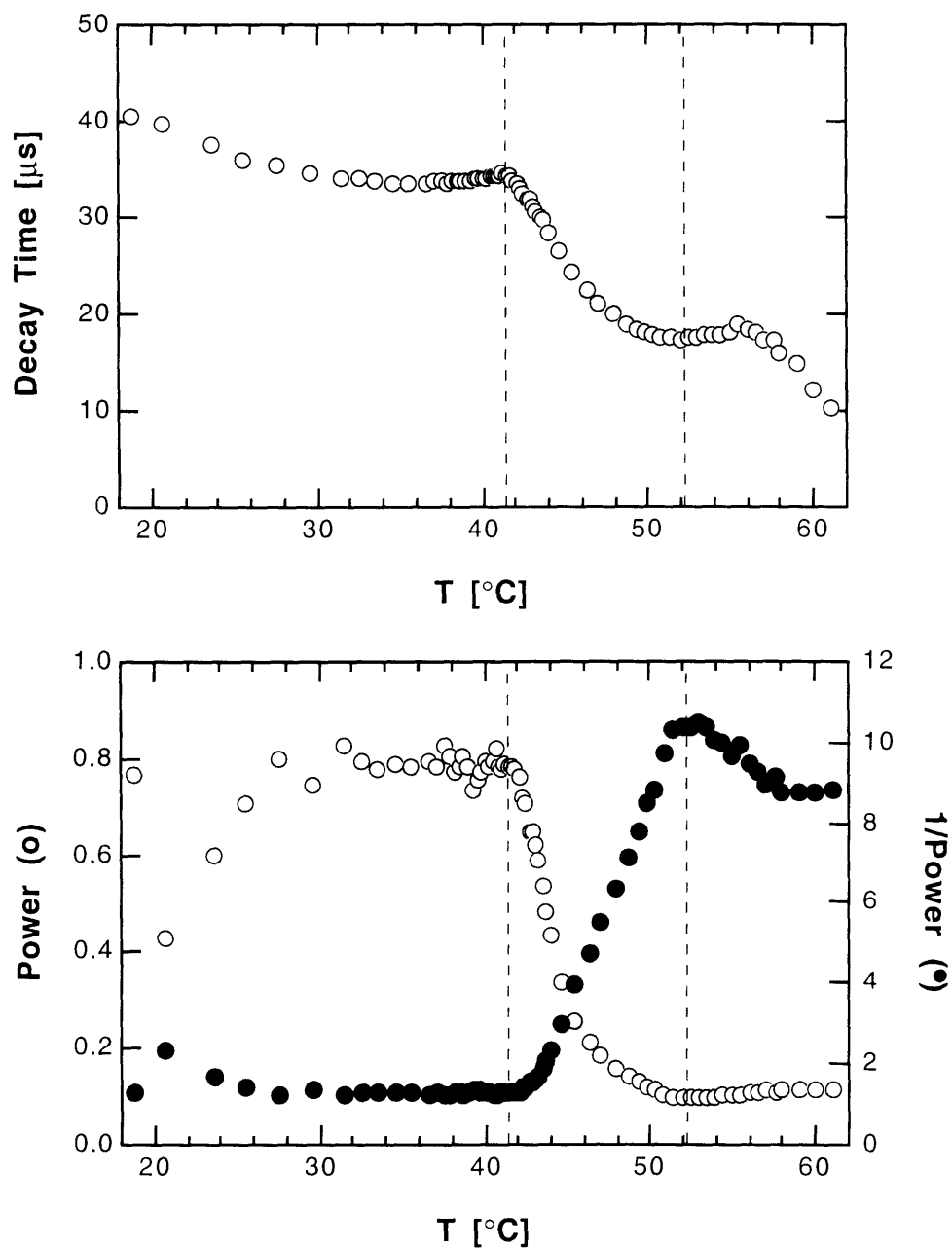


Fig. 6 Temperature dependence of the fit parameters. The fit was single exponential + power law + constant. The top graph shows the decay time from the exponential. The bottom graph shows the power from the power law fit (open circles) and its inverse (black circles). The dashed vertical lines mark two temperatures at which some transition occurs. The higher one corresponds to the volume transition (collapse). At the lower one the shape of the correlation function changes (the power law term appears).

6.3.2 Intensities

The various components of the scattering intensity are plotted on Figure 7. First interesting observation is that nothing very drastic happens at the transition temperatures described above. The static intensity continues to increase with temperature. The exponential part has a mild maximum near the first transition temperature, and then begins to decrease. The power law part follows the static part almost exactly. At high temperatures it dominates the exponential part.

Figure 8 shows the friction coefficient and bulk modulus calculated from the scattering parameters (see Chapter 2 and Chapter 5). Two sets of curves are plotted. One is calculated assuming that only the exponential part should be included in the dynamic intensity (open circles). The other takes dynamic intensity to be the sum of the exponential and power law contributions (black circles). The behavior is different only at high temperatures when the power law part becomes dominant.

6.4 DISCUSSION

The light scattering results of this chapter can be compared with the SANS data obtained by Shibayama et al. (4). At temperatures below the Θ temperature of NIPA in water (the temperature at which the quality of the solvent changes from good to poor), the light scattering from the gel is well described using the theory outlined in Chapter 2. In this regime all the relevant forces are repulsive in nature, so they attempt to swell the gel up to the point at which the rubber elasticity balances the repulsion. As the gel approaches and crosses the Θ point, the polymer-polymer attraction due to the hydrophobic interaction becomes significant. A neutral gel would collapse at this point. However, from the point of view of the counterions and the network charges this confinement would cause a tremendous entropy loss. Therefore they resist the collapse. At some high temperature the attractive interaction finally dominates the repulsion and the gel collapses. What happens in the intermediate regime? Shibayama et al. (4) propose that a "compromise" is reached, where swollen highly charged regions coexist with shrunken neutral parts. Such structure has certain characteristic dimension which is evident in the SANS data. The temperature at which this behavior emerges is dependent on the network concentration. Shibayama's results show that for a concentration

corresponding to the one used in this chapter the transition occurs at around 42°C, coinciding with the emergence of the power law spectrum in the light scattering data at 41.5°C. It appears that these are two aspects of the same phenomenon.

The SANS data looks at a static portrait of the gel's state. An interesting feature of light scattering is that it allows us to observe the dynamics of this process. The dynamics appears to be rather complex, as evidenced by the power law correlation function of Figure 5 (bottom). This is a rather unusual spectrum. The first objection that one may pose is whether the power law is a good description of the data? Perhaps there exists some simpler model that would not require using the power law fit? Or maybe this behavior is only due to the kinetics of some transition? The quality of the fit in Figure 5 (bottom) is a strong evidence that this is a correct description. The consistency of the power d in Figure 6 (bottom) provides another strong argument for this interpretation. As to the temporary nature of this phenomenon, there are two arguments. First, the gel is away from any volume transition, at least at the temperature of 46°C. The second evidence is that the data in Figure 5 (bottom) were collected over a time span of 35 hours, thus one would expect that even if there was some transition, the gel would have enough time to equilibrate. Therefore the power law correlation function is a permanent, rather than transitional feature.

What process within the gel would produce a power law behavior? The power law dependence is characterized by a lack of any characteristic time scale. It corresponds to a fractal distribution of photon arrival times. Such behavior was first described by Mandelbrot (5) as a description of the distribution of errors during telephone transmissions. This, however, does nothing to explain the nature of the process within a gel. Martin (6) did in fact observe a power law correlation function at the threshold of gelation of silica gel. As their pre-gel solution undergoes gelation, the correlation function changes from a single-exponential to single-exponential plus a power law – similar to the case discussed here. The amplitude of the power law becomes less and less significant as the gelation process becomes complete. The authors attribute the power law behavior to a self-similar distribution of fractal clusters of all sizes, from monomers to the infinite cluster. The size-dependent velocity and the screening of the scattered intensity then translate into a power law correlation function in the time space. This interpretation is difficult to adapt to the present case, however. First, the SANS results (4) indicate that the length scales within the gel are well-defined. Second, it is hard to speak of the motion of clusters, since the network is already cross-linked up to the macroscopic scale. Third, the temperature dependence of the power d is difficult to explain in this way.

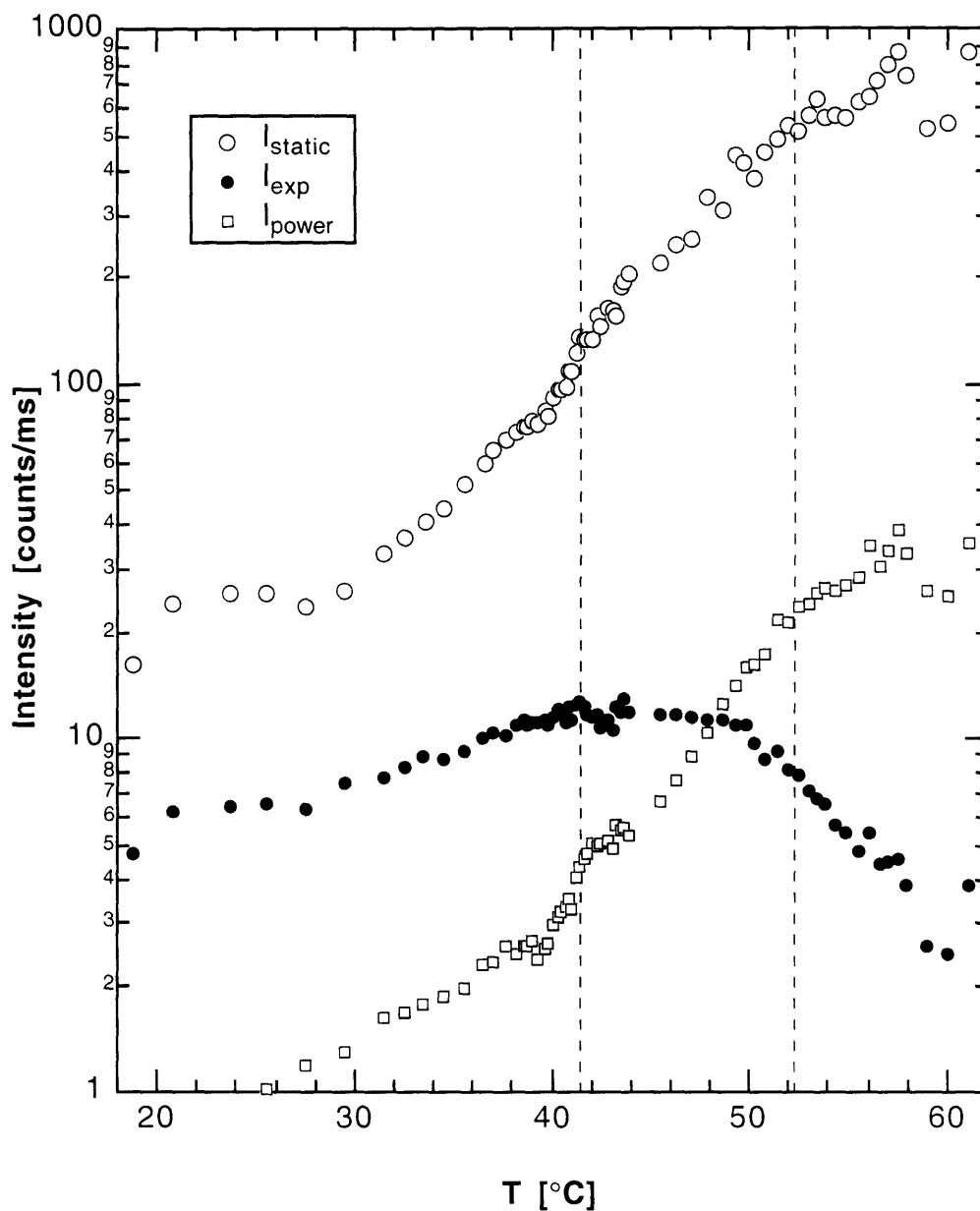


Fig. 7 Scattering intensity as a function of temperature. Contributions of different components are plotted separately. The static intensity is marked by open circles. There are two contributions to the dynamic intensity: the single exponential (black circles) and the power law (squares). The dashed vertical lines correspond to transition points determined from Fig. 6. The intensities are generally not affected by the transitions. The static intensity continues climbing, the exponential has a maximum. The power law intensity follows the static one almost exactly.

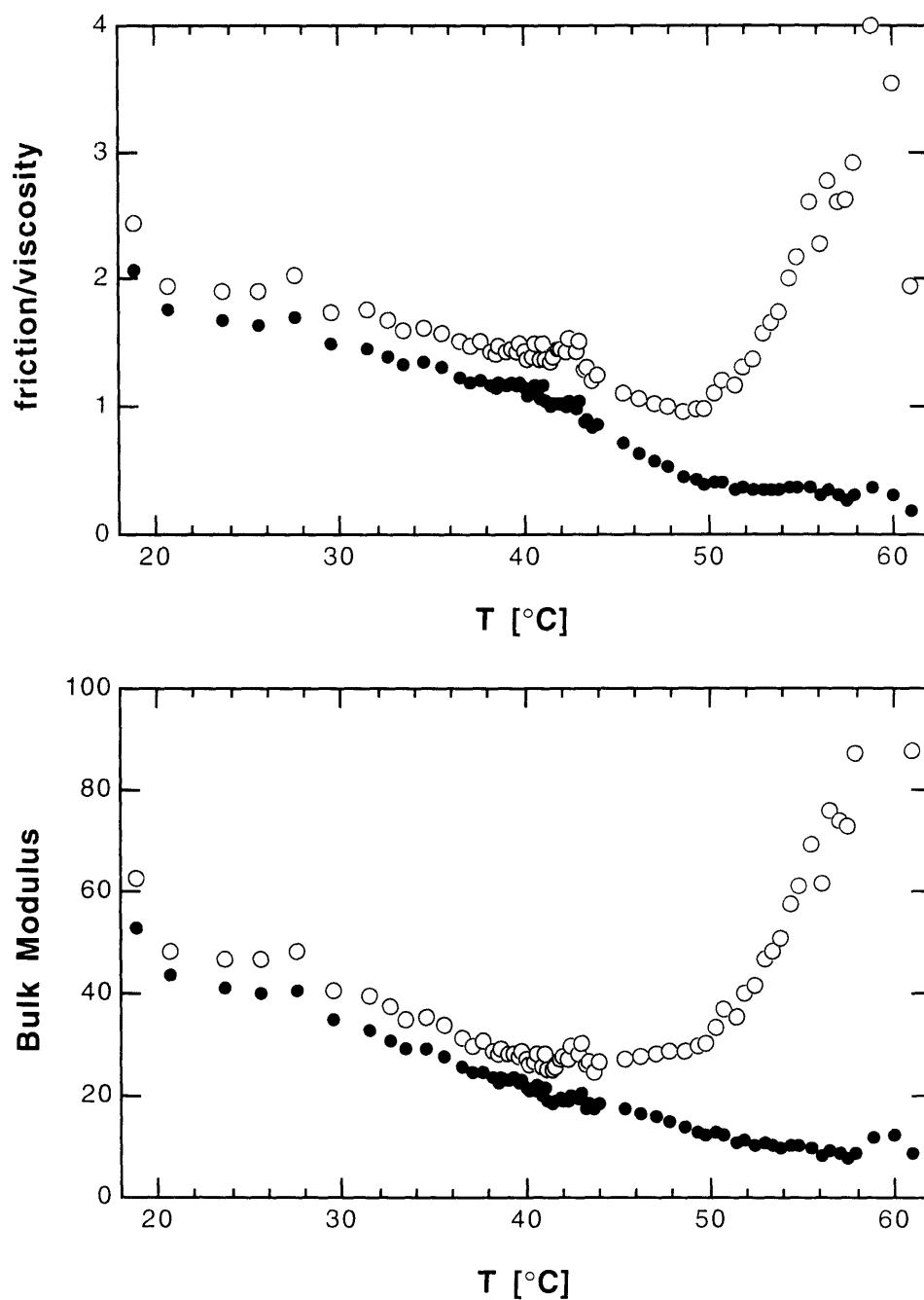


Fig. 8 Temperature dependence of network-solvent friction (calculated from the ratio of decay time to dynamic intensity), and the bulk modulus, (calculated from the dynamic intensity). The dynamic intensity was taken to be either the exponential part only (open circles) or a sum of the exponential and power law parts (everything that fluctuates – black circles).

This temperature dependence of the power d is a very interesting fact in its own right. The usual scaling theories predict the power to have some universal value (cf. (7)). Here d itself is a function of temperature (as evidenced by Figure 6 – bottom)! This corresponds to a tremendous "slowing down" of the system. As mentioned earlier, there is no time scale associated with a power law decay. Let us, for the sake of argument, introduce one artificially. Notice that on a normal-log graph the power law looks like a single exponential. The x -axis is now $x = \ln t$, so $t^{-d} = (e^x)^{-d} = e^{-d \cdot x}$. Thus the "characteristic x " is $1/d$, and the "characteristic time" is $e^{1/d}$. We notice from Figure 6 (bottom) that $1/d$ increases from 1 to 10, thus the "characteristic time" increases by many orders of magnitude!

Figure 7 might provide another clue to the nature of the phenomenon. The power law contribution to the intensity increases at a constant ratio to the static contribution. This could indicate that the same phenomenon is responsible for both effects. The SANS data (Figure 4-right, from (4)) show an increase in the peak intensity with increasing temperature. The location of the peak does not change much, so the associated length scale remains constant. Since the peak is due to the presence of swollen and collapsed microdomains, it is easy to argue that the increased contrast is also responsible for the increase in the static contribution to the light scattering intensity. As the emergence of the domains appears at the same point that the power law behavior, it is reasonable to argue that the latter is due to the dynamic behavior of the domains. An interesting fact is that the power reaches a minimum when the gel undergoes a volume transition. Above that temperature the power law behavior persists and power increases again. This might indicate that the microdomains coexist even above the gel's collapse. Their relative contribution to the bulk volume would be now reversed.

The exact mechanism giving rise to the power law behavior remains, however, a mystery. Several attempts were tried to simulate this behavior on a computer, but they were unsuccessful.

CONCLUSION

The light scattering data collected along an isochore of a charged NIPA gel was presented. Its qualitative agreement with published SANS results was also reported. There appear to be two transition temperatures. At the lower one (41.5°C) the qualitative behavior of the correlation function changes – a power law component appears in addition to a single exponential. This corresponds to the emergence of a peak in the static

structure factor obtained by SANS (4) for the same sample. It is argued (after (4)) that the origin of this phenomenon is a microphase separation into dilute (charged) and dense (neutral) domains. Another transition occurs at a higher temperature (52°C) and corresponds to the volume phase transition. It is argued that the microdomains coexist even above that point.

A novel dynamic behavior is reported – the power law shape of the correlation function. Several interesting aspects were observed. It emerges at a specific temperature corresponding to the microphase separation around the Θ temperature of NIPA/AAC gel. The power itself depends on temperature, contrary to the usual scaling law behavior. An attempt was made to compare it to other known examples of such phenomenon, especially in the case of a silica gel at the gelation threshold. No definitive conclusion regarding the nature of the phenomenon was reached.

FURTHER RESEARCH

As it was mentioned several times, the mechanism giving rise to the power law decay of the correlation function is not known. It would be very interesting to investigate the problem further, both from a theoretical and an experimental point of view. In particular, it would be important to search for similar behavior in other systems to determine the universality of this behavior. The phenomenon was observed in a temperature sensitive polyelectrolyte gel. It might be tried in other circumstances. It seems that the necessary precondition was a coexistence of strong, competing interactions (here the counterion pressure and the hydrophobic interaction). It might be tried, for example, in another system where the quality of the solvent is changed by varying its composition (e.g., mixing water with acetone).

The experiments on the same kind of gel can also be expanded. An approach along the isobar (freely swollen gel) might yield some new insight. The degree of gel's ionization can be also changed, either by varying the molar ratio of the monomer, or changing the pH to influence the ionization of existing AAC units. This should help investigate the dependence of the power law behavior on the strength of the interactions.

On the theoretical front attempts should be made to determine a possible mechanism explaining the power law behavior.

REFERENCES

- [1] Hirotsu, S., Hirokawa, Y. and Tanaka, T.: *J. Chem. Phys.*, **87**, 1392 (1987).
- [2] Tanaka, T.: *Phys. Rev. Lett.*, **40**, 820 (1978),
Tanaka, T., Fillmore, D., Sun, S.T., Nishio, I., Swislow, G. and Shah, A.: *Phys. Rev. Lett.*, **45**, 1636 (1980).
- [3] Flory, P.J.: *Principles of Polymer Chemistry*, Cornell Univ. Press, Ithaca, pp. 495-540 (1953).
- [4] Shibayama, M., Tanaka, T. and Han, C.C.: *J. Chem. Phys.*, **97**, 6842 (1992).
- [5] Mandelbrot, B.B.: *The Fractal Geometry of Nature*, (Freeman, New York, 1983), p. 247.
- [6] Martin, J.E., Wilcoxon, J. and Odinek, J.: *Phys. Rev. A*, **43**, 858-872 (1991).
- [7] deGennes, P-G.: *Scaling Concepts in Polymer Physics*, (Cornell Univ. Press, Ithaca, 1979),

CHAPTER 7

ANALYSIS OF A MULTIPLE-PHASE POLYAMPHOLYTE GEL

Previous chapters dealt with either neutral (NIPA) or polyelectrolyte (copolymer of NIPA+AAc) gels. This chapter focuses on a polyampholyte gel – with both positive and negative charges attached to the network. As one can expect, its behavior is even more complicated. This particular gel (or rather a family of gels) exhibits a very complex phase behavior as pH of their environment is changed (some of them have up to seven possible phases existing at one pH value). Light scattering measurements reveal many interesting details about these gels' structure and the nature of interactions responsible for their behavior. Even though the multiple phases are not investigated in great detail (due to their very low scattering), their nature is partially revealed by experiments involving other parts of the system. One of the most important findings is the evidence that another order parameter (besides density) is needed to describe the system.

7.1 INTRODUCTION

The gel investigated in this chapter is a co-polymer of acrylic acid (AAc – a weak acid) and MAPTAC (a strong base). Fig 1. shows the chemical structure of both components. This system was first thoroughly investigated by Dr. Masahiko Annaka (1,2). It is a very interesting system, because several of the intermolecular forces compete, producing a very complex phase behavior. Fig. 2 illustrates several of the factors contributing to this behavior. Positive and negative charges are randomly distributed along the network. Acrylic acid is a weak acid ($pK_A=4.7$) so it is neutralized

at low pH and ionized at high pH. Both the total network charge and the charge distribution change with pH. This, in turn, affects several types of interactions.

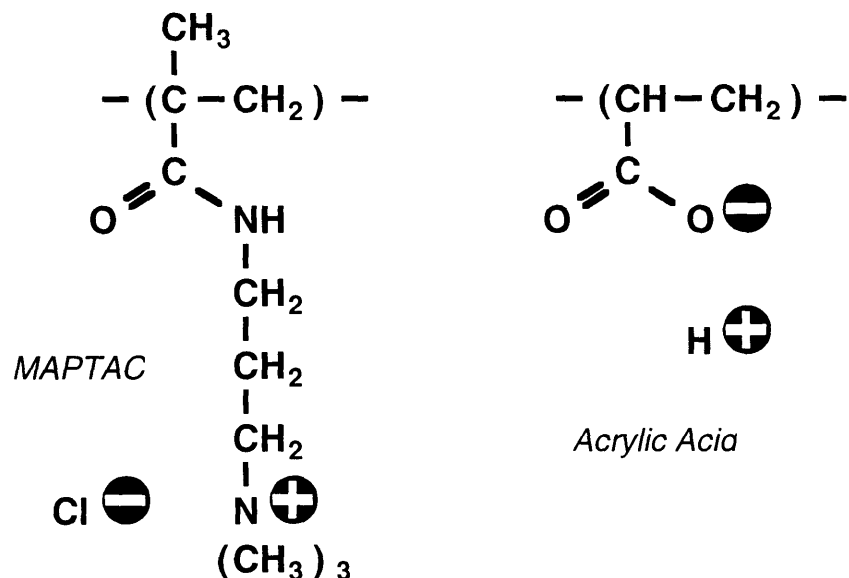


Fig. 1 Chemical structure of MAPTAC and Acrylic acid units. The network is charged when the units are ionized. MAPTAC is a strong base – it is assumed to be always ionized. Acrylic acid is a weak acid ($pK_A=4.7$ for a monomer), so it is not ionized at low pH.

As mentioned in Chapter 6, a very important factor is the osmotic pressure of counterions. When the network is charged, the counterions must be localized within the gel, so the overall electroneutrality is maintained (this is the idea behind the Donnan potential – see (3), pp. 3-134ff). Trapped counterions behave like an ideal gas exerting pressure on the confining walls – the gel-solvent boundary – thus attempting to swell the gel. This interaction depends on the net charge attached to the network, i.e. the difference between the positive and negative charge concentrations. The effect is diminished at high ionic concentrations (either in the presence of salt or at the extremes of the pH range) when the difference in free ionic concentration inside and outside the gel becomes less pronounced. Another repulsive force is the Coulomb repulsion of like charges, which, however, is heavily screened by the presence of counterions (Debye screening – see (3), pp. 3-20ff). A polyampholyte exhibits, in addition, a long range attractive force due to Debye-Hückel energy. This attraction depends on the smaller of positive and negative

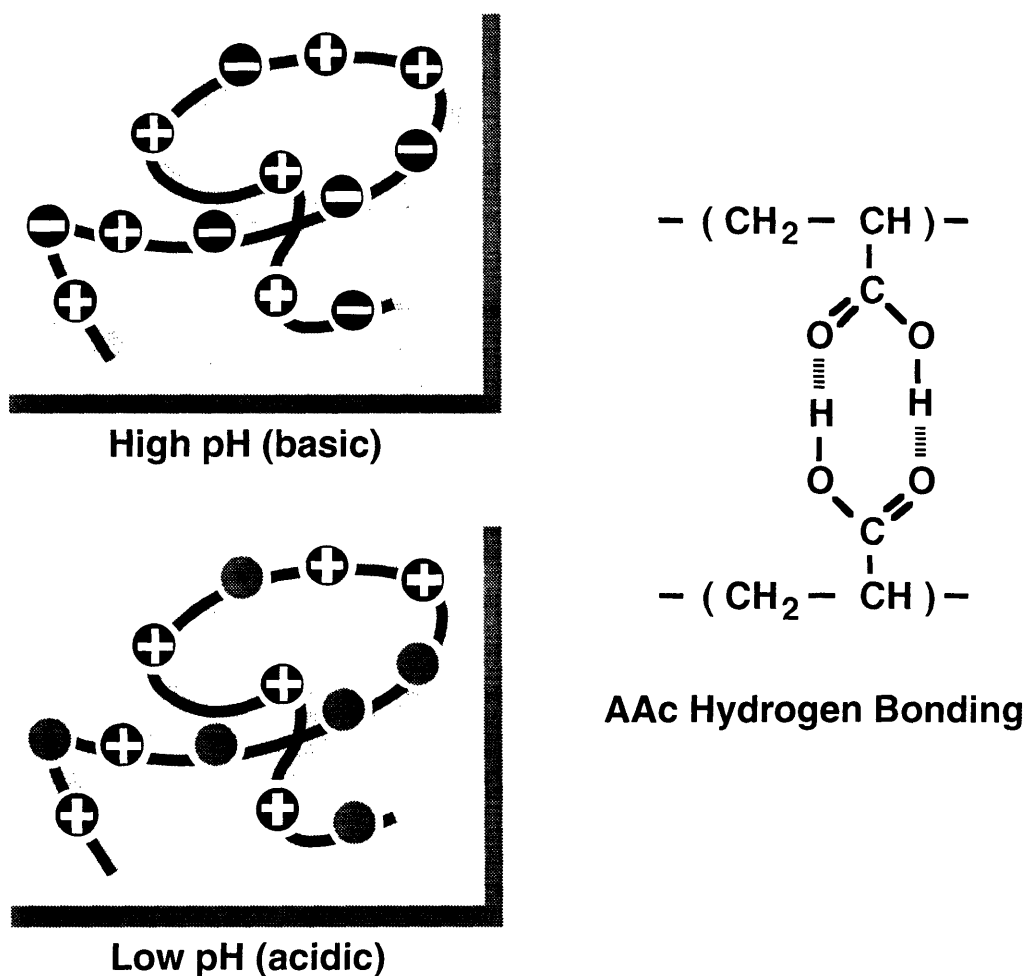


Fig 2. Illustration of the forces influencing the AAc+MAPTAC copolymer gel. The left part shows the schematic distribution of the network charge. Above the pK_A of the AAc one expects to find most of the acid units ionized (negative charges). When the conditions are acidic (below), the AAc becomes neutralized, so only the positive charge from MAPTAC is present. The counter ion osmotic pressure depends on the net charge (the difference between the positive and negative charge concentrations). The Debye-Hückel attractive interaction depends on the minimum of the positive and the negative charge concentrations. There is also the screened Coulomb repulsion of like charges. The right side shows how two units of AAc can form a hydrogen bond when they are not ionized. The hydrogen bonding introduces an additional attraction. It can also be viewed as an increase in the crosslinking density.

network charge concentrations (as it results from the attraction between opposite network charges). Finally, as illustrated on the right of Fig. 2, two acrylic acid units can form a hydrogen bond (but only when they are not ionized). Hydrogen bonding can be viewed as an attractive force, or as a temporary increase in the crosslinking density.

Given the variety of coexisting and competing interactions it is reasonable to expect a complex behavior from this gel. Fig. 3 reproduces data from Annaka (*1*), showing the swelling curves for two gels with the same total monomer concentration, but different molar ratios of AAc and MAPTAC (these two gels were investigated in this chapter). One observation immediately apparent from these graphs is multiplicity of phases coexisting at the same conditions, and dependent on the history of these conditions. This is an evidence that the concentration is not a good order parameter, or at least not the only one. Several other common features can be observed in these graphs. There is (are) transition(s) near $\text{pH}=4$ in both cases. Both gels exhibit a "ground state" between $\text{pH}=4$ and $\text{pH}=7.5(8)$. The diameter decreases at extreme pH values (an evidence of the salt effect on the counterion osmotic pressure).

7.1.1 Organization of this Chapter

The rest of this Introduction summarizes the common features of all of these experiments (sample preparation, scattering conditions and the scattering technique).

The light scattering experiments described in this chapter are organized into four groups, according to the conditions under which the scattering was performed. First we shall look at "unwashed" gels – gels that were never taken out of the pipettes in which they were prepared. Then we investigate gels whose diameter was constrained by being swollen in another micropipette. Before we investigate freely swollen gels, a comparison is made between the scattering results of a typical unwashed, constrained and free gel. Finally, and perhaps most importantly, the results of scattering from freely swollen gels at various pH values are presented.

7.1.2 Sample Preparation

The gels used throughout this chapter were all formed by free radical copolymerization of Acrylic Acid (AAc) - the anionic unit, and methacryl-amido-propyl-trimethyl ammonium chloride (MAPTAC) - the cationic unit. Their total amount was fixed at 700mM, while several different ratios were used. Consider, for example, the

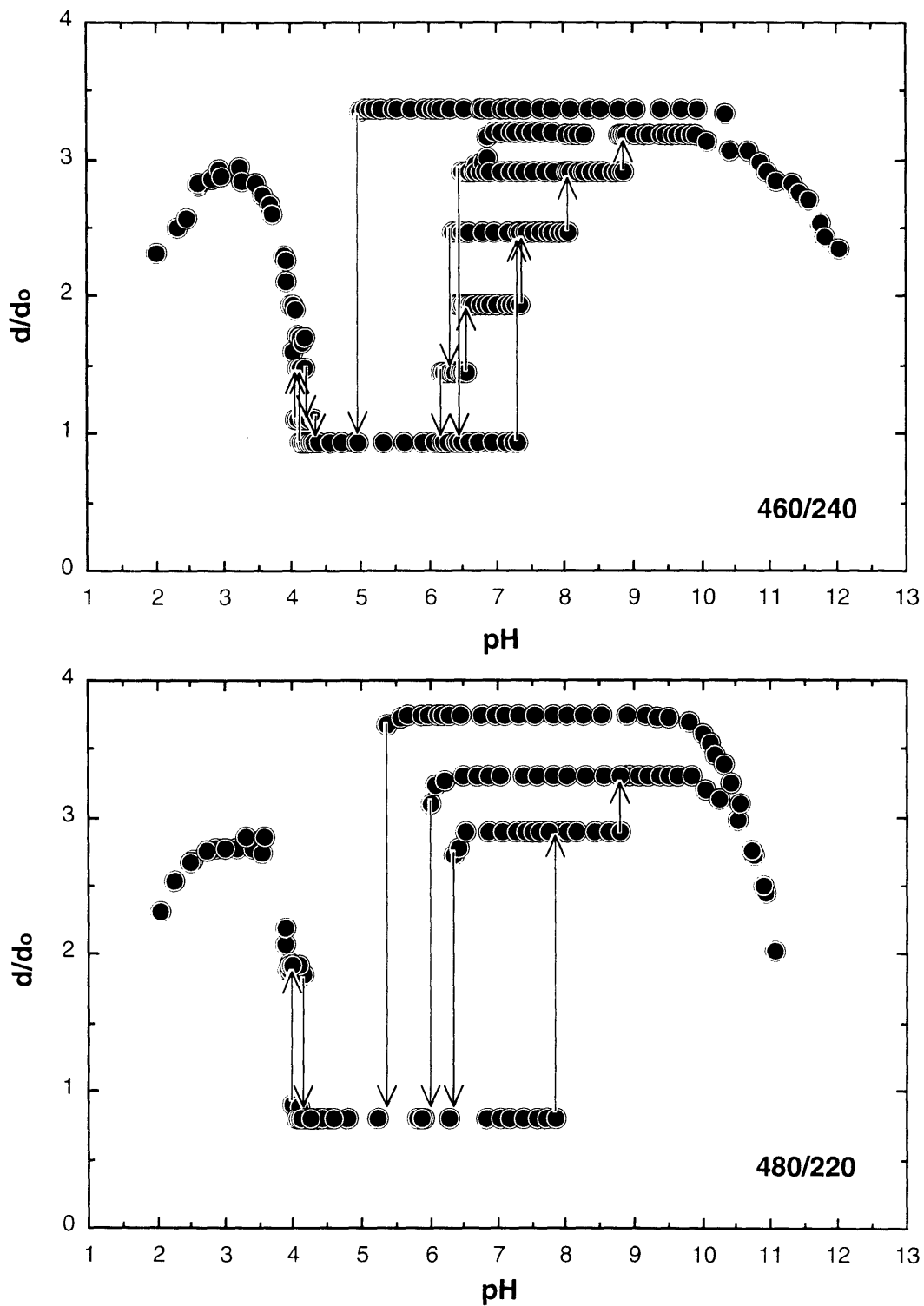


Fig. 3 pH dependence of diameter for two AAc+MAPTAC copolymer gels. Upper graph shows 460/240mM, lower – 480/220mM. Data reproduced from Annaka et al. (1).

480/220 gel (the first number represents the AAc concentration in mM, and the second – MAPTAC). In this case 0.69g (0.66ml) of purified AAc (purification was necessary to remove the inhibitor) were combined with 1.94g (1.84ml) of MAPTAC solution (in water – 50% by weight). 26.5mg (corresponding to 8.6 mM concentration) of N,N'-methylene-bisacrylamide (BIS) – the crosslinker – were then added along with 8.0mg of ammonium persulfate (initiator) and 19ml of distilled, deionized water (1ml of water was already included as a part of the MAPTAC solution). Thus prepared pre-gel solution was filtered using a 0.22 μ m filter and degassed in vacuo for 10-15 minutes (to remove the dissolved oxygen that kills free radicals). The solution was then transferred into a test tube holding some open micropipettes. The air remaining in the tube was displaced with argon gas, and the tube was sealed. Temperature of the gelation process was kept at 60°C by immersing the test tube into a circulating heat bath (Lauda model RM 6). 18 hours were allowed for gelation to complete. The micropipettes were then extracted from the bulk of the gel.

7.1.3 Temperature

The gels are not very sensitive to temperature at the room conditions. Annaka's data (2) show some temperature dependence, but only at much higher (~33°C) or much lower (~5°C) temperatures. Therefore all the experiments in this chapter were run at room temperature (23 \pm 1°C).

7.1.4 Light Scattering

The scattered light intensity and the intensity auto-correlation function were determined at an angle of 90° using the microscopic laser light scattering setup described earlier in this thesis. In all cases the software correlator with logarithmically spaced channels (described in Chapter 1) was used. The method outlined in Chapter 2 was used to analyze the data. Raw correlation functions were measured at N (50 or 150) different locations (7.5 μ m apart) by laterally translating the sample. They were summed and normalized forming an approximation $g_N^{(2)}(t)$ of the ensemble average $g_E^{(2)}(t)$ (see Chapter 2). The optical setup was the same in all cases (unless indicated otherwise), so the scattering intensities can be compared directly. The decay time τ was obtained by fitting $g_N^{(2)}(t)$ with a single exponential $A e^{-t/\tau^*} + B$ and then correcting τ^* for heterodyning of \bar{I}_D with $\langle I_S \rangle_N$ (see again Chapter 2).

7.2 "UNWASHED" GELS - DEPENDENCE ON PREPARATION CONDITIONS AND COMPOSITION

In the first set of experiments the light scattering from "unwashed" gels was investigated. The light scattering was performed inside the pipettes in which the gels were made – they were never taken out – thus the term "unwashed".

7.2.1 Experiments

A set of 480/220 gels was prepared according to the recipe above, but the pre-gel solution was partially neutralized by addition of some NaOH. pH of an untreated pre-gel solution is 2.6. By adding NaOH a set of pH values was established ranging from 2.6 to 8.0. The scattering was then performed as described above.

In another experiment gels of different molar ratios of AAc and MAPTAC (but fixed total concentration) were synthesized. The AAc concentration ranged from 355mM to 450mM (MAPTAC from 345mM to 250mM).

In these two experiments only, an older version of the scattering optics was used, where the consistency of scattered intensity between measurements was harder to maintain.

7.2.2 Results

Fig. 4 shows the results of light scattering from gels prepared at different pH's. There appear to be two regimes – one at low, one at high pH values. The dynamic intensity appears constant within each regime (top graph). The static intensity fluctuates more, but this may be simply because there is bigger uncertainty in the static intensity (see Chapter 2). The fraction of dynamic intensity R (middle graph) is quite constant. The decay time follows the general pattern of the intensities, but it keeps increasing with increasing pH. The transition is also not as sharp.

Fig. 5 presents the composition dependence of the light scattering data. It is clear from the graphs that none of the parameters are very much influenced by the varying ratio of co-monomers. The intensity fluctuates a little, most probably due to an experimental error. Overall, it remains rather constant. The fraction of dynamic intensity R (which is independent of the absolute value of intensity) is presented in the middle graph. It is

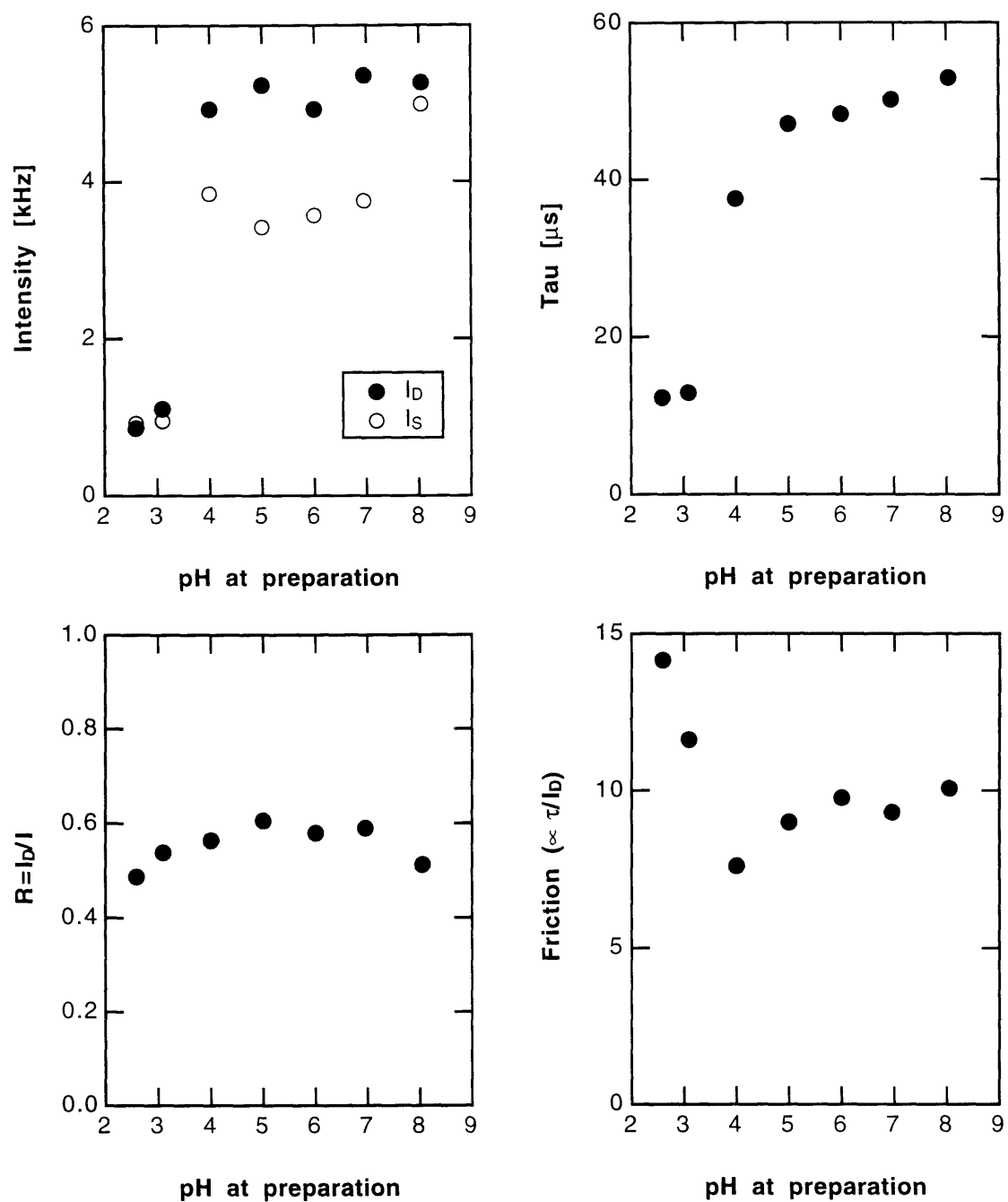


Fig. 4 Dependence of light scattering parameters on the pH of gel preparation. The gels were never taken out of the micropipettes in which they were prepared. Top left graph has dynamic and static intensities, bottom left – the fraction of dynamic intensity, top right graph shows the decay time, bottom right – network-solvent friction. The intensities and the decay time jump near pH = 4.

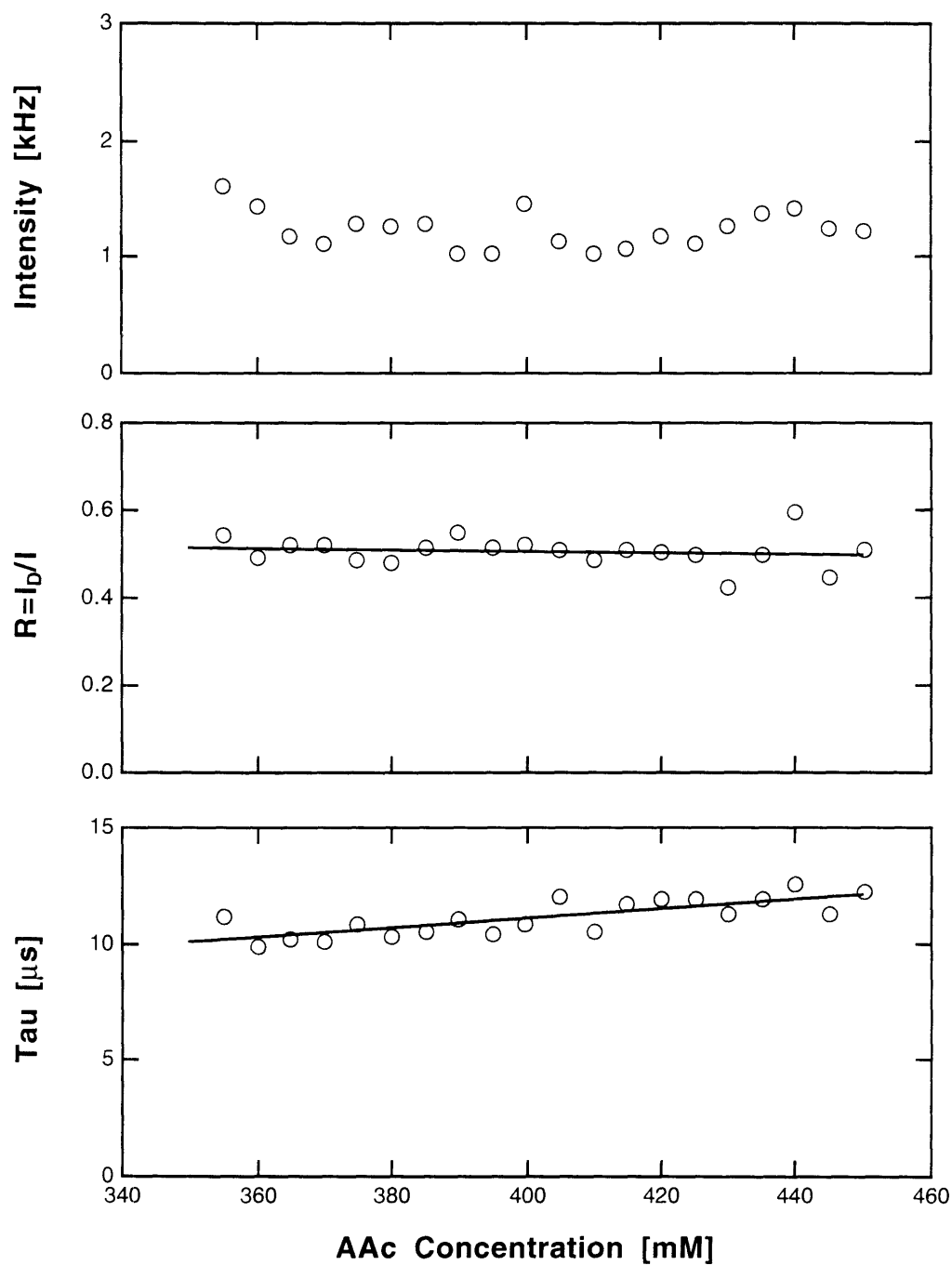


Fig. 5 Composition dependence of light scattering results. The total monomer concentration is 700mM so [MAPTAC]=700mM-[AAc]. The gels were never taken out of the pipettes in which they were prepared. The total intensity (top), the fraction of dynamic intensity (middle), and the decay time (bottom) are only weakly affected by the composition.

quite constant, and the least-square fit line is almost horizontal. The decay time (bottom graph) shows a slight, but consistent increase with increasing AAc concentration.

7.2.3 Discussion

The abrupt change in the scattering parameters when pH crosses the value of 4 (Fig. 4) can be better understood when compared to the swelling curves of Fig. 3. The jump occurs at the place where the freely swollen gel collapses from a diameter of 2–3 d_0 to $d/d_0 \approx 1$ (an order of magnitude increase in concentration). In a crude approximation the AAc/NIPA gel can be viewed as a polyelectrolyte, so the swelling would be due to the counterion osmotic pressure. Larger swelling corresponds to larger network pressure. This can be seen explicitly from the concentration dependence of the osmotic pressure of counterions (4):

$$\Pi_{\text{ion}} = C \cdot k_B T \left(\frac{\phi}{\phi_0} \right)$$

where Π_{ion} is the counterion contribution to the osmotic pressure, and C – the network charge concentration at $\phi = \phi_0$ ($d/d_0 = 1$). The bulk modulus K is defined as

$$K = \phi \left(\frac{\partial \Pi}{\partial \phi} \right)_T$$

Thus the counterion contribution to the bulk modulus is numerically equal to the counterion contribution to the osmotic pressure. Therefore larger equilibrium diameter (below $\text{pH} \approx 4$) implies larger charge concentration, which leads to larger bulk modulus for a gel confined to $d/d_0 = 1$. Both the decay time and the dynamic intensity are inversely proportional to the elastic modulus, so both should be smaller. This is consistent with the data from Fig. 4. Of course, this is a very crude approximation, and there are many problems with it. For example, there is only a very small pH range near the pK_A of AAc (~ 4.7) for which the network charge vanishes. Above that pH one would expect all of AAc to be ionized. There should be a net negative charge, since there are 480mM of AAc and only 220mM of MAPTAC. Therefore some other factor should be responsible for the low bulk modulus there. Presumably this is the same factor that causes the gel to be in the "ground state" for $\text{pH} < 8$ (hydrogen bonding?).

The data from Fig. 5 present another problem. Presumably at the pH value of the pre-gel solution most of AAc is not ionized. Therefore the network charge should be due mainly to MAPTAC. However, MAPTAC concentration in Fig. 5 changes from 345mM to 240mM with little discernible effect on the scattering parameters. The slight change in decay time is at least consistent with the argument above (higher τ for lower charge). This could mean that the charge effect is saturated – other contributions to the bulk modulus are more significant.

To summarize, the correspondence between the increase in the scattering parameters and the free gel entering the "ground state" as pH increases, is worth keeping in mind. This will be further explored when the experiments on free gels are described.

7.3 "CONSTRAINED" GELS - DIAMETER DEPENDENCE

This section carries us a step further towards more complicated conditions. It describes experiments carried out on gels that were partially allowed to swell, but whose diameter was constrained by a micropipette in which they were swollen.

7.3.1 Experiments

Fig. 6 shows the preparation of a constrained gel. The gels (480/220) were prepared in micropipettes, as described in the Introduction. Subsequently they were extracted from these micropipettes. Since the gels were extremely sticky (especially after contact with water), and a contact with methanol seemed to alter the gel structure, a special procedure was devised for extracting them. The micropipette holding the gel was cut to a desired length, and one of its ends was pushed into Critoseal, so that the gel started emerging from the other end. A portion of the gel was then squeezed out by pushing the Critoseal end with a piston of an appropriate diameter (for larger micropipettes), or by inserting the micropipette into a closely fitting larger one, where the Critoseal was used to transmit the piston pressure onto the gel (for smaller micropipettes that would not admit a piston). The gel was only partially extracted, so that it could be washed by hanging the micropipette over a beaker with water, with the gel washing in the beaker. When placed in pure water the gels first swell (because of the ions present from the gelation process), and then collapse as the ions diffuse out. The water in the beaker was changed several times during the 24 hours allowed for the gel to wash. The gel was then taken out of the water and allowed to dry for a day (Fig. 6-2). After that, the gel was

cut from the micropipette and placed in a micropipette of a different diameter (Fig. 6-3), which was then filled with a NaOH solution of pH=10 (using a syringe), so that the gel would swell (Fig. 6-4). The gel was then allowed several weeks to equilibrate. The micropipette was then sealed and placed in a water-filled light scattering cuvette for light scattering measurements.

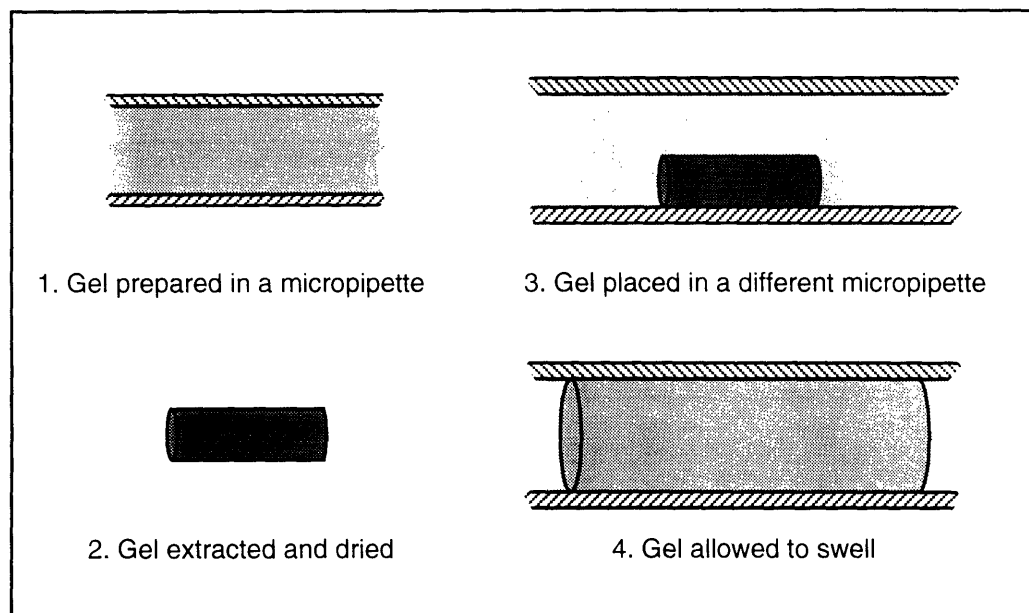


Fig. 6 Preparation of a constrained gel. The value of d/d_0 is determined by the ratio of diameters of the pipette in which the light scattering is performed (the pipette on the right of the figure) and the pipette in which the gel was made (upper left). An extra complication is due to the fact that swelling of the gel is not affine (the diameter to length ratio is not maintained) when the gel is swollen under constraint.

7.3.2 Results

First observation regards the relaxation time. When the length of the dried gel was several times its diameter, the light scattering results indicate a very slow equilibration process. Fig. 7 shows two plots of the position dependence of scattering intensities for two gels of constrained $d/d_0 \approx 1.2$ (the top figure has 1.155, the bottom –

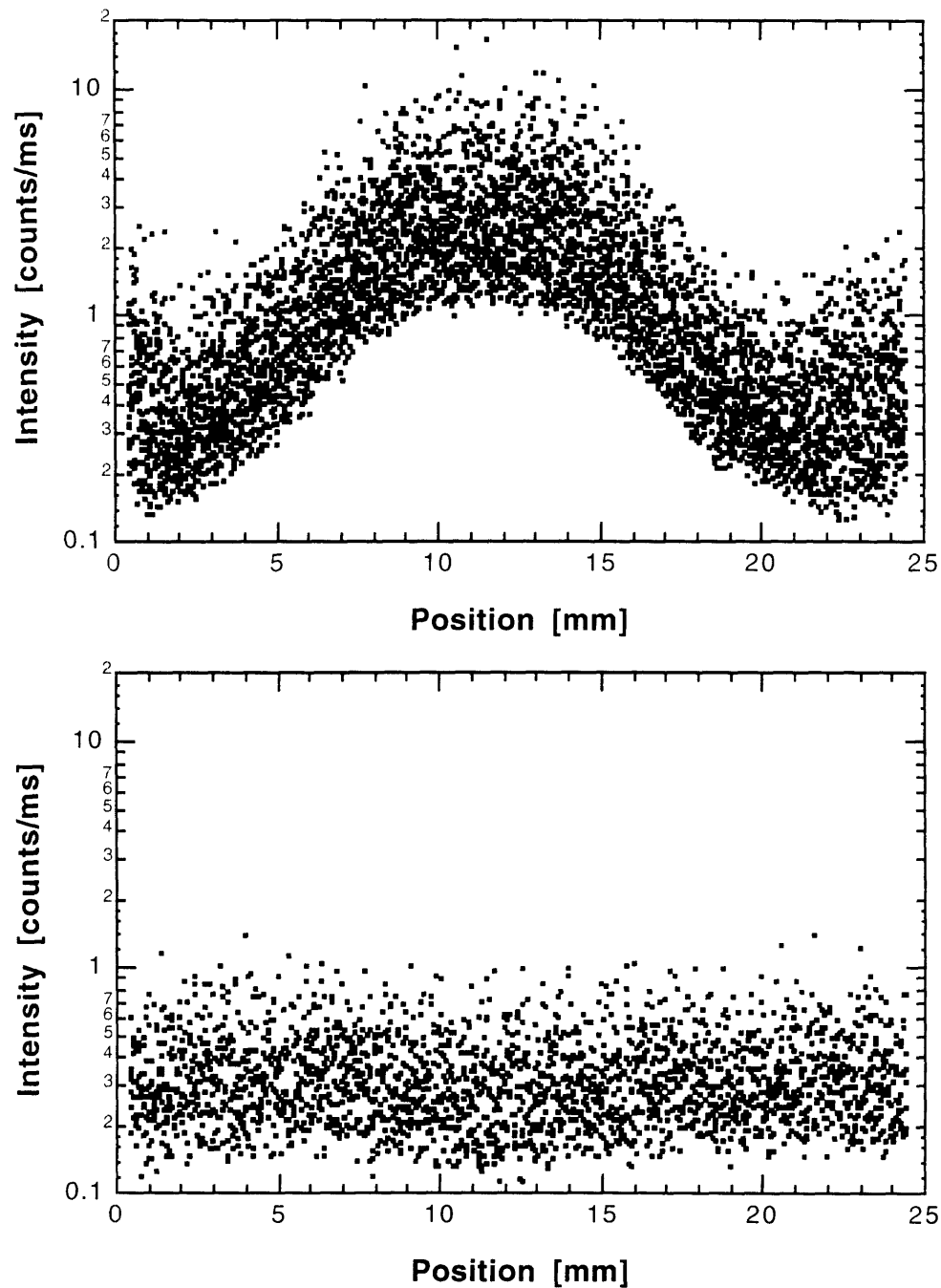


Fig. 7 Position dependence of scattering intensity for two gels whose diameter is constrained by a micropipette. In the top graph the gel has been equilibrating for two weeks. In the second case a gel from the same batch was examined after one year. N.B. in the upper curve both dynamic intensity (the lower edge) and the static intensity are clearly discernible. Both intensities are much higher at the center than at the edges, which have more freedom to relax.

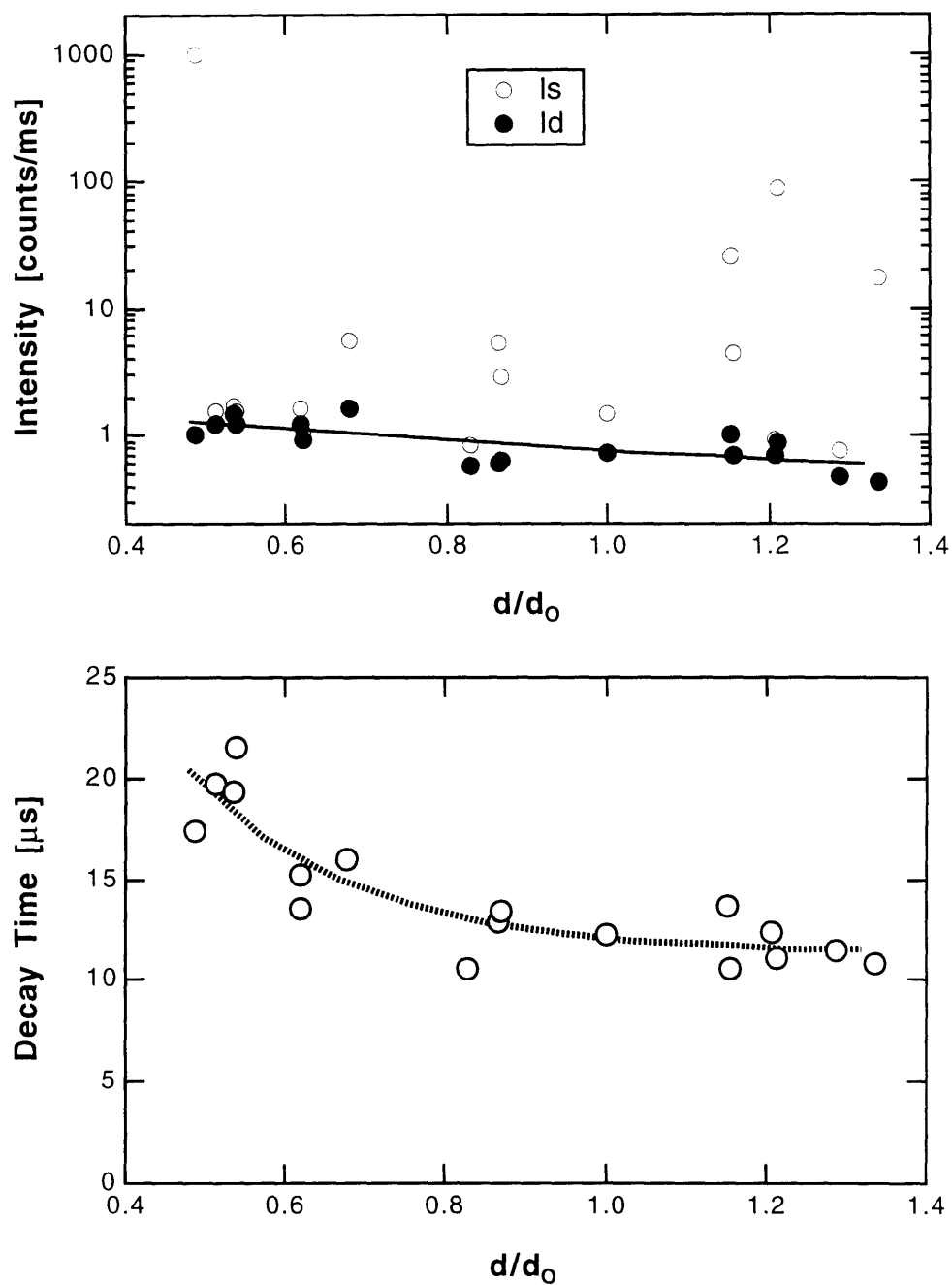


Fig. 8 Light scattering from gels constrained to different diameters by swelling in a different pipette than that in which it was made. The top graph has the static and dynamic intensities, the bottom – the decay time. The decay time and the dynamic intensity are mildly decreasing with increasing d/d_0 . The static intensity is scattered, possibly due to incomplete relaxation. At $d/d_0=0.486$, which almost corresponds to a dried gel, the static intensity is enormous.

1.208). The difference is that the top data was collected after two weeks of equilibration, while the bottom gel was allowed to equilibrate for a year. It is evident from the top graph that the center of the gel scatters light much more than the edges. There is about an order of magnitude difference in both the dynamic (the bottom edge of the scattered plot) and the static (the average of the outer envelope) intensities. The lower graph shows that after one year both the static and the dynamic components are position independent.

Fig. 8 shows the light scattering results from various constrained gels plotted against the constrained diameter. These gels had a small length to diameter ratio, so they should have been equilibrated. The top graph shows the scattering intensity (both static – open circles and dynamic – black circles). The dynamic intensity seems to be weakly decreasing with diameter. The static intensity is quite scattered. The bottom graph shows the decay time, which also mildly decreases with increasing diameter.

7.3.3 Discussion

The difference between the two graphs in Fig. 7 is an evidence that the strong scattering in the center is due to kinetics. The other possible explanation would be that the cause is the equilibrium strain distribution. However, the lower graph shows that after a long enough delay the scattering becomes uniform throughout the gel. This also strongly indicates that the swelling of a gel under constraint is not an affine process, i.e., the gel swells more along one direction than along the others (as explained by Rabin (5)). The gel is supposed to swell isotropically in all directions if it is free (cf. Y. Lee et al. (6)). This should happen until it reaches the walls of the confining pipette. If the gel were affine, the process would stop there, and the gel would be equilibrated at that moment. This does not happen. The most obvious explanation is that the edges, which are less constrained by the bulk of the gel to relax along the pipette, relax first. The rest of the gel relaxes (maintaining a shear deformation) as the edges are pushed away against gel-glass friction towards the ends of the pipette. Therefore the edges, being less concentrated, scatter less light than the center. This is consistent with the data of the upper graph of Fig. 7. Another direct evidence of the non-uniform swelling is that after one year the gel presented in the bottom of Fig. 7 took up the entire length of the micropipette (2.5cm) while the length of the dried gel ($d/d_0 \approx 0.45$) was only about 5mm. Thus a 2.5 fold increase in diameter was accompanied by a 5 fold increase in length (these figures are only approximate).

Considering the above explanation, the data in Fig. 8 produce a further interesting aspect of the non-uniformity of gel swelling. For a freely swollen gel the light scattering

parameters should depend strongly on the diameter. Let's recall a formula for the dynamic part of light scattered from a gel network (Chapter 2, Eqn. 20):

$$\langle E(\mathbf{q}, t) E(\mathbf{q}, 0) \rangle \propto \left(\frac{\partial \varepsilon}{\partial \phi} \right)_T^2 \phi^2 \frac{k_B T}{K + \frac{4}{3} \mu} \exp \left[- \frac{(K + \frac{4}{3} \mu) q^2 t}{f} \right]$$

This formula was explained elsewhere (Chapter 2). What is of interest here is the concentration dependence of the dynamic scattering intensity: $I_D \propto \phi^2 \propto (d / d_0)^{-6}$. The diameter in Fig. 8 changes by a factor of 3, so for an affinely swollen gel one would expect a 700 fold decrease in intensity. However, nothing like this happens. The dynamic intensity changes by at most a factor of 2. A plausible explanation for this fact is that the gel almost reaches its equilibrium concentration, undergoing a large shear deformation in the process. Another evidence supporting this hypothesis is that the ratio of decay time to static intensity (which was argued in Chapter 5 to be proportional to the network-solvent friction) is almost constant over the entire d/d_0 range covered here. The friction should be strongly concentration dependent. The absence of this dependence may further indicate an equal concentration in all cases.

The scatter of the static intensities is hard to explain. The easiest explanation would be to assume that the gels were not completely relaxed. However, as evidenced by the top graph of Fig. 7, in such case the dynamic intensity should follow the static intensity. Another trivial explanation would be the presence of dust, but the pre-gel solution was filtered, after the dust was determined to be a problem with previous batches of gels. A more exotic hypothesis would be to assume that at certain values of d/d_0 the gel assumes a particular spatial configuration ("structure"). This was the original motivation behind this experiment. It is hard to argue this hypothesis based on the available data. Another possible explanation would be to adopt the idea of periodic modulation of the structure, introduced by Candau et al. (7). The variations in the static intensity would then correspond to variations of the characteristic length of this modulation, probed by a fixed scattering vector. When the scattering vector coincides with the mean distance between dense regions, we get strong static scattering. Finally, the gel constrained to $d/d_0=0.486$ has the static intensity several orders of magnitude higher than at higher diameters. This might be because this diameter is close to the diameter of the dried gel ($\phi=100\%$). It is reasonable to expect a high nonuniformity and thus high static scattering in such case.

7.4 COMPARISON OF UNWASHED, CONSTRAINED, AND FREE GELS

Having discussed the unwashed and constrained gels with d/d_0 near 1, and before examining freely swollen gels at large diameters this seems like a right point to compare the behavior of the prior two with that of the "ground state" ($d/d_0 \approx 1$, see Fig. 3) of the freely swollen gel. The comparison should also give important insights into the behavior of free gels.

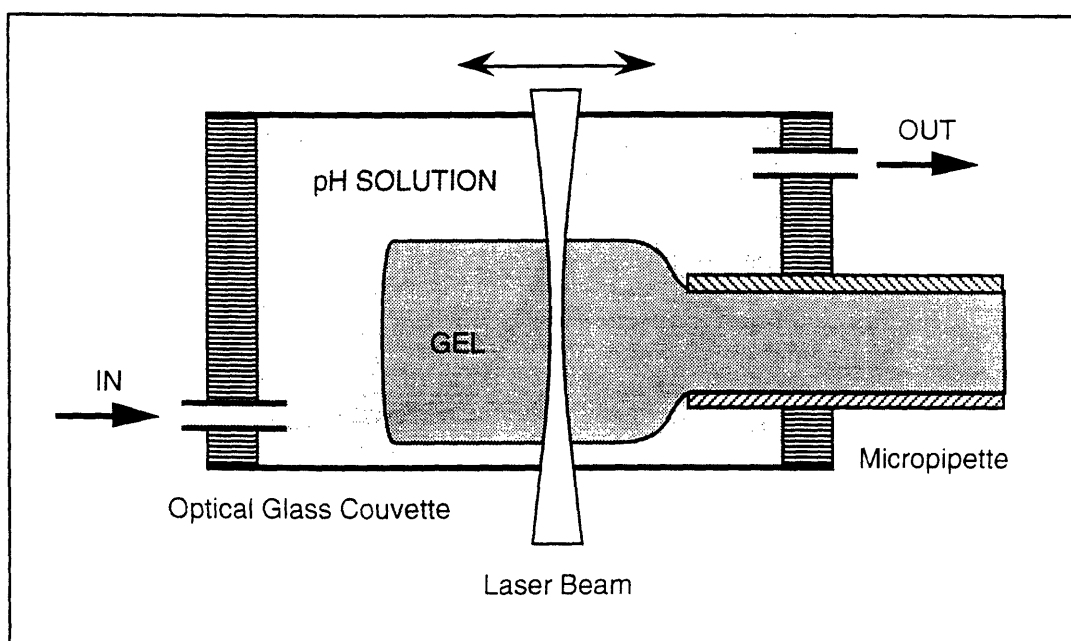


Fig. 9 Scattering setup for a freely swollen gel. Part of the gel is pushed out of the micropipette in which it was made using a piston of matching diameter. This portion is allowed to swell freely as a solution of controlled pH flows through the cuvette. The gel is held in place by the micropipette in which it was made.

7.4.1 Experiments

Gels with AAc/MAPTAC ratio of 460/240 were used for this comparison. The details of the scattering from unwashed and constrained gels were discussed before (this constrained gel was equilibrated for a year). The experimental arrangement for the scattering from the freely swollen gel is depicted in Fig. 9. The gel was partially

extracted from the micropipette in the same way as described in the section about constrained gels. This micropipette was then fixed at the side of the light scattering cuvette so the free gel was bathed by the solution of controlled pH. The light scattering was performed on that gel through the walls of the cuvette (made from an optical glass). The "ground state" was reached by running distilled, deionized water through the setup.

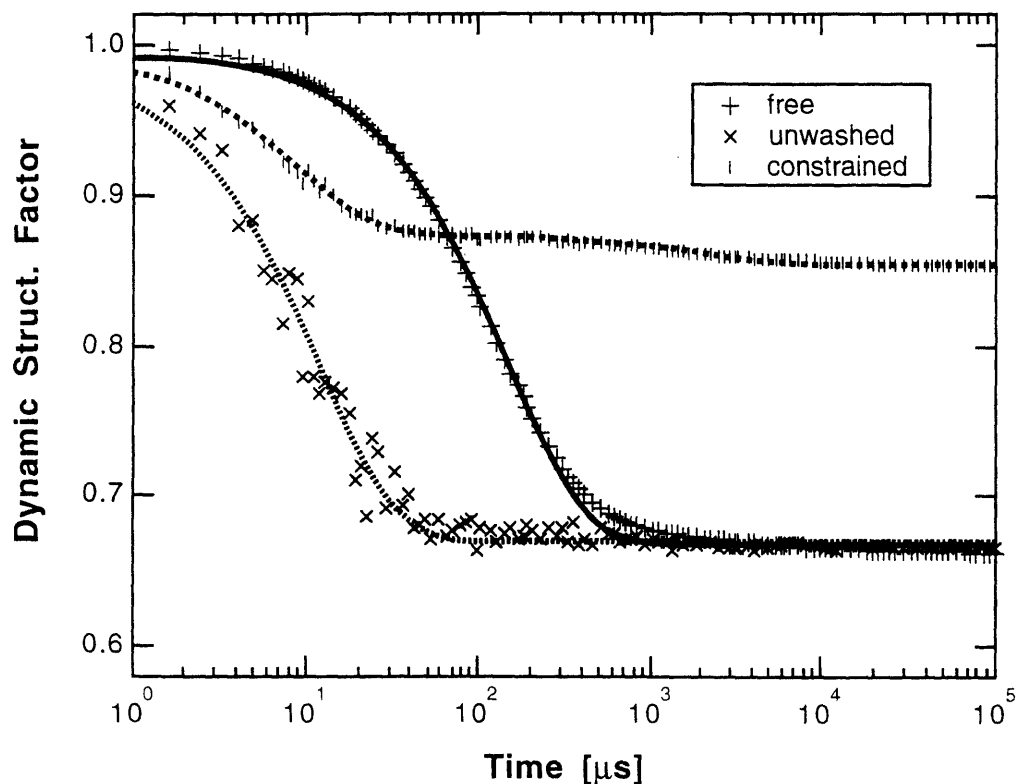


Fig. 10 Comparison of dynamic structure factors (normalized electric field autocorrelation functions) for unwashed ($d/d_0=1$), constrained ($d/d_0=0.828$), and freely swollen ($d/d_0=1.05$) gels. The free gel's decay time is about an order of magnitude larger than the unwashed one's, but otherwise the two curves are quite similar. They are reasonably well fitted by single exponentials (solid curves). The constrained gel is adequately fitted by a double exponential (solid curve).

In a control experiment the solvent was extracted from the unwashed gel by placing the gel in a specially constructed metal syringe (the "Gel Squeezer"), where on one end the solution (but not the gel) could pass through a compressed cotton, and on the

other end a large pressure was applied. After several days of applying pressure (through a large C-clamp) several milliliters of the solvent were extracted. Its refractive index was then determined using a clinical refractometer.

7.4.2 Results

The normalized ensemble averaged electric field autocorrelation functions (dynamic structure factors – computed as in Chapter 2, Eqn. (12)) for different gel conditions are presented in Fig. 10. The gels follow a single exponential decay reasonably well, which validates the use of the analysis methods of Chapter 2 (which were used up to now anyway). There is a slight non-single exponential tail, most clearly visible in the case of free gel. The constrained gel is reasonably well fitted by a double exponential. One point immediately evident from the graph is that the decay time of the freely swollen gel is an order of magnitude larger than in the other two cases. Otherwise the free gel's curve is quite similar to the unwashed gel's. The similarity of the static/dynamic intensity ratios (manifested by the fact that the infinity values overlap) could be a coincidence. This is because spurious scattering from glass, etc., could contribute significantly to the unwashed gel's static intensity (as the scattering intensity from the unwashed gel is extremely low). Table 1 summarizes the scattering results.

gel condition	d/d_0	ϕ/ϕ_0	τ [μ s]	I_D	I_S	K	friction
Unwashed	1	1	11.9	0.27	0.53	3700	44.7
Constrained	0.83	0.7(?)	8.8 2120	0.37 0.06	2.61	1300	11(?)
Free	1.05	0.87	149	11.8	23.0	64	9.4

Table 1 Comparison of scattering results for different gel conditions.

The friction f is calculated from $(\tau/I_D) * (\phi/\phi_0)^2$, and the elastic modulus K from $(\phi/\phi_0)^2/I_D$ as it was done in Chapter 5 (both are given in arbitrary units). The concentration of the constrained gel is only an estimate, since the lengthwise swelling is not exactly known. This also introduces an uncertainty in the friction f . It is evident from these data that the free gel behaves quite differently from the other two, even though the network

concentrations are similar. The decay time is about 12 times larger than for the unwashed gel, while the intensity (both static and dynamic) is about 44 times larger. An interesting fact is that the friction as calculated above is 5 times smaller for the free gel, while the elastic modulus (proportional to $(\phi/\phi_0)^2/I_D$) is about 60 times smaller.

The refractive index measurements reveal that the refractive index of the liquid extracted from the gel is indistinguishable from that of water.

7.4.3 Discussion

The most interesting fact discussed in this section is the large difference in behavior of an unwashed gel and a freely swollen gel in its "ground state" (N.B. this is not the densest accessible state – that can be accomplished by collapsing the gel in acetone, but it then becomes completely opaque). The fact is even more striking given that the diameters (and thus the concentrations) are very similar in both cases. One easy explanation would be to assume that the low scattering of the unwashed gel is due to a weak contrast between the collapsed gel and the solvent due to the presence of gelation residues – unbounded monomers, salt, etc. This hypothesis is easily disproved when the index of refraction of the solution squeezed out of the gel is examined. This solution would, in fact, contain all the residues that one may worry about. However, its index of refraction is practically equal to that of water, so there can be no argument about decreased contrast. It cannot be an effect of the remnant salt either, since the gel swollen freely in salt scatters similarly to the one in water (see next section).

The following argument is at least plausible, though further experiments would be needed to clarify it. When the gel is polymerized, the chains approximate Gaussian coils. This happens "by construction", since the polymerization occurs by random addition of monomers to the ends of existing chains, and by random joining of already formed clusters. When the gel is washed, i.e., allowed to swell and change its configuration, the chains have an opportunity to interact with each other, cluster, form or break hydrogen bonds, etc. Therefore the equilibrium configuration is lost. We observe that in case of the free gel, even though its diameter is almost the same as for the unwashed case, the friction is 5 times smaller, the elastic modulus 60 times smaller, while the static intensity is 45 times larger. If we assume that the chains form some local clusters, this would explain these results. The clusters have to be interspersed with less dense regions, so the overall friction decreases. Bulk modulus decreases since the loose regions are more compressible (bulk modulus is the incompressibility). Finally the static intensity

increases due to more inhomogeneous distribution of chains. The following section will look at possible mechanisms responsible for this clustering.

7.5 "FREE" GELS - pH DEPENDENCE

Finally we are in the position to discuss the pH dependence of light scattering from freely swollen gels. The original motivation for this research was to investigate the possible differences between scattering behavior of multiple phases in the neutral to basic regime (see Fig. 3). Unfortunately, the gels are extremely dilute at these swelling ratios, so it was almost impossible to obtain good quality scattering data under these conditions. This section focuses instead on scattering in the acidic region, where a single "hump" is present. Even this region reveals many surprises. A near critical behavior is observed near $\text{pH}=4$. Even more interestingly, the light scattering data present a direct evidence that the diameter (or concentration) is not a good order parameter (or at least not the only one). Different internal structures can exist at the same concentration.

7.5.1 Experiments

A single gel with AAc/MAPTAC ratio of 460/240 was used in this experiment. The measurements were performed using an arrangement depicted in Fig. 9 and described in the previous section. pH of the gel's environment was controlled by flowing a solution of monitored pH through the scattering cell (as shown on Fig. 9). For $\text{pH}<5.8$ an HCl solution was used. For $\text{pH}>5.8$ it was a NaOH solution. Two control experiments were also performed with neutral NaCl solutions (50mM and 500mM).

7.5.2 Results

The swelling curve and the scattering parameters for the low pH region are plotted in Fig. 11. The swelling curve appears smooth, contrary to Annaka's results for the same gel (top graph of Fig. 3, near $\text{pH}=4$; Ref.'s (1,2)). One observes, though, that the discontinuous transition in the top graph of Fig. 3 is much smaller than the transition in the bottom graph (for 480/220 gel). Thus one may assume that the transition in the 460/240 gel occurs near the critical point, so a small variation in the preparation could

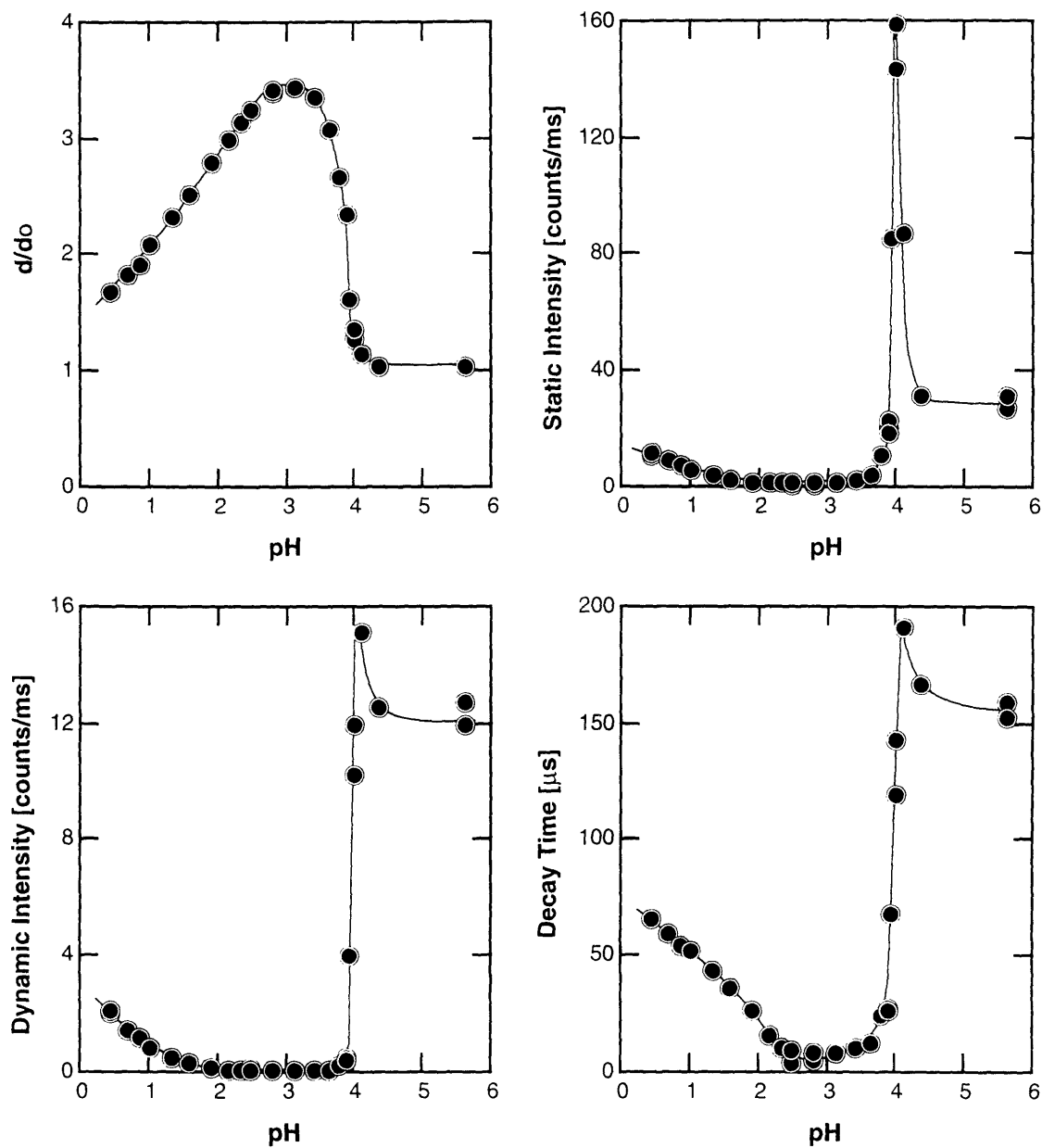


Fig. 11 pH dependence of d/d_0 and the light scattering parameters in the acidic region. d/d_0 (upper left) seems continuous, but the light scattering parameters reveal a near-critical behavior near $\text{pH}=4$. The most drastic divergence occurs in the static intensity (upper right). The dynamic intensity (lower left) and the decay time (lower right) also seem to behave pre-critically at that value of pH. The divergence is much less pronounced in this case. Another general trend is that, with the exception of the near-critical behavior, all the values decrease with increasing d/d_0 (decreasing concentration).

push the transition into a continuous regime. Another difference is that Annaka's gels were extracted in methanol, which the light scattering measurements showed to alter gel's characteristics. This should be sufficient to explain the discrepancy.

While the swelling curve is continuous, there appears to be a nearly singular behavior in the scattering parameters. The biggest change occurs in the static intensity, which has a large peak near $\text{pH}=4$. The dynamic intensity and the decay time also peak at the same pH , but above it they level to a value only slightly smaller than the peak.

Another way of plotting the same data is presented in Fig. 12. Here the horizontal axis represents the swelling ratio d/d_0 . The top graph is the same as the top left graph of Fig. 11. The points are color-coded, so that at pH values below the peak diameter they are white, and above they are black. This is just a reference for the two graphs below. The middle graph shows the dynamic intensity as a function of d/d_0 . It seems to be a well-defined function of concentration – both the black and the white curves fall on top of each other. A different thing occurs in the bottom graph, where the static intensity is plotted as a function of the swelling ratio. The black and white branches are clearly distinguishable – they no longer fall on top of each other. Higher pH values correspond to a higher intensity at the same diameter.

Fig. 13 summarizes the concentration dependence of the intensities presented first in Fig. 12. Data obtained at high pH 's (NaOH) and in NaCl are also included. We observe again a single branch of the dynamic intensity, and two branches of the static intensity (plotted here as a loop). In the latter case the low pH (<3) and salt data fall on the lower branch, while the higher pH data – on the upper branch.

Bulk modulus calculated as above ($\propto (\phi/\phi_0)/I_D$) is presented in Fig. 14 against the diameter (top graph) and pH (bottom graph). There are two interesting observations: bulk modulus is only weakly dependent on concentration for $d/d_0 > 1.5$ (from the top graph), and the "ground state" is clearly very different from the remainder of the gel (the "ground state" is at the upper line of the bottom graph). N.B. bulk modulus of an unwashed gel was 3700, compared to the range 5-65 presented here. Another observation is that there is no singularity in the bulk modulus (as contrasted with the data in Fig. 11).

7.5.3 Discussion

The plots of Fig. 11 support the idea that we are near a critical point at $\text{pH}=4$. It is doubtful whether this behavior could be contributed to kinetics (incomplete equilibration). The peak does not correspond to the largest change in diameter, so other

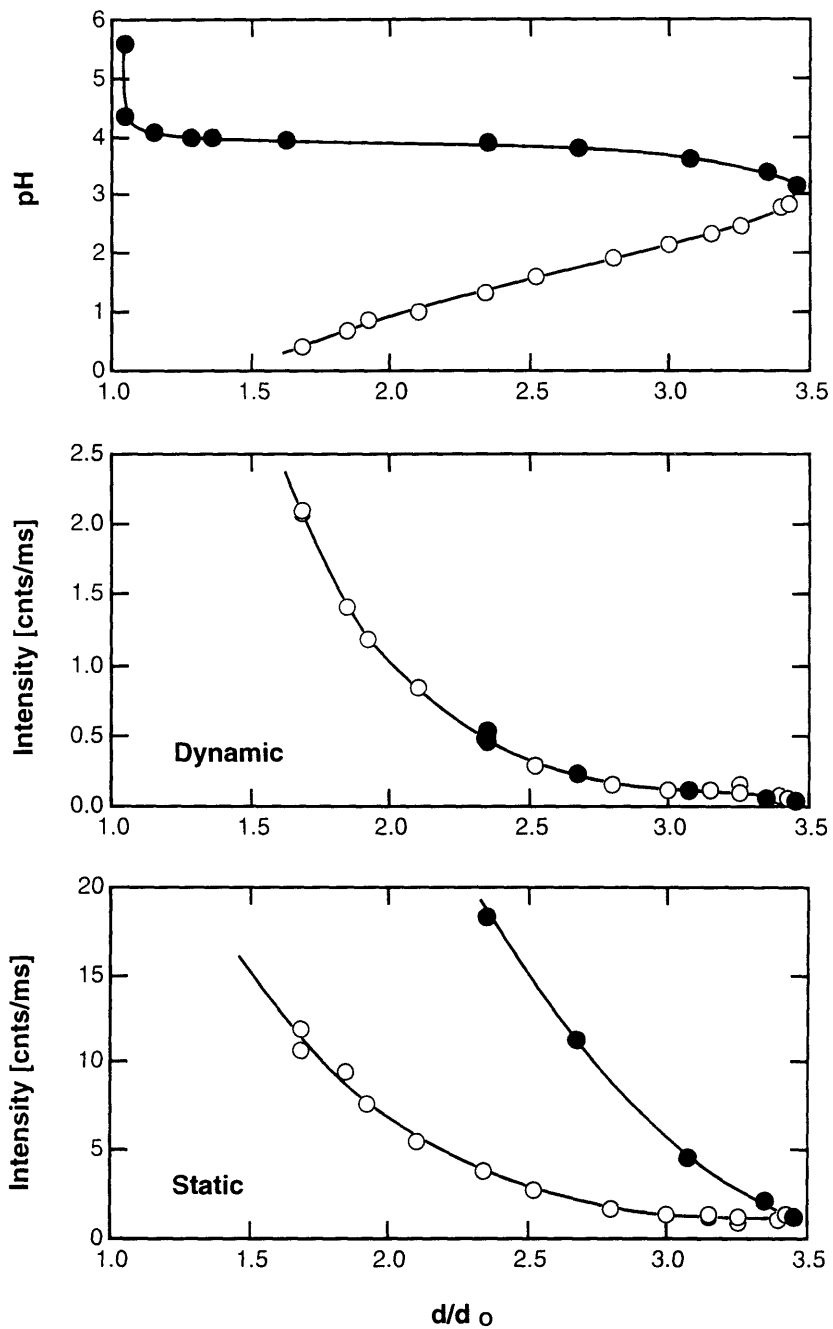


Fig. 12 Diameter dependence of dynamic and static intensity. The top graph, shown here for reference, is the usual swelling curve, but with the axes swapped. The higher pH (with respect to the peak of d/d_0) portion of the curve is marked black, and the lower one white. In case of the dynamic intensity (middle graph) both curves fall on top of each other, so I_D is a function of d/d_0 only. In case of the static intensity the two branches are clearly distinguishable.

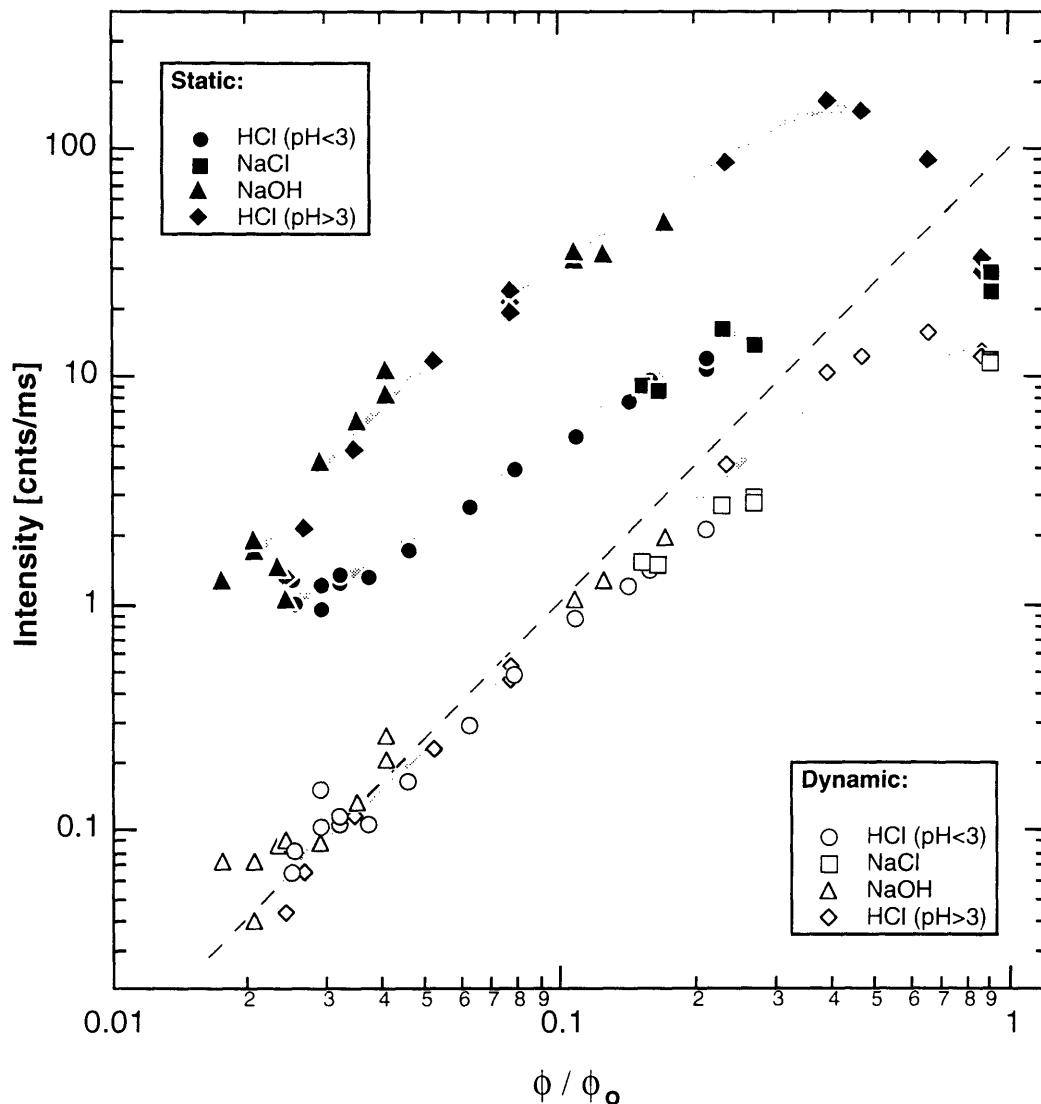


Fig. 13 Intensity as a function of concentration. Plot of both dynamic (white) and static (black) intensities vs. $\phi/\phi_0=(d/d_0)^{-3}$. The gel was in contact with HCl (circles and diamonds), NaOH (triangles) and NaCl (squares). Thick lines are guides to the eye. Dashed line has a slope of 2 ($\propto \phi^2$) expected for a neutral gel. It is again evident that the dynamic intensity is simply a function of concentration (with an exponent slightly less than 2), while there are two separate branches of static intensity dependence. Interestingly, low pH HCl data, and NaCl points fall together on the lower branch, while higher pH HCl and NaOH points are all on the upper branch.

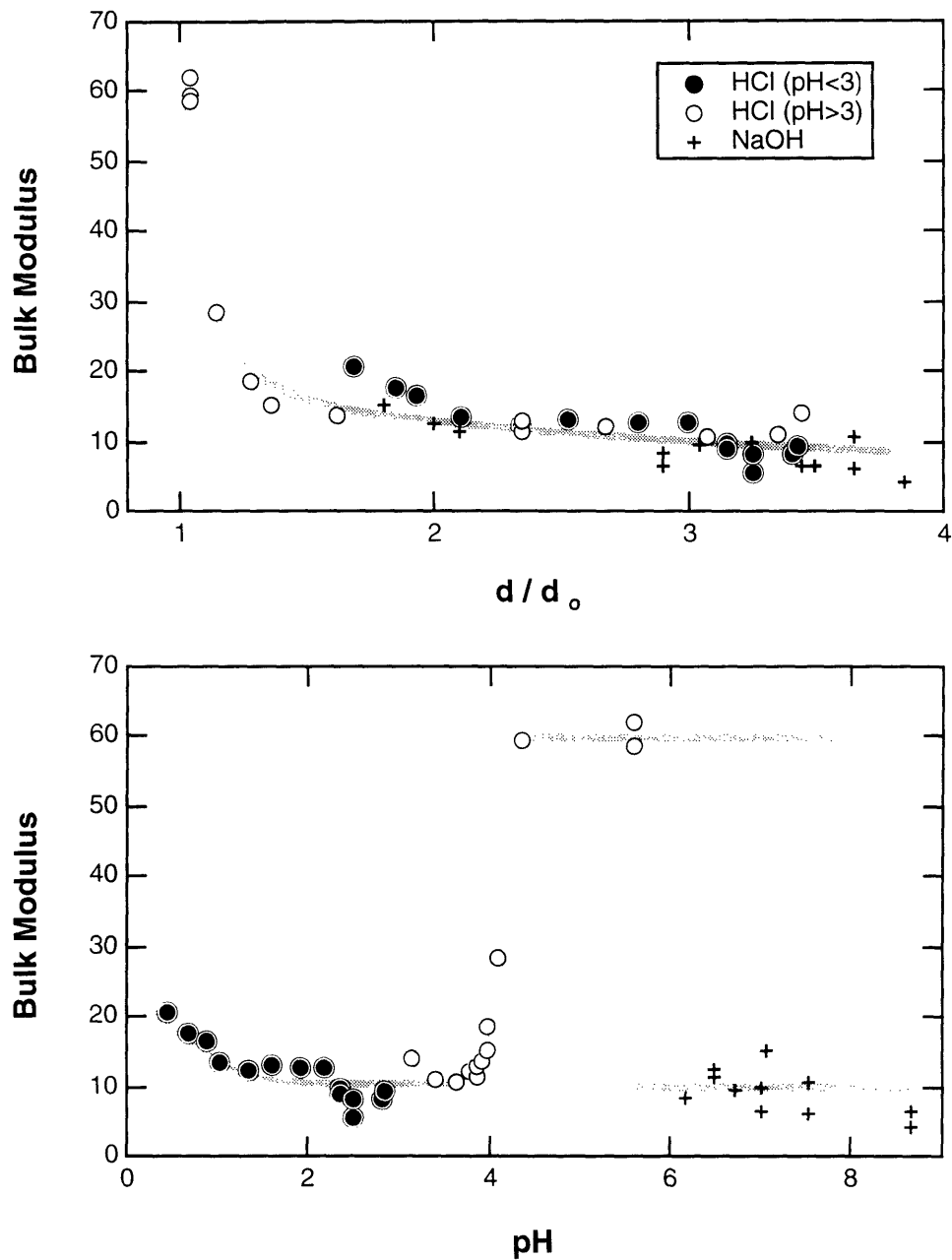


Fig. 14 Two plots of elastic modulus ($\propto \phi^2/lD$). Top graph is plotted vs. d/d_0 , while the bottom graph shows the pH dependence. It is interesting to observe from the top graph that, with the exception of lowest diameters, the elastic modulus does not change significantly with concentration (even as ϕ varies by an order of magnitude). The bottom graph reveals that there are two regimes, the "ground state" (top of the graph) being distinctly different from the swollen conditions.

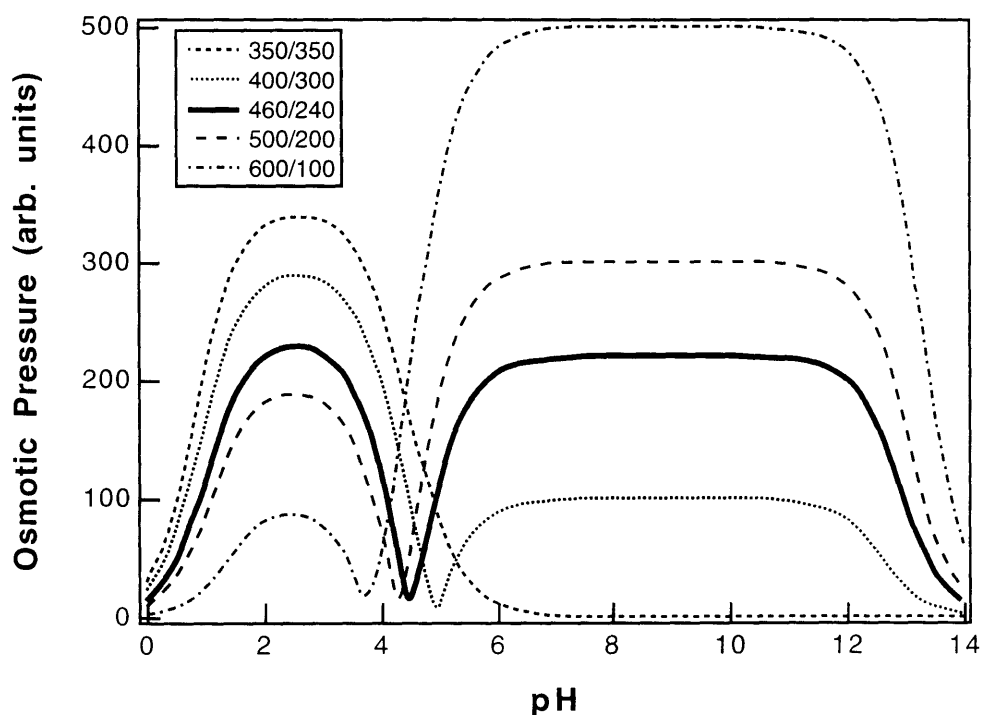


Fig. 15 Rough model of the osmotic pressure of counterions based on the total network charge (using the dissociation curve of AAc with $pK_A=4.5$), and moderated by the salt effect at extreme pH's. Curves for different molar ratios of AAc/MAPTAC are plotted.

points, if any, would be more likely to be unequilibrated. In addition, this behavior is consistent when pH is for increased and decreased. There is no discontinuous change of volume, so we must be near a critical point. It is noteworthy that the biggest change occurs in the static intensity.

What is the interaction responsible for the phase transition and for the gel structure hinted at in the results section? As mentioned at the beginning of this chapter, there are several interactions contributing to the behavior of this gel. Let's start by examining the repulsive counterion osmotic pressure. Fig. 15 shows a crude approximation of the strength of this interaction (at constant concentration). It was calculated considering only the net network charge concentration, modified by dissociation of AAc at varying pH's (assuming AAc's $pK_A=4.5$), and moderated by the salt effect (Cl^- and Na^+ concentration) at extreme pH's (this calculation follows Ref. (8)). It is interesting to observe a qualitative agreement of this curve with the outer envelopes of the swelling curves in Fig. 3 (including relative degrees of swelling for different

AAC/MAPTAC ratios). This indicates that it is the osmotic pressure of counterions that is responsible for the swelling (this is nothing very surprising, since it is the only long range repulsive force in the system).

Let us consider the attractive forces. It is obvious that they play an important role. For example the "ground state" (see Fig. 3) persists well into the region that would be swollen if only the counterion pressure were present (compare Fig. 15 with Fig. 3). There are two main attractive forces in the system: hydrogen bonding and the long range polyampholyte attraction (see Ref. (8) for a thorough description of the latter one). The multiplicity of phases (evident from Fig. 3) indicates that none of them could be ignored (we would expect much simpler behavior if only one type of attraction were present).

Hydrogen bonding is a cooperative process. If one hydrogen bond forms, others are likely to form among neighboring units (so-called zipper effect – cf. Ilmain et al. (9) who describe gel collapse caused by hydrogen bonding). Hydrogen bonding is likely to be responsible for the "ground state". Following two arguments support this hypothesis. First, the origin of the polyampholyte attraction is very similar to the origin of the osmotic pressure – both are due to the presence of network charges. Therefore above a certain value of pH (not too far from the isoelectric point, which almost coincides with the pK_A of AAC, since MAPTAC concentration is roughly one half of AAC's) one would expect both effects to be saturated with respect to their pH dependence. Only at very high pH's the salt contribution of Na^+ becomes important (even at $pH=10$ $[Na^+] \approx 0.1 mM$, much less than the network charge concentrations). Therefore we expect both the polyelectrolyte and polyampholyte effects to persist with unchanged strength beyond $pH=7.5-8$ where a discontinuous transition occurs. Hydrogen bonding is able to explain this transition. It competes with the dissociation of AAC – AAC can either dissociate or form a hydrogen bond, but not both. Thus dissociation of a hydrogen bonded AAC involves first breaking the bond. The energy penalty is justified only if the chemical potential of H^+ ions in the solution ($\propto -pH$) is low enough. Thus at some higher pH we expect the hydrogen bonds to start breaking and release the gel from its collapsed state.

The second argument for hydrogen bonding is the shape of the most swollen phase. We notice from Fig. 3 that it is attained only after a very high pH had been reached. It is consistent with the argument above – at a very high pH all the hydrogen bonds are broken, since the chemical potential of H^+ ions is very low under these circumstances. Once pH starts decreasing the formation of hydrogen bonds is impeded by the low concentration – to form a hydrogen bond two AAC units must come in contact having a correct spatial orientation, which is less likely if the concentration is low. Hence the most swollen phase is due mostly to the osmotic pressure of counterions – thus its

similarity to the osmotic pressure curves of Fig. 15. The difference is that there is a discontinuous phase transition back to the "ground state". If the preceding argument about the difficulty of hydrogen bond formation at high swelling ratios is correct, then another attraction has to be responsible for the discontinuous transition. Polyampholyte attraction is a good candidate, since it is long range. By the same argument, polyampholyte attraction should be responsible for the discontinuous collapse of the gel around $\text{pH}=4$. Hydrogen bonding must be partially responsible too, otherwise, by the reasoning already stated, there would be a large hysteresis associated with that transition, contrary to actual results (Fig. 3).

Let us now see how these hypotheses explain the scattering data. First let's go back to the pH of pre-gel solutions (Fig. 4). It was argued before (Sect. 7.2.3) that the jump in the intensities and the decay time is due to the difference in osmotic pressure (high at low pH 's and vice versa). Since the concentration does not change, there should be no impediments to hydrogen bonding formation. Furthermore, the pH range covered does not go beyond the transition out of the "ground state" at $\text{pH}\approx 8$. Therefore we can assume that no change in hydrogen bonding occurs, so it does not play an important role in the jump near $\text{pH}=4$. Since there is only a small pH range where the osmotic pressure of counterions decreases (cf. Fig. 15), this leaves only the polyampholyte attraction as a possible cause of the decrease of osmotic pressure (and bulk modulus) at $\text{pH}>4$. It is noteworthy that the static intensity increases as well. This might be due to segregation into denser and more dilute microdomains, as argued in Sect. 7.3.3.

The pH dependence of bulk modulus (Fig. 14) can be explained if we assume that hydrogen bonding is responsible for the "ground state". Hydrogen bonding introduces extra cross-linking into the gel, therefore making the gel stiffer, as reflected by higher bulk modulus (incompressibility) of the ground state. Another argument for the hydrogen bonding origin of this behavior is that bulk modulus increases rapidly only when d/d_0 is close to 1 (top graph of Fig. 14), which is consistent with hydrogen bond formation being impeded at low concentrations.

The relative concentration insensitivity of bulk modulus for higher swelling ratios can be explained by the formation of microdomains of varying concentration. A proverb says that a chain is only as strong as its weakest link. The bulk modulus would be determined by the dilute regions. Formation of such fluctuations can also explain why in Fig. 11 the largest peak occurs in the static intensity – static fluctuations critically diverge.

Finally, a comment can be made about the two branches of the static intensity's concentration dependence (Fig's 12 and 13). We notice in Fig. 13 that the upper branch

of the static intensity consists of higher pH values ($\text{pH} > 3$), while the lower branch – lower pH values and salt. This is consistent with the fact that we would expect the emergence of the polyampholyte effect at that pH (when AAc starts becoming ionized). Microdomains created by the polyampholyte effect contribute more to the static intensity, therefore higher pH's lay on the upper branch.

CONCLUSIONS

Several interesting effects were described in this chapter. Pre-gel solution's pH was shown to affect gel's scattering behavior. It was argued that polyampholyte attraction is responsible for this effect.

Molar ratio of the co-monomers was shown to affect little the scattering behavior of an unwashed gel in the range investigated. This is probably due to saturation of the network charge contribution to the osmotic pressure of an unwashed gel.

Gels whose diameter was constrained by swelling them inside a micropipette were shown to require a very long time to relax. Dynamic light scattering parameters (decay time and dynamic intensity) were not significantly affected by the constrained swelling ratio. This was taken as an evidence that the gels swelled almost to their equilibrium concentration, under a significant shear deformation. Existence of scattering vector size microdomains was given as a possible explanation for the apparent scatter of the static intensity as a function of swelling ratio.

A near-critical transition was demonstrated for a freely swollen gel near $\text{pH} = 4$. Polyampholyte attraction was indicated as a possible driving force making this transition discontinuous or critical. This polyampholyte attraction was argued to be responsible for the two-branched concentration dependence of static intensity – a feature that demonstrates that concentration alone is not sufficient to describe the system's behavior – there must exist another order parameter.

Hydrogen bonding was presented as the possible interaction keeping the gel in its lowest state (the "ground state") even when the osmotic pressure of counterions would be sufficient to swell it to a large diameter. Hydrogen bonding was also deemed responsible for the large hysteresis involved in swelling and collapsing of the gel.

To summarize, many effects related to this very complex and interesting systems were tackled, and some of them qualitatively described. This information will be useful in designing gels with desired properties, and aid in understanding the interactions that make possible design of "intelligent gels" with desired structure.

FURTHER RESEARCH

This chapter leaves plenty of room for further research. The original motivation was to examine, by light scattering, the differences between the multiple phases. As mentioned earlier, this proved rather difficult to do, since the phases scatter very little light. It would be very interesting to go back to that problem and perform more careful scattering experiments, perhaps using a stronger source of light (which would make up for the weak scattering), or using a different gel with more concentrated phases.

Number of very interesting effects was described in this chapter, but they were difficult to evaluate separately because of the complexity of the system. It would be very important to investigate these effects separately in simpler systems, where the claims about the origins of various features could be made with more certitude. In particular, if acrylic acid was substituted by a weak acid that does not form hydrogen bonds, the resulting system would allow us to understand more directly the contribution of the polyampholyte attraction. To investigate the effect of hydrogen bonding on light scattering, an experiment on pure acrylic acid could be performed.

The existence of microdomains was postulated on number of occasions throughout this chapter. In particular, it was suggested as an explanation for large scatter of static intensities as the gel was swollen to different diameters, or to explain the existence of two branches of concentration dependence of static intensity in a freely swollen gel. It would be very interesting to examine this effect directly, by performing angular dependence measurements (as mentioned in previous chapters, this is impossible using the current microscopic setup). This would provide direct information about the existence of such domains, and the length scales associated with them.

A number of aspects of this system were observed, but not reported here. In particular, there is an interesting salt concentration dependence in this system. In pure water the gel is collapsed. At high salt concentrations the diameter decreases with increasing salt concentrations. This is contrary to the findings of Yu (8), who finds that an unbalanced polyampholyte is fully swollen at zero salt concentration (though his system is much simpler – it does not involve hydrogen bonding). What happens at low salt concentrations? There must be a transition from collapsed to swollen gel (judging from the boundary conditions). Could this transition be discontinuous? It would be interesting to investigate.

Another observation mentioned only in passing in this chapter involves the shape of the correlation functions. It was noted that the free gel exhibits some non-exponential

"tails". This effect should be investigated in greater detail, especially near the transition around $\text{pH}=4$, where the tails resemble the power law behavior described in Chapter 6.

Finally, some of the interactions invoked to explain the phase behavior can be modeled analytically. In general, predicting the full phase behavior is very difficult (it was attempted by V. Pande). However, the limited conclusions reached in this chapter may be more amenable to being modeled than the whole phase diagram. Such analysis could strengthen their credibility.

To summarize, the experiments reported in this chapter raise more questions than they answer, and provide an ample opportunity for further investigation.

REFERENCES

- [1] Annaka, M and Tanaka, T.: *Nature*, **355**, 430-432 (1992).
- [2] Annaka, M, Ph.D. Thesis, University of Tokyo (1993)
- [3] Benedek, G.B. and Villars, F.M.H.: *Physics with Illustrative Examples from Medicine and Biology*, Vol. III, Addison-Wesley, Reading, MA (1979).
- [4] Hirotsu, S., Hirokawa, Y. and Tanaka, T.: *J. Chem. Phys.*, **87**, 1392 (1987).
- [5] Rabin, Y. and Bruinsma, R.: *Europhys. Lett.*, **20**, 79 (1992).
- [6] Li, Y. and Tanaka, T.: *Springer Proc. in Phys.*, **52**, 44-54 (1990).
- [7] Candau, S.J., Ilmain, F., Schosseler, F., Bastide, J.: *Mater. Res. Soc. Symp. Proc.*, **177**, 3-15 (1989).
- [8] Yu, X.H., Ph.D. Thesis, M.I.T. (1993).
- [9] Ilmain, F., Tanaka, T. and Kokofuta, E.: *Nature*, **349**, 400 (1991).

FURTHER RESEARCH

Many ideas for further research were mentioned at the end of each chapter. Some ideas of more general nature will be briefly listed here.

This thesis dealt a lot with decomposition of scattered light into dynamic and static components. The laws governing the dynamic part are well understood. Attention should be directed to the specific nature of the static part. Among interesting questions is the concentration dependence of the static intensity. Several chapters, especially Chapter 7, demonstrate that this dependence is very strong. Variation of its functional form (e.g., the exponent) among different types of gels can shed further light on these gels' structure. This dependence can be investigated in a straightforward way by preparing gels of slightly different compositions and different equilibrium swelling diameters. Even more direct measurement can be performed by controlling the equilibrium diameter of a single gel (thus avoiding possible composition dependence), through variation of its environment (pH, salt concentration, solvent composition). Yet another method may involve partially drying a gel and immersing it in a mineral oil, which would not penetrate the network, and prevent the gel from drying further. The equilibrium diameter can be measured directly, and the gel is free from a shear stress, so it can maintain its equilibrium shape. Finally, gels of varying initial concentrations (but same crosslinking ratios) can be prepared and scattering performed on them without taking them out of the micropipettes in which they were made.

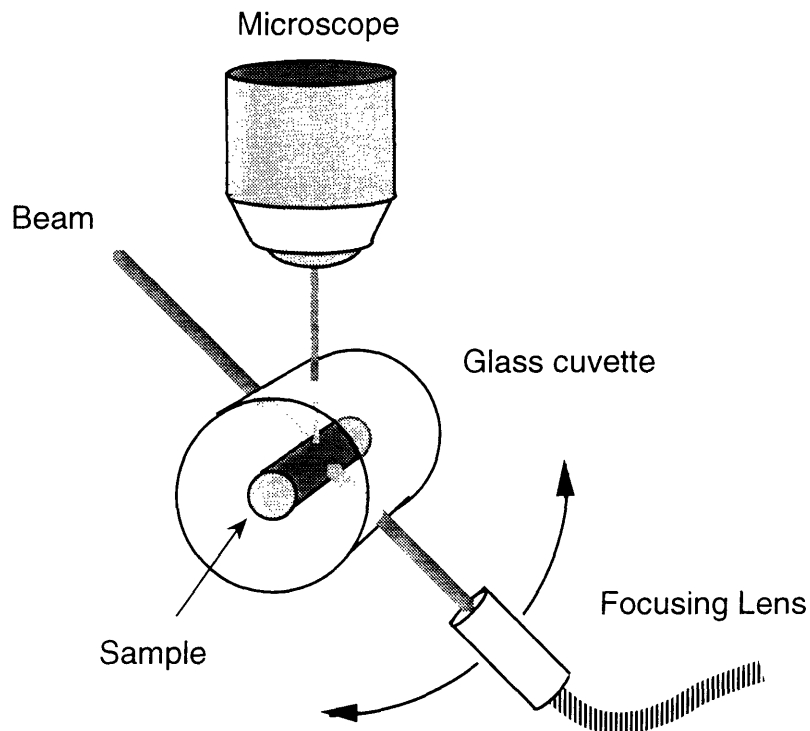
Another interesting phenomenon observed in this thesis, but not investigated very thoroughly, is the large difference in scattering by unwashed and freely swollen gels. This observation is true for many strongly charged gels. It merits a more in-depth study, which may reveal some facts about the structure of charged gels.

The techniques used in this thesis prove to be useful in investigating "exotic" gels (i.e., gels with very complex behavior). It would be interesting to continue this research with other types of "unusual" gels. For example, a comparison study of a balanced polyampholyte gel prepared in two different ways was commenced. One sample was prepared by random copolymerization of equal amounts of MAPTAC (3-methacryloyl-aminopropyl-trimethylammonium chloride – cationic component) and AMPS (2-acrylamido-2-methyl-1-propanesulfonic acid – anionic component). The second was obtained by polymerization of an organic salt of the same monomers (MAPTA-AMPS). Preliminary results show a significant difference in scattering properties (intensities and decay time) between the two samples. Further investigation of this system may reveal some information about molecular self-imprinting, besides furthering our knowledge about polyampholytes.

Several other experiments, not reported in this thesis, were performed by the author. Their continuing investigation can shed further light on the results of this thesis, as well as advance our understanding of gels in general. For example, in Chapter 7 it was reported that a gel whose swelling diameter was constrained by a micropipette would swell significantly along the unconstrained direction, reducing the overall concentration almost to its equilibrium value. A very different behavior was observed for a different gel – highly concentrated polyampholyte (2.36M of acrylic acid, 0.64M of allylamine hydrochloride and 0.1M of N-isopropylacrylamide). The scattering parameters (static and dynamic intensities and decay time) vary significantly with constrained swelling diameter. Furthermore, scattering from both unwashed and freely swollen gels (in several phases) is consistent with the results obtained for constrained gels. This is a sharp departure from the behavior reported in Chapter 7 and merits further investigation. It may also advance our understanding of internal structure of gels.

One deficiency of the scattering apparatus in its current form, mentioned often throughout this thesis, is its inability to perform multiple angle measurements. These measurements may reveal important information about characteristic length scales of structures present in gels. Furthermore, they help to distinguish between diffusive scattering modes, and more "exotic" non-diffusive effects.

The Figure shows a relatively straightforward modification of the scattering setup, which would facilitate performing multiple-angle measurements. The sample (either a micropipette holding the gel, or a freely swollen gel) is placed in the center of an optical



Design of a multiple-angle microscopic scattering setup

glass cuvette filled with water (for refractive index matching), or a solution of desired property (salt concentration, pH, solvent composition). Temperature could be controlled by heating or cooling this solution as it circulates through the cuvette. Focusing lens (at the end of a fiber delivering light from a laser) would be mounted on a goniometer centered on the axis of the cuvette, so different angles between the beam and the detected light could be achieved by rotating the focusing assembly. This relatively simple modification could further increase versatility of this apparatus.

Finally, results of this thesis (especially Chapter 6) show the usefulness of combining light scattering with other measurement techniques. They can include neutron scattering, nuclear magnetic resonance, etc. Future investigations directed along these lines may provide much more insight than results obtained by one technique alone.

To summarize, this thesis demonstrated the applicability of light scattering technique to study of many "exotic" gels. The biggest potential for further research lies in investigating new gel systems with interesting properties or applications.

CONCLUSION

This thesis presented a complete system for automated light scattering studies of gels, and used it to investigate many aspects of this scattering, for systems ranging from a simple neutral homopolymer gel, through a polyelectrolyte, finishing with a polyampholyte exhibiting multiple phase behavior.

First chapter presented a design of a logarithmic software correlator capable of measuring simultaneously delays from $0.8\mu\text{s}$ to several hours. This correlator provides an economic alternative to commercially available models, and can be used in many applications, including a clinical light scattering apparatus for early detection of cataracts. In this thesis it is used as a heart of a fully automated system for performing gel light scattering studies. Other components of the system include sample holders designed for exchange of solvents during an experiment, temperature control, sample translation for averaging over different positions, and software averaging and data analysis. This system proved itself as a useful general purpose tool for studying structure and properties of gels.

Chapter 2 used several existing theories of scattering from gels to devise a method for estimating ensemble averages from time average data collected at different locations. It also provided some means of understanding these ensemble averaged data. The methods presented in this chapter were used throughout this thesis and showed themselves applicable to analyzing the scattering behavior of many gels. Several simple experimental results were included as an illustration of the main ideas and their consequences, so Chapter 2 is a good introduction for anyone wanting to become familiar with light scattering from non-ergodic media, gels in particular.

Chapter 3 went beyond the theoretical considerations of Chapter 2 and investigated the origin of structural inhomogeneities within a gel directly. It demonstrated that there are two kinds of permanent structural inhomogeneities, and dynamic fluctuations. Their formation was shown to be determinable from the relative position of the gel state point within the phase diagram either at the onset of gelation process, or at the measurements of inhomogeneities. Therefore, the concept of phase transitions of gel and polymer solution was demonstrated to be important in predicting the gel network structure. The spatial inhomogeneities, although their structure is permanent, can be enhanced as temperature approaches the spinodal line, and diverge at the line. The findings presented in this chapter could be useful in controlling the gel structure and thus the physical properties of gels such as permeability, viscoelasticity, and optical clarity. Moreover, the studies presented show that information may be stored in a distributed way as spatial inhomogeneities within a 3-dimensional gel, and that it can be readily observed with the aid of scattered laser light. This may be useful in various applications including 3-dimensional holography.

Chapter 4 investigated phase diagram of NIPA (N-isopropylacrylamide) monomer, whose gel was studied in Chapter 3. It was found that this phase diagram is qualitatively similar to that of Poly(NIPA) and of NIPA gels, as it also exhibits a lower-critical solution temperature, above which the solution (or a gel) undergoes phase separation. This behavior is due to hydrophobic interaction of NIPA monomers in all three cases. The experiments revealed, however, large quantitative differences. Critical point of a monomer solution is much lower than in the other two cases. Dilute monomers can exist in a single phase in concentrations much higher than gels and solutions (and concentrated monomers in much lower). Finally, crystallization occurs in monomers, while it is not observed in polymers and gels. Findings of this chapter, apart from a general interest in phase behavior of hydrophobic molecules, provide a direct indication about the mechanism of permanent structural inhomogeneity formation in NIPA gels, as described in Chapter 2.

Chapter 5 investigated measurement temperature dependence of light scattering in a NIPA gel as the gel went through a discontinuous volume phase transition. Scattering from both swollen and collapsed gel was investigated and compared. The shapes of the correlation functions obtained at different gel conditions, as well as the temperature dependence of the ratio of static to dynamic intensities support the model presented in Chapters 2 which attributed the dynamic portion to collective diffusion. Local variations

of polymer density are enhanced near the spinodal line and the static scattering that they cause diverges, as argued in Chapter 3. Vanishing of bulk modulus at the spinodal line is useful in explaining the near-critical behavior in the light scattering parameters near the transition point. Experiments reported in this chapter shed some new light on the network-solvent friction. Friction coefficient obtained by light scattering was found to behave very differently from the friction coefficient measured by a macroscopic liquid flow. This was argued to be due to different aspects of the friction measured by these two techniques. In general, the data presented in this chapter confirm a number of results mentioned earlier in this thesis.

Chapter 6 investigated scattering behavior of a weakly charged polyelectrolyte gel, examined previously using neutron scattering (SANS) technique by other researchers in this lab. Light scattering data collected along an isochore of a charged NIPA gel was found in qualitative agreement with published SANS results. Two transition temperatures were found. The first manifested itself through a qualitative change of the correlation function shape – a power law component appeared besides a single exponential. This corresponds to the emergence of a peak in the static structure factor obtained by SANS for the same sample. The model used to explain the SANS data (microphase separation into charged dilute charged and dense neutral domains) was found consistent with light scattering results. A discontinuous volume transition was observed at a higher temperature. It was argued that the microdomains coexist even above that point. A novel dynamic behavior was reported – power law shape of the correlation function. Several interesting aspects were noticed. It emerges at a specific temperature corresponding to the microphase separation of NIPA/AAC gel. The exponent itself depends on temperature, contrary to the usual scaling law behavior. An attempt was made to compare this effect to other known examples of such phenomenon, especially in the case of silica gels at the gelation threshold. No qualitative conclusion regarding the nature of the phenomenon was reached, leaving the field wide open to further research.

Finally, Chapter 7 investigated light scattering by a multiple phase polyampholyte gel. Several interesting effects were described in this chapter. Pre-gel solution's pH was shown to affect gel's scattering behavior. It was argued that polyampholyte attraction is responsible for this effect. Gels whose diameter was constrained by swelling them inside a micropipette were shown to require a very long time to relax. Dynamic light scattering parameters (decay time and dynamic intensity) were not significantly affected by the constrained swelling ratio. This was taken as an evidence that the gels swelled almost to

their equilibrium concentration, under a significant shear deformation. Existence of microdomains whose size approximates the scattering vector was given as a possible explanation for the scatter of the static intensity as a function of the swelling ratio. A near-critical transition was demonstrated for a freely swollen gel near $\text{pH}=4$. Polyampholyte attraction was indicated as a possible driving force making this transition discontinuous or critical. This polyampholyte attraction was argued to be responsible for two-branched concentration dependence of static intensity – a feature which demonstrates that concentration alone is not sufficient to describe the system's behavior – there must exist another order parameter. Hydrogen bonding was presented as the possible interaction keeping the gel in its lowest state even when the osmotic pressure of counterions would be sufficient to swell the gel to a large diameter. Hydrogen bonding was also deemed responsible for the large hysteresis involved in swelling and collapsing of the gel. Information presented in this chapter could be useful in preparing gels with desired properties, and aid in understanding interactions that make possible design of "intelligent gels" able to perform some useful tasks in response to changing environment.

Summarizing, this thesis demonstrated that the relatively old technique of dynamic light scattering can be successfully applied towards understanding new and complex gel systems. The intense research in designing "intelligent gels" will be greatly aided by application of this technique. Many of the results presented in this thesis already provide a basis for understanding some of the interactions that make gels and gel phase transitions so useful.

1
3636-12